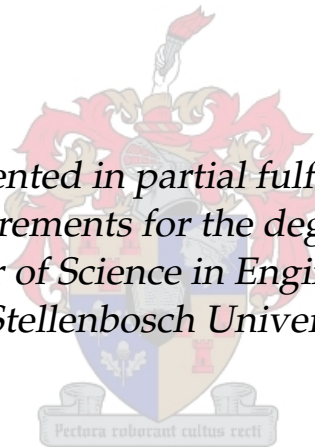


Investigation and Design of a Slotted Waveguide Antenna with Low 3D Sidelobes

by

Andries Johannes Nicolaas Maritz

*Thesis presented in partial fulfilment of the
requirements for the degree of
Master of Science in Engineering
at Stellenbosch University*



Supervisor:

Prof. Keith D. Palmer

Department Electrical and Electronic Engineering

March 2010

Declaration

By submitting this thesis electronically, I declare that the entirety of the work contained therein is my own, original work, that I am the owner of the copyright thereof (unless to the extent explicitly otherwise stated) and that I have not previously in its entirety or in part submitted it for obtaining any qualification.

March 2010

Abstract

An investigation into the cause of undesired sidelobes in the 3D radiation pattern of slotted waveguide arrays is conducted. It is hypothesized that the cross-polarization of the antenna is at fault, along with the possibility that an error is made when designing a linear array. In investigating and finding a solution to the problem, the "Z-slot" is introduced in conjunction with polarizer plates. The base components are used by a custom optimization algorithm to design reference and solution antennas. Results of the antennas are then compared to ascertain the cause and possible solutions for the unwanted sidelobes. The generic nature of the process may be used to characterize other arbitrary aperture configurations and to design larger antennas.

Opsomming

'n Ondersoek om die oorsaak van ongewenste sylobbe in die 3D uitstraalpatroon van golfleier-antennas vas te stel. Die hipotese is dat die probleem ontstaan uit die kruis-polarisasie van die antenna, tesame met 'n verkeerde-likke aanname dat die opstelling liniêr is. Die "Z-Gleuf" tesame met polariseringsplate word voorgestel as hulpmiddel om die moontlike oorsake te ondersoek. 'n Gespesialiseerde optimerings-algoritme benut hierdie basiskomponente om beide verwysings- en oplossing-antennas te ontwerp. Resultate van die ontwerpde antennes word dan vergelyk om die oorsaak van die ongewenste sylobbe te vas te stel. Die generiese aard van die proses kan toegepas word op enige gleuf-konfigurasie en om groter antennes mee te ontwerp.

Acknowledgements

The author would like to thank the following people for their contribution towards this project.

- Prof K.D. Palmer
- Werner Steyn
- Jonathan Hoole

Contents

Abstract	iii
Opsomming	iv
Acknowledgements	v
Contents	vi
Abbreviations	ix
List of Figures	x
List of Tables	xv
1 Introduction	1
1.1 Problem Statement	1
1.2 Project Overview	3
1.3 Thesis Outline	4
2 Literature Study	6
2.1 Waveguides	6
2.2 Aperture Antennas	15
2.3 Transmission Line Theory	19
2.4 Array Synthesis	22
2.5 Waveguide Slot Arrays	23
3 Design of the Waveguide Transmission Line	25
3.1 Waveguide Specifications	25
3.2 Properties of Rectangular Waveguides	26
3.3 Design of a Ridged Waveguide	27
4 Analysis of Aperture Radiators	32
4.1 Discussion of Slot Properties of Interest	32
4.2 <i>Study</i> : Offset Rectangular Aperture in the Broadwall	34
4.3 <i>Study</i> : Z-slot Aperture in the Broadwall	35

4.4	<i>Study</i> : Z-slot Aperture in the Broadwall with Polarizer Plates	37
4.5	<i>Study</i> : Z-slot Aperture in a Ridged Waveguide	38
4.6	<i>Study</i> : Z-slot Aperture in a Ridged Waveguide with Polarizer Plates	39
4.7	<i>Study</i> : Varying Polarizer Plate Lengths in a Z-slot Ridged Waveguide Configuration	40
4.8	Equivalent Circuit Models	44
4.9	Simulation Results	45
5	Algorithms for Aperture Characterization & Antenna Optimization	47
5.1	Discussion of the Parameter Sweep Algorithm	47
5.2	Extraction of Impedance Properties from S-Parameters	49
5.3	Simulation Results of a Parameter Sweep	53
5.4	Optimization Algorithm	56
5.5	Validation of CST Models	65
6	Antenna Designs and Comparison	68
6.1	Benchmark Design	68
6.2	WR75 Z-slot Antenna Design	73
6.3	Ridged Waveguide Z-slot Antenna Design	78
6.4	Comparison of Benchmark and Z-slot Antenna Properties	83
7	Conclusions	88
7.1	Summary	88
7.2	Recommendations for Future Research	89
7.3	Conclusion	90
	Appendices	91
A	Benchmark Design	92
A.1	Introduction	92
A.2	Dimensions	92
A.3	Simulated Results	93
B	WR75 Waveguide Z-slot Design	95
B.1	Introduction	95
B.2	Dimensions	95
B.3	Simulated Results	96
C	Ridged Waveguide Z-slot Design	98
C.1	Introduction	98
C.2	Dimensions	98
C.3	Simulated Results	100

CONTENTS

viii

D WR90 to Ridged Waveguide Transition

102

Bibliography

105

Abbreviations

- TE – Transverse Electric
- TM – Transverse Magnetic
- TEM – Transverse Electromagnetic
- CST – CST Microwave Studio (software tool)
- E-Field – Electric Field
- H-Field – Magnetic Field
- λ_0 – Free-Space Wavelength
- f_0 – Operating Frequency
- λ_G – Waveguide Wavelength

List of Figures

1.1	Azimuth Depiction of Radiation Pattern for an Antenna Array . . .	2
1.2	3D Radiation Pattern of a Slotted Waveguide Antenna	2
2.1	Axis System for Arbitrary Transmission Lines and an Example of a Transmission Mode	7
	(a) Axis System for Generic Waveguides	7
	(b) TE_{10} Propagation Mode in a Rectangular Waveguide	7
2.2	Parallel Plate Transmission Line	8
2.3	Attenuation and Propagation Constant as a Function of Frequency	9
2.4	Rectangular Waveguide Dimensions and Axis System	10
2.5	First Modes and their Cutoff Frequencies Found for the WR90 Waveguide Profile	11
	(a) TE_{10} : $f_c =$ at 6.55 GHz	11
	(b) TE_{20} : $f_c =$ at 13.07 GHz	11
	(c) TE_{01} : $f_c =$ at 14.73 GHz	11
	(d) TE_{11} : $f_c =$ at 16.12 GHz	11
	(e) TM_{11} : $f_c =$ at 16.12 GHz	11
	(f) TM_{21} : $f_c =$ at 19.69 GHz	11
2.6	TE_{10} Mode Fields and Currents	14
	(a) E-Field of a TE_{10} Wave Along the Waveguide	14
	(b) E-Field TE_{10} Mode in a Rectangular Waveguide (at the Port)	14
	(c) H-Field of a TE_{10} Wave Along the Waveguide	14
	(d) Surface Current J_s of a TE_{10} Wave Along the Waveguide . .	14
2.7	Single-Ridged Waveguide	15
	(a) Single-Ridged Waveguide	15
	(b) Profile and Notation of a Single-Ridged Waveguide	15
2.8	An Aperture Cut in a Screen with its Complementary Component	16
2.9	Aperture Excitation and Transmission Line Model	17
2.10	Equivalent Circuit Models for Offset and Rotated Aperture An- tennas	18
	(a) Offset Aperture Antenna and its Equivalent Circuit Model .	18
	(b) Rotated Aperture Antenna and its Equivalent Circuit Model	18
2.11	Cascaded ABCD Parameters	19
2.12	Two-Port ABCD Network	19

2.13	ABCD Representation of a Transmission Line	20
2.14	ABCD Representation of a Series Impedance	21
2.15	ABCD Representation of a Parallel Admittance	21
2.16	Example of a Cascaded ABCD Network	21
2.17	Element Excitations for Two 40 Element Arrays	22
	(a) 40 Element Tschebyscheff Excitation	22
	(b) 40 Element Villeneuve Excitation	22
3.1	Depiction of Waveguide Specifications	26
3.2	Standard Rectangular Waveguide	26
3.3	Single-Ridged Waveguide	27
	(a) Single-Ridged Waveguide	27
	(b) Profile and Notation of a Single-Ridged Waveguide	27
3.4	Cutoff Frequencies of a Ridged Waveguide with a Fixed a and b .	29
	(a) Lower Cutoff Frequencies	29
	(b) Higher Cutoff Frequencies	29
3.5	Region Where Both the Lower and Higher Cutoff Frequency Specifications are Met	30
3.6	Physical Dimensions of Final Ridged Waveguide	30
4.1	Definition of Amplitude Tuners	33
4.2	Model for Rectangular Aperture at Some Offset from the Centerline of the Waveguide	34
	(a) 3D Wireframe of Aperture	34
	(b) Top View of Aperture in Waveguide	34
4.3	Model for Z-slot at Some Rotation Angle	36
	(a) 3D Wireframe of Aperture	36
	(b) Top View of Aperture in Waveguide	36
4.4	Model for Z-slot with 10mm Polarizer Plates	37
	(a) 3D Wireframe of Aperture	37
	(b) Top View of Aperture in Waveguide	37
4.5	Model for Z-slot in a Ridged Waveguide	38
	(a) 3D Wireframe of Aperture	38
	(b) Top View of Aperture in Waveguide	38
4.6	Model for Z-slot with 10mm Polarizer Plates in a Ridged Waveguide	40
	(a) 3D Wireframe of Aperture	40
	(b) Top View of Aperture in Waveguide	40
4.7	Cross-Polarization Level with Varying Polarizer Plate Lengths . .	41
4.8	Bandwidth Variation as a Result of Varying Polarizer Plate Lengths	42
4.9	Radiated Power and Q-Factor for Varying Polarizer Plate Lengths	43
	(a) Percentage of Power Radiated at f_0 for Varying Polarizer Plate Lengths	43
	(b) Quality Factor at f_0 for Varying Polarizer Plate Lengths . . .	43

4.10	Phase of S_{11} for an Offset Aperture and a Z-slot	44
4.11	Percentage Bandwidth	45
4.12	Percentage of Power Radiated by Aperture	46
4.13	dB Cross-Polarization Level	46
5.1	Flow Chart of the Parameter Sweep	48
5.2	Z-slot Environment and Port Definitions	49
	(a) Z-slot Calibration Model for the Parameter Sweep	49
	(b) Port Locations Between Apertures and their Normal Direc- tions	49
5.3	Location of Aperture Impedances With Respect to the Load Impedance	53
5.4	Resistance: Real Part of the Aperture Impedance	53
5.5	Reactance: Imaginary Part of the Aperture Impedance	54
5.6	Phase Slope: Rate with which Impedance Changes	55
5.7	Phase of the Impedance	55
5.8	Flow Chart of the Optimization Algorithm	56
5.9	Transmission Line Model for a Z-slot Antenna	57
	(a) Equivalent Transmission Line Model of a Z-slot Antenna	57
	(b) Reduced Transmission Line Model of a Z-slot Antenna	57
	(c) Depiction of Argument for Reduced Transmission Line Model	57
5.10	Villeneuve Power and Impedance Distribution	58
5.11	Magnitude and Phase of Electric Field over the Antenna	60
	(a) Magnitude of E_x of the Electric Field Over the Antenna	60
	(b) Phase of E_x of the Electric Field Over the Antenna	60
5.12	Series Impedance Transmission Line Model Notation	61
5.13	Curve Fitted to Simulated Data	62
5.14	Prediction Grids Before and After Adaptation	63
	(a) Original Prediction Grid	63
	(b) Adapted Prediction Grid	63
5.15	Gain Patterns for 40 Element Offset Rectangular Aperture Array	66
5.16	Zoom of Gain Patterns for 40 Element Offset Rectangular Aper- ture Array	67
6.1	CST Model of the Benchmark Template and Antenna	69
	(a) Template Used to Generate the Antenna	69
	(b) Antenna Generated by Optimization Algorithm	69
6.2	Simulated Magnitudes for All Iterations of the Benchmark Antenna	70
	(a) Simulated Magnitudes Over All Iterations	70
	(b) Simulated Magnitude for Final Iteration	70
6.3	Simulated Phases for All Iterations of the Benchmark Antenna	71
	(a) Simulated Phases Over All Iterations	71
	(b) Simulated Phase for Final Iteration	71

6.4	Radiation Pattern for the Benchmark Design	72
6.5	CST Model of the WR75 Z-slot Template and Antenna	73
	(a) Template Used to Generate the Antenna	73
	(b) Antenna Generated by Optimization Algorithm	73
6.6	Total Radiated Power After Each Element	73
6.7	Simulated Magnitudes for All Iterations of the WR75 Z-slot Antenna	75
	(a) Simulated Magnitudes Over All Iterations	75
	(b) Simulated Magnitude for Final Iteration	75
6.8	Simulated Phases for All Iterations of the WR75 Z-slot Antenna .	76
	(a) Simulated Phases Over All Iterations	76
	(b) Simulated Phase for Final Iteration	76
6.9	Radiation Pattern for the WR75 Z-slot Design	77
6.10	CST Model of the Ridged Waveguide Z-slot Template and Antenna	78
	(a) Template Used to Generate the Antenna	78
	(b) Antenna Generated by Optimization Algorithm	78
6.11	Simulated Magnitudes for All Iterations of the Ridged Wave- guide Z-slot Antenna	79
	(a) Simulated Magnitudes Over All Iterations	79
	(b) Simulated Magnitude for Final Iteration	79
6.12	Simulated Phases for All Iterations of the Ridged Waveguide Z-slot Antenna	80
	(a) Simulated Phases Over All Iterations	80
	(b) Simulated Phase for Final Iteration	80
6.13	Radiation Pattern for the Ridged Waveguide Z-slot Design	81
6.14	Simulated Excitation Weightings for All Iterations of the Z-slot Antenna	82
	(a) Simulated Weighting Over All Iterations	82
	(b) Simulated Weighting for Final Iteration	82
6.15	3D Radiation Patterns	83
	(a) Benchmark 3D Radiation Pattern	83
	(b) Z-slot Ridge 3D Radiation Pattern	83
	(c) Z-slot WR75 3D Radiation Pattern	83
6.16	Polarization Components in the Radiation Pattern	84
6.17	Absolute Radiation Pattern Including Both Polarization Compo- nents	85
6.18	Cross-Polarization Level in the Azimuth Cut	85
6.19	Horizontal Cut ($\phi = 0^\circ$) of Radiation Pattern for All Designs . . .	86
6.20	Diagonal Cut ($\phi = 45^\circ$) of Radiation Pattern for All Designs . . .	86
6.21	Vertical Cut ($\phi = 90^\circ$) of Radiation Pattern for All Designs	87
A.1	Model of the Benchmark Antenna	92
	(a) 3D Radiation Pattern	94
	(b) Azimuth Radiation Pattern	94

B.1	Model of the WR75 Z-slot Antenna	95
(a)	3D Radiation Pattern	97
(b)	Azimuth Radiation Pattern	97
C.1	Model of the Ridged Waveguide Z-slot Antenna	98
C.2	Waveguide Profile for the Ridged Waveguide Z-slot Antenna	99
(a)	3D Radiation Pattern	101
(b)	Azimuth Radiation Pattern	101
D.1	Magnitude of S_{11}	103
D.2	Two-port Model for the Waveguide Transition	103
D.3	Single-Ended WR90 to Ridged Waveguide Transition	104
(a)	3D View	104
(b)	Top View	104
(c)	Side View	104
(d)	Front View	104

List of Tables

1.1	Antenna Properties	4
3.1	Waveguide Specifications	25
3.2	Standard Rectangular Waveguide Profiles	27
3.3	Properties of Final Ridged Waveguide Design	30
4.1	Properties of a 25° Z-slot Antenna Compared to the Addition of Polarizer Plates	44
5.1	Properties of the Antenna Used for Validation	65
6.1	Specifications for the Benchmark Design	68
A.1	Dimensions of Benchmark Apertures	93
B.1	Dimensions of Z-slot Apertures in WR75	96
C.1	Dimensions of Z-slot Apertures in a Ridged Waveguide	99

Chapter 1

Introduction

Slotted waveguide antennas are a class of antenna commonly used in microwave radar applications. Therefore it can be argued that antennas of this type must exhibit properties desirable for the implementation of a radar system. Looking at an antenna used in a radar system [1], it can be seen that some of the desirable functions include:

- The focusing of radiated energy toward a target;
- To act as a spatial filter to only recognize energy originating from the direction of a target; and
- To collect the energy scattered back from a target in the illuminated region.

The antenna also serves several other important roles, but the research done here aims to improve the quality of the antenna as it pertains to the functions mentioned.

An antenna would be suitable if it exhibits high gain in one direction, while suppressing the sidelobes in all other directions. High gain serves to concentrate energy toward a target as well as collecting scattered energy from a target. Low sidelobes serve to act as a spatial filter that will help in resolving targets and determining their position.

Slotted waveguide antennas have been a popular choice for mechanically steered antennas since the 1970's and are found in a variety of 3D radar antennas.

1.1 Problem Statement

The radiation pattern performance of linear arrays is often measured in a plane perpendicular to the array direction (call it the azimuth direction) as in Fig. 1.1. However, when the radiation pattern is analyzed in all directions, sidelobes can be seen to emerge.

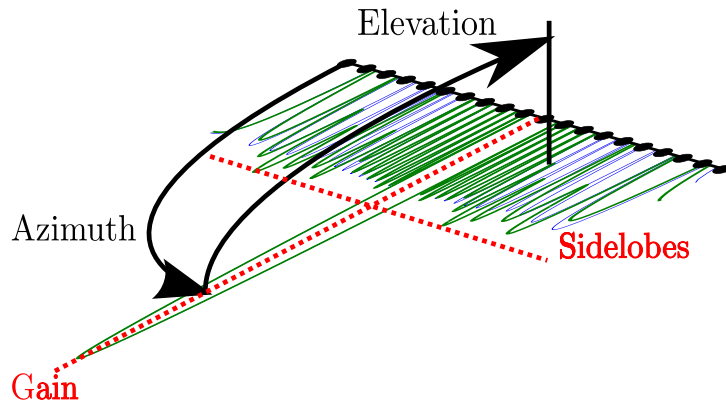


Figure 1.1: Azimuth Depiction of Radiation Pattern for an Antenna Array

The gain is shown in Fig. 1.1 as the main lobe. It is an indication of how much energy is being concentrated in a specific direction relative to an isotropic antenna. The sidelobes are the smaller lobes to the side of the main lobe. The sidelobe level refers to the maximum amount of energy that can be radiated in any direction other than the direction of the main lobe.

As stated, when the elevation pattern is also taken into consideration, the sidelobes become large. Fig. 1.2 shows these sidelobes. It can be seen that the sidelobes disappear when the elevation is zero.

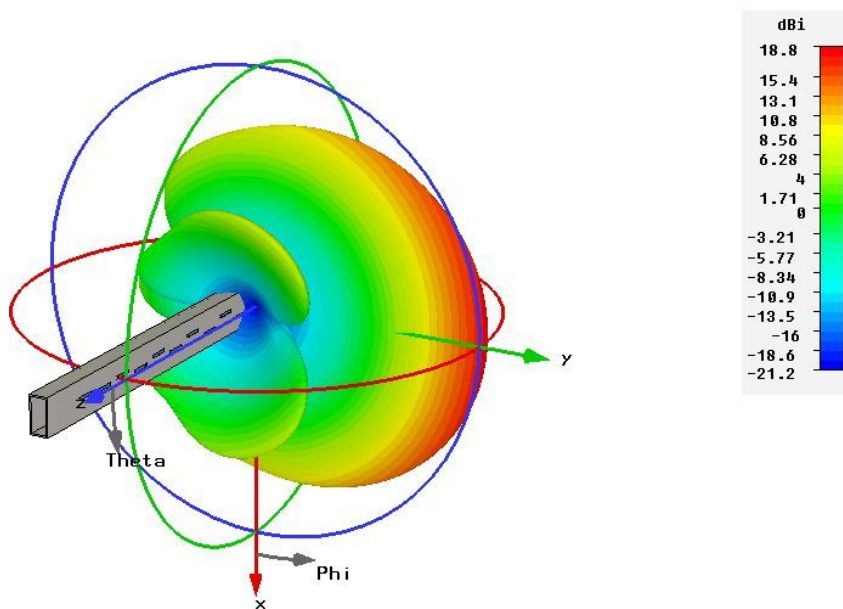


Figure 1.2: 3D Radiation Pattern of a Slotted Waveguide Antenna

The presence of these sidelobes are undesirable for radar antennas because:

- It focuses energy in multiple directions, instead of the one desired direction;
- It ceases to function as a spatial filter, since it can recognize energy from multiple directions; and
- Even though energy that is scattered from a target is collected, it could also collect energy from different directions due to reflections.

For the antenna to be effective for radar applications, the source of the sidelobes must be investigated and addressed. There are two suspected causes for the sidelobes. The first is that the offset of the rectangular apertures of the antenna in Fig. 1.2 causes the linear array approximation to become invalid. In effect, behavior of a planar array is observed where the design that is typically used assumes a linear array. The second possibility is that the cross-polarization component of the antenna causes a sidelobe. The cross-polarization is assumed to be small, but if enough energy is radiated in the cross-polarization, it will affect the magnitude of the energy radiated in a direction enough to alter the radiation pattern.

The aim is to identify to which extent these two possibilities affect the radiation pattern of a slotted waveguide antenna. An antenna which compensates for the problem is then designed to provide a practical low side-lobe antenna for radar applications.

1.2 Project Overview

Two suspected causes contribute to the sidelobes seen in Fig. 1.2. The source of the two causes, namely

1. cross-polarization and
2. the incorrect assumption of a linear array,

must be investigated and understood. This involves an investigation into the cross-polarization properties of radiating elements and how to suppress them. Also, an aperture array configuration that enforces a linear array must be found.

Once a linear array with a controllable cross-polarization component can be designed, the source of the sidelobes can be discerned. A benchmark antenna (such as the one displayed in Fig. 1.2) is developed that exhibits the unwanted sidelobes. Two antennas are developed and compared to the benchmark design. One antenna must have similar cross-polarization properties to the benchmark, but a linear array configuration. The other antenna must have a different cross-polarization level to the benchmark.

In order to compare the antennas, they must have the same design goals. The design parameters are given in Tab. 1.1.

Table 1.1: Antenna Properties

Property	Value
Waveguide Profile	Any: Max width = 16 mm
Feed	Traveling Wave
Bandwidth	Not specified
Operating Frequency (f_0)	10.5 GHz
Number of Elements	20
Load Power (P_L)	13%
Sidelobe Level (Design)	-35 dB
Sidelobe Level (Real)	-30 dB
Excitation Taper	Villeneuve

Note that any profile may be used, with the constraint that the the inside width of the waveguide does not exceed 16 mm. This is a physical restriction that is included for practical reasons [2]. All other constraints are chosen arbitrarily or for convenience. Typically, more elements would be required (> 100), but is costly in terms of computational requirements.

Care is taken to ensure that the antennas adhere as closely as possible to the requirements of Tab. 1.1 to ensure that no other variables influence the investigation. A specialized optimization algorithm is devised to generate the antennas and to analyze their properties.

Successful completion of the investigation will include three complete antenna designs with the desired attributes. An analysis of the comparison between the antennas will be completed and the source of the sidelobes of Fig. 1.2 will be isolated.

1.3 Thesis Outline

The thesis aims to follow the flow described above. First an investigation into the radiating elements is conducted to ascertain their cross-polarization and physical properties. Once the general attributes are understood, the aperture antennas are characterized and analyzed in preparation for the array designs. This is followed by the development of an optimization algorithm that is used for the design of the slotted waveguide antennas. The designs are then compared and analyzed.

Chapter 2 provides the scientific background that is required for understanding the work done in other chapters. Literature covering important principles is reviewed and summarized to provide a broad understanding of how the research is conducted. The literature covers topics including waveguides, aperture antennas, transmission line theory, array synthesis and slotted waveguide arrays.

The design of the waveguide profile is given in chapter 3. Standard rectangular waveguide profiles are considered for the design, as well as custom profiles. Ridged waveguides in particular are investigated as a possible solution. The benefits and drawbacks of each is considered and a design decision is made.

Aperture antennas are discussed in chapter 4. The Z-slot is introduced and characterized with respect to the offset rectangular aperture. The Z-slot is a hybrid between a rotated slot and an offset longitudinal slot, which is suggested by Prof. K.D. Palmer of the University of Stellenbosch. The offset aperture is used for the benchmark antenna, as it is commonly found in practice [3]. The apertures will be analyzed in terms of their inherent cross-polarization properties, radiation capability and bandwidth. The effect of polarizing plates is also investigated.

Once the general behavior of an aperture antenna is understood, it can be characterized as described in chapter 5. A series of simulations are performed where the physical properties of the aperture is altered and its impedance properties recorded. The data generated in chapter 5 is used in the design process to predict the behavior of an aperture.

A basic optimization algorithm is implemented that makes use of prior knowledge of an aperture (which is obtained through the method explained in chapter 5). This algorithm and its results are discussed in chapter 6. The results of the different antenna designs are compared and analyzed.

Chapter 7 serves to provide a wide view of the work done and to indicate any useful conclusions that may be drawn from the results. Relevant information is drawn from the different phases of the completed work, including: the characterization of isolated apertures; the optimization algorithm and the comparison of the final antenna designs with respect to their radiation pattern properties. Further details on the antennas that are generated can be found in the appendices, including complete specifications required for manufacture.

Chapter 2

Literature Study

Before the analysis and design of the antenna is discussed, it would be useful to review some of the more important concepts involved. The aim is to introduce the reader to the terminology that will be used and the key concepts that will be investigated in later chapters.

2.1 Waveguides

A waveguide is a hollow tube made of a single conductor that can propagate electromagnetic fields at certain frequencies [4]. The fields reflect off the conducting walls of the tube and propagate forward. This type of transmission line is common among high-frequency applications because of its high power handling capability and low loss [5].

2.1.1 Types of Propagation in Waveguides

The three types of waves that can propagate through a transmission line are *TEM* (Transverse Electromagnetic), *TE* (Transverse Electric) and *TM* (Transverse Magnetic) waves [5]. Transverse waves are those waves for which the energy is stored in a plane perpendicular to the direction of propagation [4]. In other words, a plane wave propagating in the z -direction, as would be the case in Fig. 2.1(a), will be transverse if the z -component of the wave is equal to zero.

The subscript in Fig. 2.1(b) denotes which mode is being propagated. In this case, for example, TE_{10} implies that the transverse electric mode is being propagated (i.e. $E_z = 0$) and that only one half-wavelength can fit into the wide dimension of the waveguide. A more detailed discussion on *TE* modes will follow in section 2.1.1.2. The electric field (\vec{E}) and magnetic field (\vec{H}) are defined in the coordinate system of Fig. 2.1(a) by Eq. 2.1.1 and

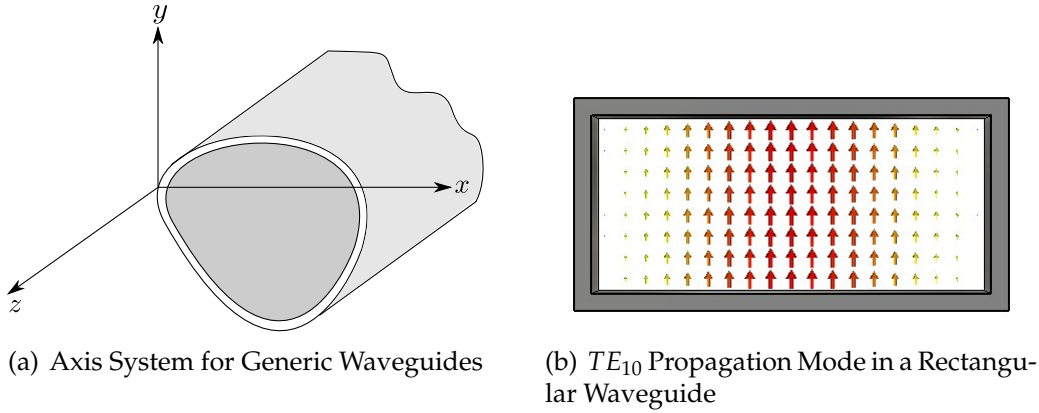


Figure 2.1: Axis System for Arbitrary Transmission Lines and an Example of a Transmission Mode

Eq. 2.1.2 respectively.

$$\vec{E} = \hat{x}E_x + \hat{y}E_y + \hat{z}E_z \quad (2.1.1)$$

$$\vec{H} = \hat{x}H_x + \hat{y}H_y + \hat{z}H_z \quad (2.1.2)$$

2.1.1.1 TEM Waves

TEM waves are characterized by the z -components of the electric and magnetic fields being zero, or $E_z = 0$ and $H_z = 0$. Waves of this type require two or more conductors to propagate, making them unsuitable for waveguide applications [4]. An arbitrary hollow tube such as the examples in Fig. 2.1 can only support *TE* or *TM* modes.

2.1.1.2 TE and TM Waves

TE and *TM* waves are similar in mathematical derivation and application, with the difference being that:

- for *TE* waves: $E_z = 0$; $H_z \neq 0$ and
- for *TM* waves: $E_z \neq 0$; $H_z = 0$.

Both of these modes are supported in hollow conductors (e.g. cylindrical or rectangular waveguides) and share a similar derivation and set of variables that describe them.

If the guide is a source free transmission line in a lossless and homogeneous environment close to free space (i.e. $\mu = \mu_0$ and $\epsilon = \epsilon_0$), then Maxwell's equations can be written as in Eq. 2.1.3(a) and (b) [5].

$$\nabla \times \vec{E} = -j\omega\mu\vec{H} \quad (2.1.3a)$$

$$\nabla \times \vec{H} = j\omega\epsilon\vec{E} \quad (2.1.3b)$$

Reduced TE Equations

$$H_x = \frac{-j\beta}{k_c^2} \frac{\partial H_z}{\partial x}, \quad (2.1.4a)$$

$$H_y = \frac{-j\beta}{k_c^2} \frac{\partial H_z}{\partial y}, \quad (2.1.4b)$$

$$E_x = \frac{-j\omega\mu}{k_c^2} \frac{\partial H_z}{\partial y}, \quad (2.1.4c)$$

$$E_y = \frac{j\omega\mu}{k_c^2} \frac{\partial H_z}{\partial x}. \quad (2.1.4d)$$

Reduced TM Equations

$$H_x = \frac{j\omega\epsilon}{k_c^2} \frac{\partial E_z}{\partial y}, \quad (2.1.5a)$$

$$H_y = \frac{-j\omega\epsilon}{k_c^2} \frac{\partial E_z}{\partial x}, \quad (2.1.5b)$$

$$E_x = \frac{-j\beta}{k_c^2} \frac{\partial E_z}{\partial x}, \quad (2.1.5c)$$

$$E_y = \frac{-j\beta}{k_c^2} \frac{\partial E_z}{\partial y}. \quad (2.1.5d)$$

The sets of equations given by Eq. 2.1.4 and Eq. 2.1.5 take the zero field components (e.g. $H_z = 0$ or $E_z = 0$) into account, as well as the z -dependency for a line of infinite length. The important values to note are β (the propagation constant) and k_c (the cutoff wavenumber). It can be seen that all of the transverse field components are functions of these values. There exists a simple relationship between the properties in the form of Eq. 2.1.6.

$$k_c^2 = k^2 - \beta^2, \quad (2.1.6)$$

where $k = \frac{2\pi}{\lambda} = \omega\sqrt{\mu\epsilon}$. Using boundary value conditions for a particular topology, solutions for the fields of different types of transmission lines can now be equated, including an equation for k_c . This equation, combined with Eq. 2.1.6, can be used to solve for β as well.

The propagation constant β indicates how much the phase of a signal will change over a certain length of line and is measured in radians per unit length [4]. The cutoff wavenumber k_c relates to the lower cutoff frequency by Eq. 2.1.7.

$$f_c = \frac{k_c}{2\pi\sqrt{\mu\epsilon}} \quad (2.1.7)$$

This is important when the operating range and center frequency of an application is considered [5].

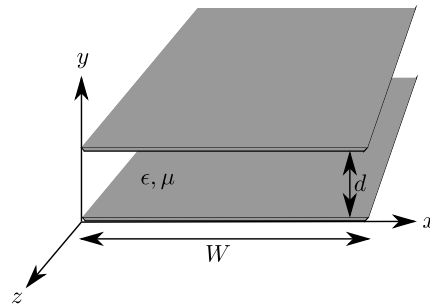
2.1.2 Parallel Plates

Figure 2.2: Parallel Plate Transmission Line

For the geometry of a parallel plate transmission line depicted in Fig. 2.2, the equation for the TE_n mode of propagation can be written as in Eq. 2.1.4.

$$H_x = 0, \quad (2.1.8a)$$

$$H_y = (j\beta/k_c) \sin(n\pi y/d) e^{-j\beta z}, \quad (2.1.8b)$$

$$H_z = B_n \cos(n\pi y/d) e^{-j\beta z}, \quad (2.1.8c)$$

$$E_x = (j\omega\mu/k_c) B_n \sin(n\pi y/d) e^{-j\beta z}, \quad (2.1.8d)$$

$$E_y = 0, \quad (2.1.8e)$$

$$E_z = 0, \quad (2.1.8f)$$

$$k_c = \frac{n\pi}{d}, \quad (2.1.8g)$$

$$\beta = \sqrt{k^2 - k_c^2}. \quad (2.1.8h)$$

In this case, H_z was calculated using the Helmholtz wave equation [5] and E_z is defined to be zero for TE waves. Note that for such a configuration, the value of $E_y = 0$. It is important to see that for a wave traveling in the z -direction, only the x -component is propagated.

In addition to the solutions to the field components, Eq. 2.1.8 also gives the solutions to the constants k_c and β , which is not only used when determining the fields, but properties such as the attenuation as well. The attenuation constant (α_d) is used to indicate how quickly a wave will be suppressed as a result of the dielectric properties of the gap between the plates. This attenuation is given by Eq. 2.1.9 and will apply to frequencies below the cutoff frequency of Eq. 2.1.7 as indicated by Fig. 2.3 [6].

$$\alpha_d = \frac{k^2 \tan \delta}{2\beta} \quad (2.1.9)$$

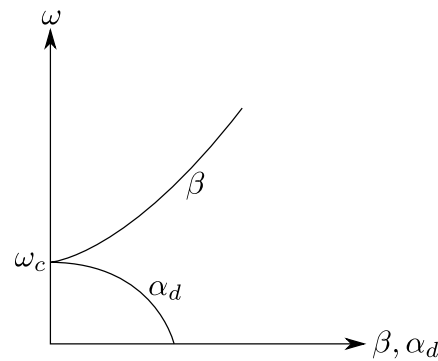


Figure 2.3: Attenuation and Propagation Constant as a Function of Frequency

2.1.3 Rectangular Waveguide

For the analysis of the rectangular waveguide properties using Maxwell's equations, the axes and waveguide properties are defined as shown in Fig. 2.4. Rectangular waveguides have been used for many decades in microwave applications, with standard bands ranging from 1 GHz up to 220 GHz [5].

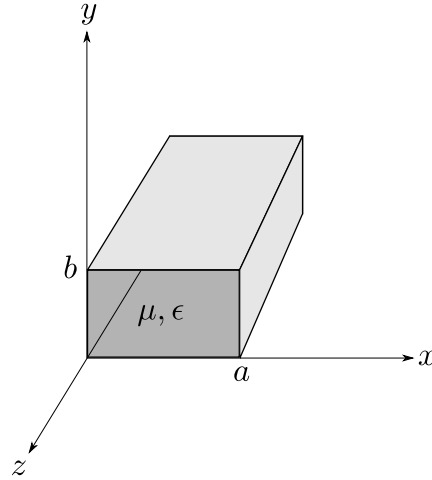


Figure 2.4: Rectangular Waveguide Dimensions and Axis System

If the walls of the waveguide are perfectly conducting, then it can be stated that

$$\vec{J}_s = \hat{n} \times \vec{H}. \quad (2.1.10)$$

The electric surface current density \vec{J}_s may exist at the boundaries of the waveguide. It is this surface current that will be interrupted in order to excite the aperture antennas, thus making it useful to know where they are flowing. Eq. 2.1.10 shows that the relationship between the magnetic field and the normal of the wall face (\hat{n}) determines the direction of the current flow. In other words, if the magnetic fields traveling in the waveguide are known, the surface currents can be determined and the aperture antenna placements can be designed. To this end, it is once again necessary to solve for the fields using Eq. 2.1.3.

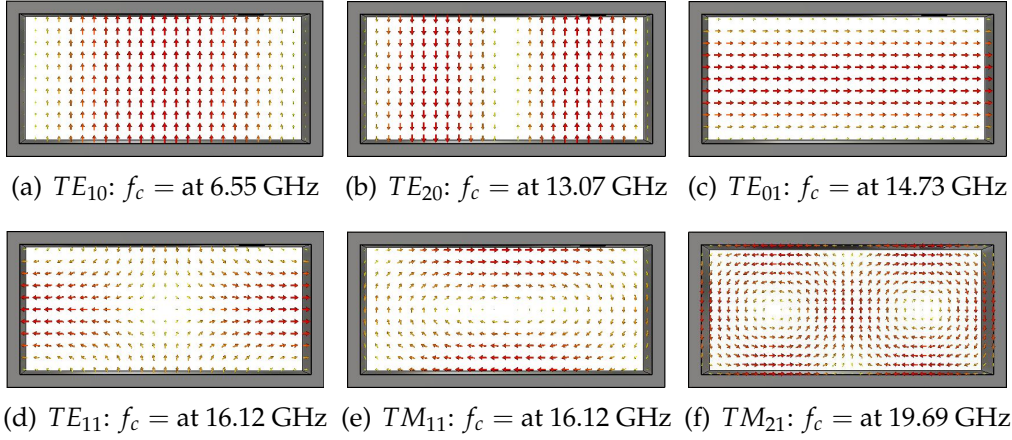


Figure 2.5: First Modes and their Cutoff Frequencies Found for the WR90 Waveguide Profile

$$H_x = \frac{j\beta m\pi}{k_c^2 b} A_{mn} \sin \frac{m\pi x}{a} \cos \frac{n\pi y}{b} e^{-j\beta z}, \quad (2.1.11a)$$

$$H_y = \frac{j\beta n\pi}{k_c^2 a} A_{mn} \cos \frac{m\pi x}{a} \sin \frac{n\pi y}{b} e^{-j\beta z}, \quad (2.1.11b)$$

$$H_z = A_{mn} \cos \frac{m\pi x}{a} \cos \frac{n\pi y}{b} e^{-j\beta z}, \quad (2.1.11c)$$

$$E_x = \frac{j\omega\mu n\pi}{k_c^2 b} A_{mn} \cos \frac{m\pi x}{a} \sin \frac{n\pi y}{b} e^{-j\beta z}, \quad (2.1.11d)$$

$$E_y = \frac{-j\omega\mu m\pi}{k_c^2 a} A_{mn} \sin \frac{m\pi x}{a} \cos \frac{n\pi y}{b} e^{-j\beta z}, \quad (2.1.11e)$$

$$E_z = 0, \quad (2.1.11f)$$

$$k_c = \sqrt{(m\pi/a)^2 + (n\pi/b)^2}, \quad (2.1.11g)$$

$$\beta = \sqrt{k^2 - k_c^2}. \quad (2.1.11h)$$

The TE_{mn} waves shown by Eq. 2.1.11 are a general set of solutions to the boundary value problems and the Helmholtz wave equation (for H_z). Here the values m and n indicate the mode in the a and b dimension of the waveguide respectively. In other words, m is an indication of the number of half-wavelengths that can fit into the a dimension of the waveguide, where n is the number of half-wavelengths of the same frequency can fit into the b dimension. Fig. 2.5 shows some of the first modes encountered for a WR90 waveguide profile.

Another important property is that of the *waveguide wavelength* (λ_g), which is defined as the distance between two planes in the propagating axis with the same phase [5]. It is defined as in Eq. 2.1.12a for TEM waves and Eq. 2.1.12b for TE and TM waves.

$$\lambda_g = \frac{2\pi}{k} \quad (2.1.12a)$$

$$\lambda_g = \frac{2\pi}{\beta} \quad (2.1.12b)$$

Rectangular homogeneous waveguides can only propagate *TE* and *TM* modes, so the focus here is on Eq. 2.1.12b. For the TE_{10} mode, Eq. 2.1.12b can also be written as in Eq. 2.1.13a.

$$\lambda_g = \frac{2\pi}{\beta} \quad (2.1.13a)$$

$$= \frac{2\pi}{\sqrt{k^2 - k_c^2}} \quad (2.1.13b)$$

$$= \frac{2\pi}{\sqrt{\left(\frac{2\pi}{\lambda}\right)^2 - \left(\frac{\pi}{a}\right)^2}} \quad (2.1.13c)$$

Insight can be gained from this representation when the operating frequency (λ) is compared to the physical dimension a . The waveguide wavelength is not defined below the cutoff frequency. If, however, the operating frequency tends toward the cutoff frequency, the denominator terms cancel and λ_g tends toward infinity. At very high frequencies, the minus term becomes negligible and λ_g tends toward zero. These conclusions are presented in Eq. 2.1.14a.

$$\lambda \rightarrow 2a \implies \lambda_g \rightarrow \infty \quad (2.1.14a)$$

$$\lambda \rightarrow \infty \implies \lambda_g \rightarrow 0 \quad (2.1.14b)$$

The reason the waveguide wavelength is such an important term, is that it will determine the element spacing and the phase difference between elements in an array. Two elements, placed λ_g apart will be in phase. Also, the relationship between λ_g and the physical dimensions of the waveguide plays an important role when the waveguide profile is considered.

If any mode other than the primary mode (TE_{10}) is used, then the frequency of the signal will be higher, but the waveguide will still have the same physical dimensions. Since it is often useful to use the smaller dimension, these modes are often avoided. Once a higher mode starts to propagate, the lower mode does not cease propagating. This means that there will be a superposition of modes running simultaneously, which complicates the design process. There is also the question of mathematical convenience. Note that when the TE_{10} mode is used, Eq. 2.1.11 simplifies to Eq. 2.1.15.

$$H_x = \frac{j\beta\pi}{k_c^2 b} A_{10} \sin \frac{\pi x}{a} e^{-j\beta z}, \quad (2.1.15a)$$

$$H_y = 0, \quad (2.1.15b)$$

$$H_z = A_{10} \cos \frac{\pi x}{a} e^{-j\beta z}, \quad (2.1.15c)$$

$$E_x = 0, \quad (2.1.15d)$$

$$E_y = \frac{-j\omega\mu\pi}{k_c^2 b} A_{10} \sin \frac{\pi x}{a} e^{-j\beta z}, \quad (2.1.15e)$$

$$E_z = 0, \quad (2.1.15f)$$

$$k_c = \frac{\pi}{a}, \quad (2.1.15g)$$

$$\beta = \sqrt{k^2 - k_c^2}. \quad (2.1.15h)$$

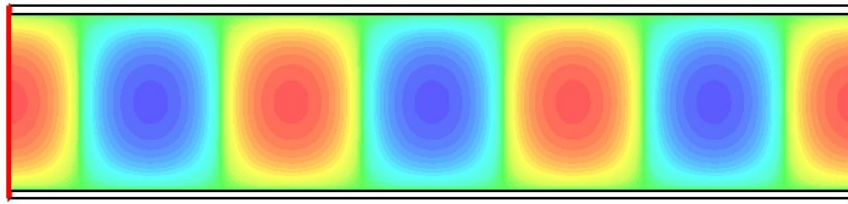
Both Fig. 2.6(a) and Fig. 2.6(b) depict the TE_{10} Electric field component. Fig. 2.6(b) shows the half-wavelength in the a -dimension of the waveguide, where Fig. 2.6(a) shows a cut from the waveguide from some constant z -value inside the waveguide. Here the sinusoidal nature of the wave can be seen that is described by Eq. 2.1.15e. The H-field is shown in Fig. 2.6(c) with arrows indicating the direction that the field is moving. Finally, the surface current J_s is depicted in Fig. 2.6(d). The currents flowing on the top and bottom of the waveguide flow in the same direction.

A similar set of equations can be found for the TM mode. The dependency of the results for the TM mode on m and n are such that if either m or n is equal to zero, that all of the field components are zero. The primary mode for TM waves in a rectangular waveguide is then TM_{11} .

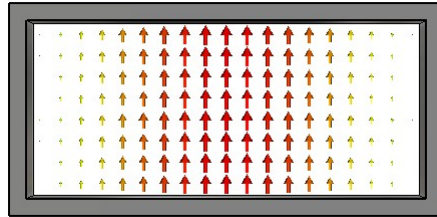
2.1.4 Ridged Waveguide

Ridged waveguides are popular for many applications due to their large inherent bandwidth and low characteristic impedance [4, 7]. Here the bandwidth refers to the ratio between the cutoff frequencies of the second and primary propagation modes [8]. An example of a single ridged waveguide and common notation is given in Fig. 2.7.

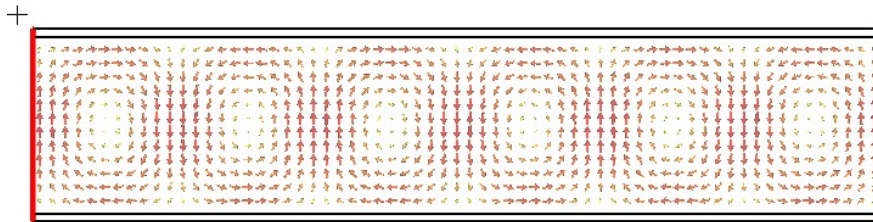
Typically, designing ridged waveguide requires tools such as tables [8], design diagrams, graphs, or mathematical approximations [7]. The tables provide curves for performance properties vs. the physical dimensions given in Fig. 2.7(b), but are often restricted to a small subset of values [8]. For this reason, the mathematical approximations are useful in that they allow for any arbitrary values. These, however, are also only approximations [7] and quickly become complicated. For example, an important equation that relates the ratio of the waveguide height to the cutoff frequency is given by Eq. 2.1.16, which is a corrected perturbation formula for analyzing ridges of finite width [7].



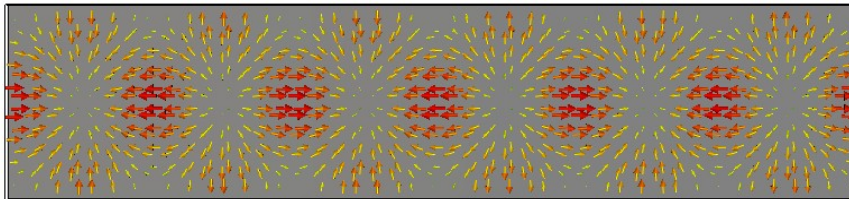
(a) E-Field of a TE_{10} Wave Along the Waveguide



(b) E-Field TE_{10} Mode in a Rectangular Waveguide (at the Port)



(c) H-Field of a TE_{10} Wave Along the Waveguide



(d) Surface Current J_s of a TE_{10} Wave Along the Waveguide

Figure 2.6: TE_{10} Mode Fields and Currents

$$\frac{b}{\lambda_{cr}} = \frac{\frac{b}{2(a-s)}}{\sqrt{1 + \frac{4}{\pi} \left(1 + 0.2\sqrt{\frac{b}{a-s}}\right) \frac{b}{a-s} \ln \csc \frac{\pi d}{2b} + (2.45 + 0.2\frac{s}{a}) \frac{sb}{d(a-s)}}} \quad (2.1.16)$$

The equation works to within 1% accuracy under most conditions; this

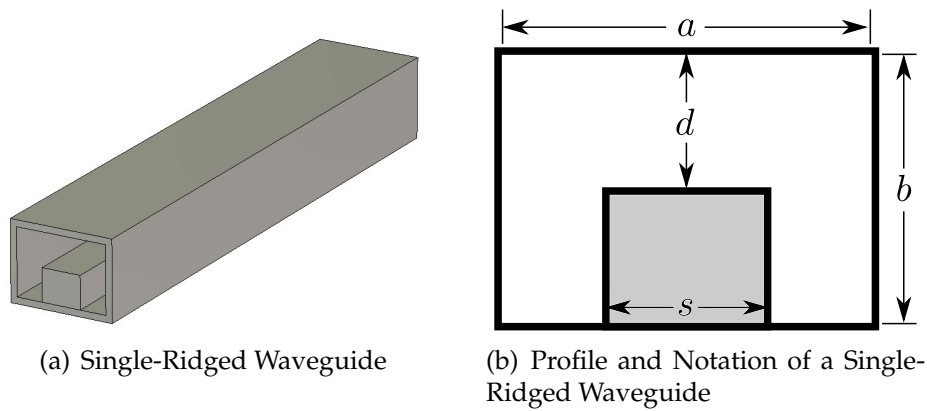


Figure 2.7: Single-Ridged Waveguide

value was verified by comparing the calculated results to those of numerical methods [7]. With the computational power available today, numerical methods and simulation tools are being used more frequently and for more complex problems.

In chapter 3, a simulation-based approach is used to characterize the properties of a waveguide and an independent reasoning is provided.

2.2 Aperture Antennas

When dealing with aperture antennas it is important to understand the basic concept of how they function. A fundamental scientific understanding allows for more efficient designs and new approaches to problems. Also, the models used to describe the apertures are very useful in the design process. By creating abstractions that accurately predict the behavior of an aperture antenna, the design process can be simplified.

2.2.1 Babinet's Principle

Apertures cut into a conducting plane are referred to as *aperture antennas*. Aperture antennas became popular once the relationship between the aperture antenna and its complementary antenna was discovered. Initially Babinet's Principle, which is the theory that describes this relationship, was limited to optics only. Babinet's argument states that if you take a screen with shapes cut out of it, you will get a pattern or shadow that is the exact inverse of when a screen with only those shapes (i.e. the shapes that form a *complementary screen*) are used. Fig. 2.8 shows two configurations, where the top is an aperture cut into a conducting screen and the bottom shows the complementary dipole.

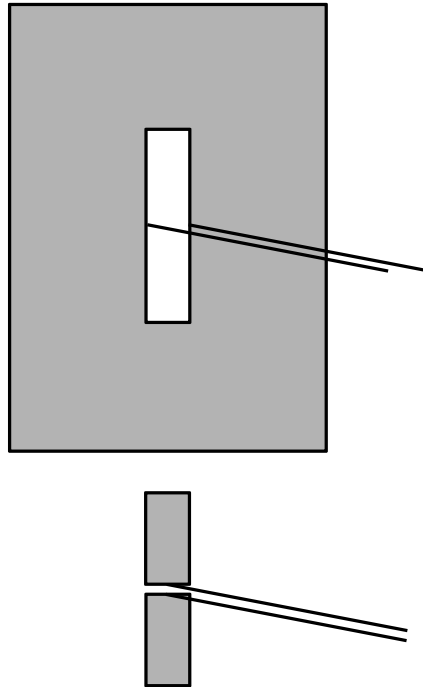


Figure 2.8: An Aperture Cut in a Screen with its Complementary Component

Booker [9] summarized this principle and expanded the theory to include the effect of polarization. He concluded that the radiation through an aperture holds to Babinet's principle, but that it is necessary to rotate the complementary screen by a right angle to get the radiated fields to add in such a way that the field appears to originate from an uninterrupted source. In order to satisfy the boundary conditions at the surface of the screen, it was necessary to do the rotation to get the complementary screens to provide the correct polarization for the complementary fields to add continuously.

Special attention was also given to the rectangular aperture antenna and its complementary structure, namely a flat thin dipole. Booker excited the aperture by adding a current source in the center, much like in a dipole. The currents then flow around the aperture and build up charge on one side, which causes an electric field to form across the aperture. This behavior, depicted in Fig. 2.9 can also be modeled as a transmission line that is short-circuited at the ends [9].

If a pure sinusoidal excitation is given, the aperture can be described in terms of where the current flows during each half-cycle of the excitation. When considering the first half cycle, the current flows from the negative terminal to the positive terminal. If the transmission path is sufficiently long (typically $\frac{\lambda_0}{2}$ or longer), a charge builds up and an electric field is formed across the gap. During the second half-cycle the polarity is reversed and

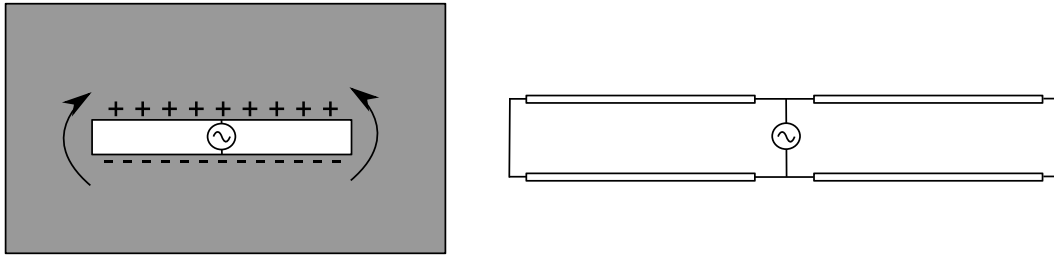


Figure 2.9: Aperture Excitation and Transmission Line Model

current flows in the opposite direction.

The important thing to note is that the field across the gap depends on the current flowing around the aperture. In this example, the current was produced by a source in the center of the aperture. However, the same behavior can be obtained if the aperture is placed in an environment where current is already flowing, which is the case for apertures cut into the wall of a waveguide. By placing the aperture in a region with a stronger current, it is similar to increasing the amplitude of the excitation in Fig. 2.9. Looking back at the TE_{10} modes of propagation in section 2.1.3, the location of the stronger surface currents are known. By placing an aperture in the path of the currents, the aperture can be excited and energy radiated.

Even though the relationship between the impedance properties of complementary structures has been analyzed [9, 10], it is of little use if the impedance is unknown for either of the complementary structures. The rest of this section deals with characterizing the aperture antennas and analyzing their equivalent circuit properties.

2.2.2 Equivalent Circuit Properties of Aperture Antennas

For slotted waveguide applications, it is useful to discuss the impedance of the aperture antennas (or slots) in a waveguide environment. This concept of normalized impedance helps generalize the design process and reduces the number of parameters that must be calculated (such as the waveguide's impedance). By characterizing aperture antennas with different physical parameters in terms of equivalent circuit models, transmission line theory can be used to design an antenna array with these models as elements on the line.

Stevenson [11] solved the fields involved with apertures by solving a set of boundary value problems. He determined that, since the fields must be continuous, it is possible to find fields inside and outside the apertures that satisfy the boundary value conditions. He also introduced the concept of impedance and admittance by looking at the energy balance. He stated that the radiated energy is related to the real part of the impedance, where the Q-factor (or the "sharpness" of the resonance, with resonant fractional

bandwidth approximately equal to $\frac{1}{Q}$) helps to determine the complex part of the impedance. He made use of the complementary structures discussed in 2.2.1 to determine the impedance (or rather, admittance) of a rectangular aperture in a rectangular waveguide. The rectangular aperture relates to a thin flat dipole (as in Fig. 2.8), whose impedance properties are known.

This work was further developed by Oliner [12, 13, 14], who included the effect of wall thickness in his analysis [12, 13]. The wall thickness is represented as a short transmission line (i.e. a short piece of waveguide) with its own characteristic impedance. This line is placed in front of the aperture as calculated by [11] and the resulting input impedance is taken as the new value. Experimental results [13] showed that this approach improves the estimated aperture antenna impedance.

Also, the concept that the Q-factor can be used as a means to determine the reactive component of the aperture is reinforced. Oliner showed that the Q-factor and the resonant length should remain relatively constant over frequency, provided the aperture width and wall thickness stays the same. Experimental data revealed that this assumption also fails if the aperture is placed near the sidewall of the waveguide.

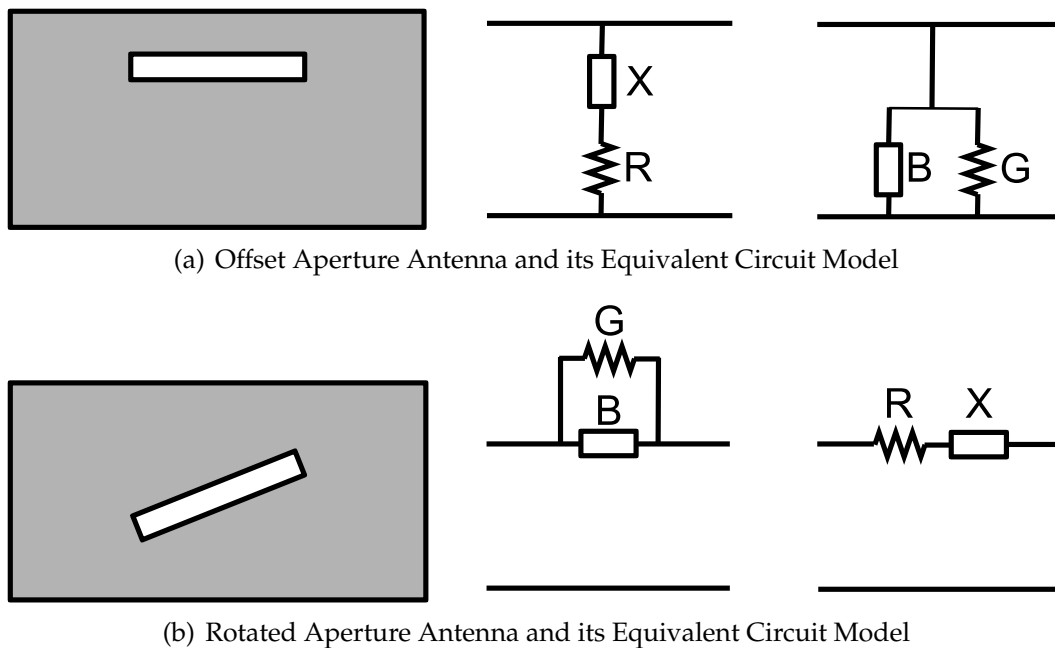


Figure 2.10: Equivalent Circuit Models for Offset and Rotated Aperture Antennas

For two of the aperture antennas that were analyzed, the equivalent models are depicted in Fig. 2.10. It should be noted that these models are approximations. A more appropriate model would be a T or Π model. This would require another parameter to be defined. Due to the symmetrical nature of the apertures, the “left” and “right” sides of a Π and T model will be

identical [14, 15], meaning that it only needs to be determined once. It has been found that, in practice, the shunt and series models shown in Fig. 2.10 are sufficient.

2.3 Transmission Line Theory

It stands to reason that if waveguides are a type of transmission line, and the apertures can be modeled as circuit elements, that it could be useful to understand some of the basic principles of high frequency transmission line theory. Specifically, it is useful to know the magnitude and phase of all voltages and currents in the system, in order to determine whether the elements are excited correctly and if not, by how much to adjust them.

The cascaded nature of the antenna suggests that the ABCD Parameters will be useful in analyzing the model. For example, the antenna can be modeled as a length of transmission line, then either a series impedance or a shunt admittance (depending on the aperture's equivalent model), followed by another piece of transmission line. This is repeated until all of the elements are included. Fig. 2.11 shows such a configuration, where each block represents either a length of line or a circuit element [5].

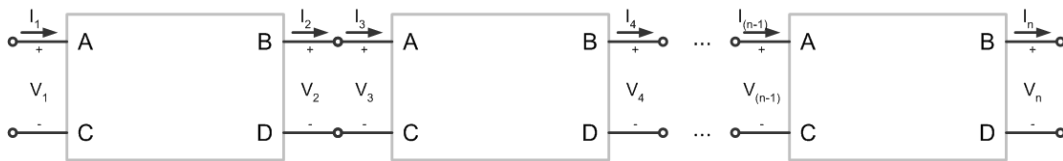


Figure 2.11: Cascaded ABCD Parameters

2.3.1 ABCD Parameters

ABCD Parameters are a representation of a two-port network. Fig. 2.12 shows how the currents and voltages are defined at the input and output, where Eq. 2.3.1 shows the matrix form of the network.

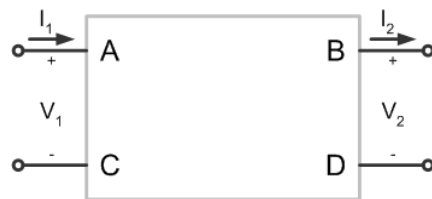


Figure 2.12: Two-Port ABCD Network

$$\begin{bmatrix} V_1 \\ I_1 \end{bmatrix} = \begin{bmatrix} A & B \\ C & D \end{bmatrix} \begin{bmatrix} V_2 \\ I_2 \end{bmatrix} \quad (2.3.1)$$

By defining the set of coefficients A , B , C and D for different types of circuit elements, the voltage and current before and after each component can be calculated.

2.3.1.1 Length of Transmission Line

A lossless transmission line, for example, maintains the magnitude of the voltage and current at the input, but adds a phase shift. The model is shown in Fig. 2.13.

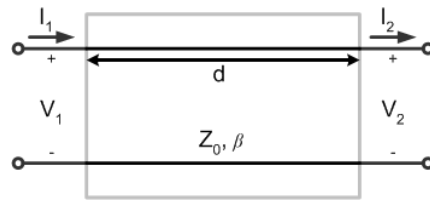


Figure 2.13: ABCD Representation of a Transmission Line

$$\begin{bmatrix} A & B \\ C & D \end{bmatrix} = \begin{bmatrix} \cos(\beta d) & jZ_0 \sin(\beta d) \\ jY_0 \sin(\beta d) & \cos(\beta d) \end{bmatrix} \quad (2.3.2)$$

The propagation coefficient β is a value indicating how quickly the phase of an input signal will change on a transmission line. The value Z_0 represents the characteristic impedance of the line, and the value d represents the length of the line. Eq. 2.3.2 gives the equivalent ABCD matrix.

2.3.1.2 Series Impedance

By simple reasoning and use of Ohm's Law, the model for a series impedance can be derived. The model is shown in Fig. 2.14. It is expected that a voltage drop occurs over the impedance ($V_Z = Z \times I_1$) and that the current remains the same. This behavior can be represented by the ABCD matrix given in Eq. 2.3.3.

$$\begin{bmatrix} A & B \\ C & D \end{bmatrix} = \begin{bmatrix} 1 & Z \\ 0 & 1 \end{bmatrix} \quad (2.3.3)$$

2.3.1.3 Shunt Admittance

The reasoning for finding the model of a parallel admittance is similar to that of the series impedance in 2.3.1.2. The only difference is that now the

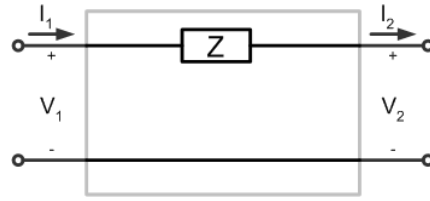


Figure 2.14: ABCD Representation of a Series Impedance

value is a parallel admittance in stead of a series impedance. The model is shown in Fig. 2.15 and the equivalent ABCD matrix is given by Eq. 2.3.4.

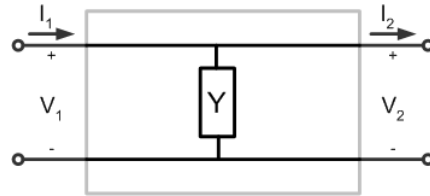


Figure 2.15: ABCD Representation of a Parallel Admittance

$$\begin{bmatrix} A & B \\ C & D \end{bmatrix} = \begin{bmatrix} 1 & 0 \\ Y & 1 \end{bmatrix} \quad (2.3.4)$$

2.3.1.4 Cascading Example

An example of a cascaded system is given by Fig. 2.16, which depicts a parallel admittance connected to a series impedance.

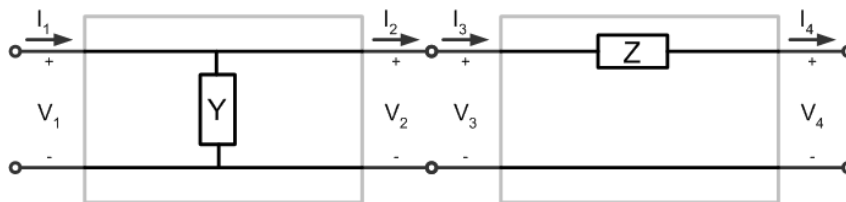


Figure 2.16: Example of a Cascaded ABCD Network

If the voltage and current at the output is known (V_4 and I_4 respectively), then the input voltage and current is given by Eq. 2.3.5.

$$\begin{bmatrix} V_1 \\ I_1 \end{bmatrix} = \begin{bmatrix} 1 & 0 \\ Y & 1 \end{bmatrix} \begin{bmatrix} 1 & Z \\ 0 & 1 \end{bmatrix} \begin{bmatrix} V_4 \\ I_4 \end{bmatrix} \quad (2.3.5)$$

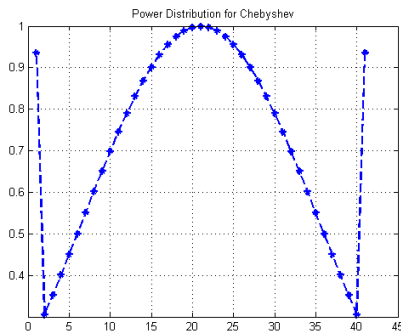
This type of cascading can be performed indefinitely with any element for which the ABCD matrix is known. Only the elements described in this section will be used.

2.4 Array Synthesis

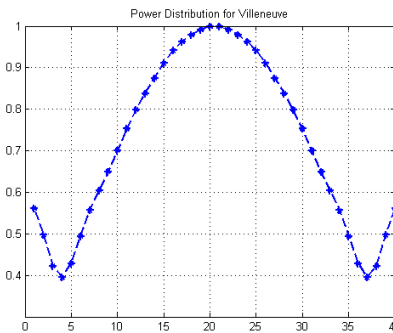
An antenna that is constructed of a linear array of elements is referred to as linear array. The synthesis of such an array requires the control of at least one of the following properties [16]:

1. the geometry of the array (i.e. the placement of the elements);
2. the amplitude and phase of each individual excitation; or
3. the individual radiation pattern of the elements.

The Dolph-Tschebyscheff distribution [16] is used when the beamwidth must be minimized for a given sidelobe level. Since the sidelobe level is all that is of concern for this design, the Dolph-Tschebyscheff distribution appears to be a sensible solution. However, upon further inspection, the edge elements of the weighting distribution flare in order to provide the necessary pattern. This is depicted in Fig. 2.17(a), note that the excitation of the first and final element jump to more than double the level of the adjacent elements. This is undesirable when coupling needs to be considered.



(a) 40 Element Tschebyscheff Excitation



(b) 40 Element Villeneuve Excitation

Figure 2.17: Element Excitations for Two 40 Element Arrays

As an alternative, the Villeneuve distribution is considered [17]. It is an implementation of Taylor patterns for discrete arrays, which is developed without making any approximations. This distribution reduces the edge flaring (Fig. 2.17(b)) whilst maintaining the same sidelobe level as the Dolph-Tschebyscheff distribution.

The specific distribution is not relevant for this study, as the antenna is not intended to be used for any particular radar application. However, the Villeneuve distribution provides a convenient distribution that is easily implemented.

2.5 Waveguide Slot Arrays

When designing a slotted waveguide array, a single stick (or linear array) must first be considered (this discussion follows from [18]). A planar array is then designed by placing these sticks next to each other. Two main classes of slotted waveguide arrays are considered, namely

- standing-wave or
- traveling-wave

arrays. A standing-wave array has elements spaced $d = \lambda/2$ apart and radiates toward broadside. In contrast, the traveling-wave array has elements spaced $d \neq \lambda/2$ apart, leading to the main beam scanning with frequency and radiating off broadside at the operating frequency.

2.5.1 Standing-Wave Arrays

Linear slot arrays with resonant slots are a class of standing-wave arrays that is commonly used in radar. The elements are spaced exactly $d = \lambda/2$ apart and in phase, leading to a radiation pattern directed in the broadside direction. The term broadside refers to the direction perpendicular to the array elements (as shown by the azimuth = 90° in Fig. 1.1).

An example of a standing wave slotted waveguide antenna is given in [19], where a ridged waveguide is used to help extend the scanning angle of a frequency scanned antenna. This work done in [19] ties in very closely to what is done here, as the basic topology of the antenna is similar. It may be useful to note the difference in approach between the work done here and that of Kim and Elliott. Their approach relies heavily on analytical approximations for the apertures, which quickly become complicated and difficult to work with. The aim here is to devise an approach that is independent of the specific aperture used, so that it may be applied to various configurations without alteration.

For this type of antenna, the radiation pattern deteriorates quickly if the frequency deviates from the operating frequency. In order to obtain a higher frequency-bandwidth, the traveling-wave array is considered.

2.5.2 Traveling-Wave Arrays

Traveling-wave arrays tend to have a higher frequency-bandwidth performance than the standing-wave arrays, particularly if all elements are designed to be resonant at the operating frequency. The focus here is on the uniformly spaced type of array, that produces a pencil beam with low side-lobes.

In traveling-wave arrays, the power radiated by each element subtracts from the power available to the remaining elements. The final elements must then radiate the remaining power for a high efficiency design. However, an element is incapable of radiating 100% of the remaining power (typically they are limited to approximately 30%). A terminating load is placed at the end of the array to absorb the remaining power. This reduces the power that must be radiated by the final few elements, allowing for more reasonable element. This relation is shown in Eq. 2.5.1.

$$P_{in} = P_{allslots} + P_{load} = \sum_{i=1}^N p_i + P_L \quad (2.5.1)$$

The sum of the power radiated by each of the elements (p_i) as well as the load power (P_L) must equal the input power for a perfectly matched, lossless system. Note that after the first element, the remaining power is $P_{in} - p_1$, which means that p_2 must radiate a larger percentage of the input power to maintain the desired element excitation.

By placing elements $d \neq \lambda/2$ apart, the direction of the main beam is influenced. The precise deviation is frequency and spacing dependent as can be shown by Eq. 2.5.2.

$$\sin \theta = \frac{\lambda}{\lambda_g} - \frac{(N - 1/2)\lambda}{d} \quad (2.5.2)$$

The important thing to note is that if $d > \lambda_g/2$, the beam angle is moved toward the load. The beam angle is moved toward the feed for $d < \lambda_g/2$. For the case where $d = \lambda_g/2$, the reflections off of each element adds in phase and the cumulative wave is reflected back to the source, which in turn lowers the efficiency of the antenna.

For the antennas of interest, it will be necessary to select an appropriate element spacing and load power. The load power will be determined by the maximum amount of power that can be radiated by an element, where the element spacing will be determined by the return loss of the antenna.

Chapter 3

Design of the Waveguide Transmission Line

The antenna specifications require a certain operating frequency f_0 . The transmission line that carries energy through the antenna must therefore also adhere to a certain frequency specification. The physical dimensions of the antenna are also of interest. A constraint in the width of the waveguide is included in the specifications. Consideration is given to commercially available waveguides, as well as customized waveguides, with the aim of finding one that adheres to the antenna specification.

3.1 Waveguide Specifications

The final design calls for an X-band antenna [2]. The specific operating frequency is not important; a value will be chosen here to help with explaining some of the principles in this chapter. The specifications chosen for this design are given in Tab. 3.1.

Table 3.1: Waveguide Specifications

Symbol	Property	Value
f_0	Center Frequency	10.5 GHz
BW	Bandwidth	1 GHz
tol	Cutoff Frequency Tolerance	20%
	Primary TE Mode	–
a	Maximum a -value	16 mm

In other words, Tab. 3.1 states that a waveguide operating in the primary TE mode (TE_{10} mode for rectangular waveguides) is required to propagate a range of frequencies around f_0 such that the bandwidth BW is achieved. It

also indicates a design tolerance for the cutoff frequencies, in effect increasing the desired bandwidth. This information is summarized in Fig. 3.1.

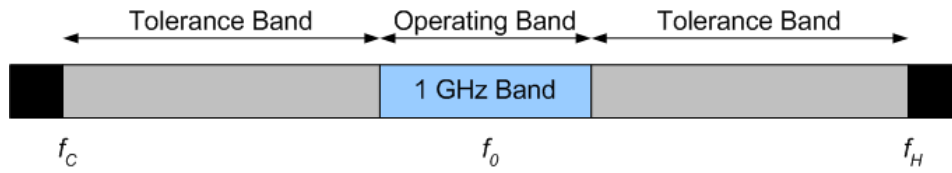


Figure 3.1: Depiction of Waveguide Specifications

Fig. 3.1 introduces the symbols f_c and f_H , representing the lower and higher cutoff frequencies respectively. With the specifications given in Tab. 3.1, these values can be represented as in Eq. 3.1.1. Note that the percentage value of tol is used here as a value between 0 – 1.

$$f_c = \frac{(f_0 - BW/2)}{1 + tol} = 8.3 \text{ GHz} \quad (3.1.1a)$$

$$f_H = (f_0 + BW/2) \times (1 + tol) = 13.2 \text{ GHz} \quad (3.1.1b)$$

To obtain a waveguide that will adhere to the specifications in Tab. 3.1, only the values in Eq. 3.1.1 need to be applied to design the cutoff frequencies of the TE_{10} mode of operation.

3.2 Properties of Rectangular Waveguides

A standard rectangular waveguide is shown in Fig. 3.2. The TE_{10} mode is depicted in Fig. 2.6.

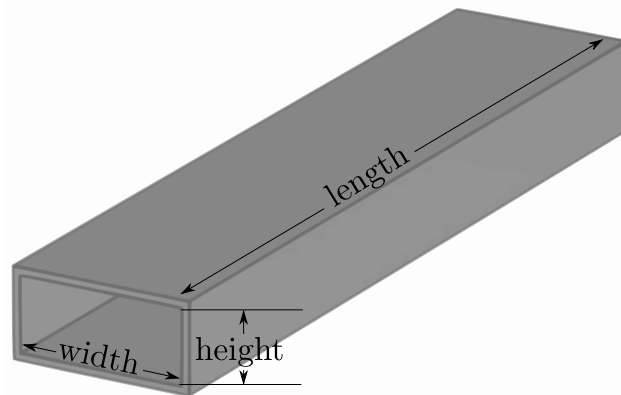


Figure 3.2: Standard Rectangular Waveguide

According to Microwave Encyclopedia [20], only two standard rectangular waveguide profiles will allow an operating frequency of f_0 to propagate in the TE_{10} mode. Tab. 3.2 shows these two profiles and some of their properties. Both profiles were also simulated in CST Microwave Studio to determine the actual cutoff values without any tolerances considered.

Table 3.2: Standard Rectangular Waveguide Profiles

Name	Frequency Range [GHz]	CST Range [GHz]	Dimensions [mm]
WR90	8.20 – 12.5	6.55 – 13.07	22.86×10.16
WR75	9.54 – 15.0	7.87 – 15.68	19.05×9.525

It would be recommended to consider this profile for X-band applications in the region near f_0 due to its availability and cost. However, the specifications in Tab. 3.1 state that the maximum width of the waveguide profile must be 16 mm. The WR75 profile is too wide for this application, meaning that custom waveguides must be considered.

3.3 Design of a Ridged Waveguide

If any of the values in Tab. 3.1 were to change, it may be possible that no standard rectangular waveguide exists with the desired bandwidth and operating frequencies. The maximum width specification (a) is not met with any of the standard rectangular guides. By adding a ridge to a waveguide with a custom rectangular profile, it is possible to design a waveguide profile for which there are specific cutoff frequencies and physical dimensions. Fig. 3.3 again shows a typical ridged waveguide and its notation as in Fig. 3.3(b).

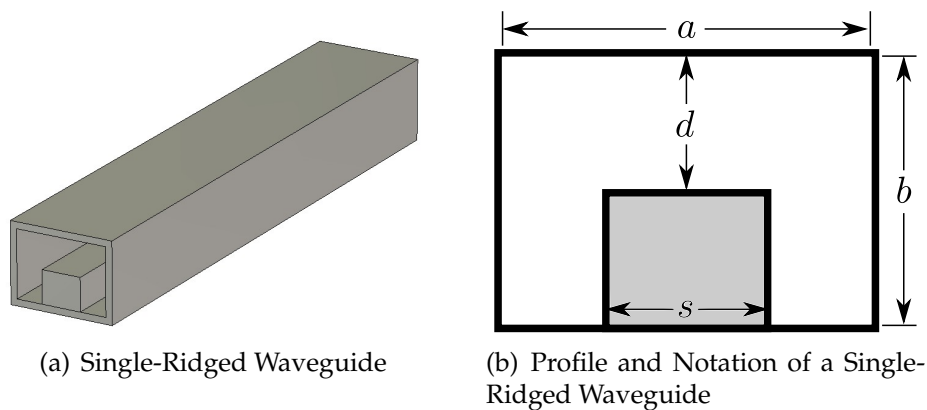


Figure 3.3: Single-Ridged Waveguide

3.3.1 Approach to Understanding Ridged Waveguides

Take, as a starting point, the standard WR90 rectangular waveguide from the previous section. It has a simulated lower cutoff frequency of $f_C = 6.55$ GHz. This corresponds exactly to the predicted cutoff frequency implied by Eq. 2.1.15g, where the cutoff wavenumber can be interpreted as shown in Eq. 3.3.1.

$$k_c = \frac{\pi}{a} \quad (3.3.1a)$$

$$\text{and } k_c = \frac{2\pi}{\lambda_c} \quad (3.3.1b)$$

$$\Rightarrow \lambda_c = \frac{2\pi}{k_c} \\ \therefore \lambda_c = 2a \quad (3.3.1c)$$

The implication of Eq. 3.3.1c is that if the width of the waveguide is reduced to conform to the physical specification in Tab. 3.1, the cutoff wavelength will be reduced and the cutoff frequency will increase. By adding a ridge, the cutoff frequency can be lowered again as a result of the additional capacitance.

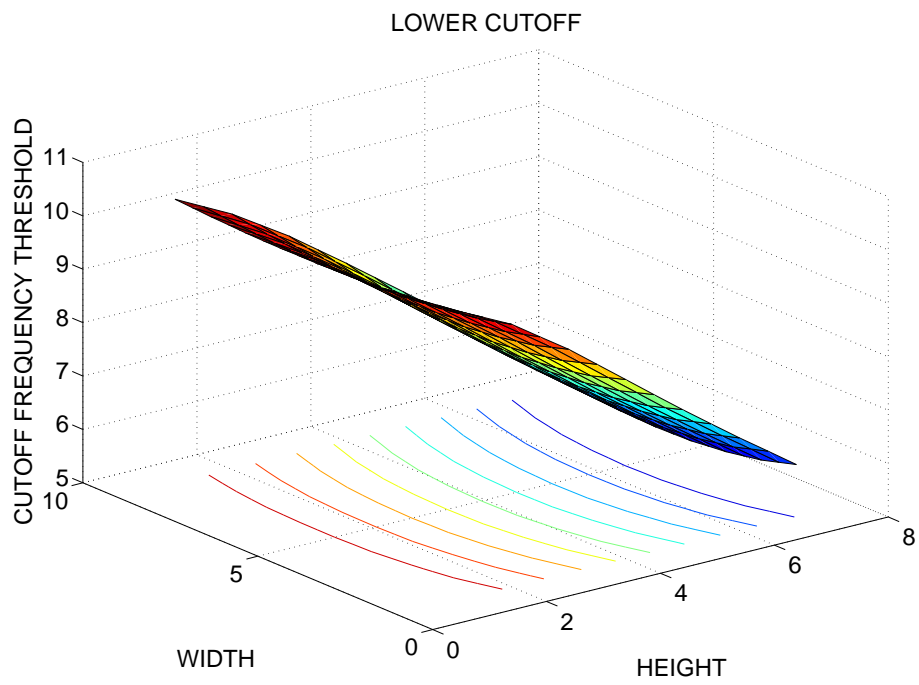
By sweeping the values d and s in Fig. 3.3(b), the cutoff frequency for the first and second cutoff frequencies can be determined and a suitable combination can be chosen. The two dimensions that are swept in the simulations are the *width* of the ridge (s) and the *height* of the ridge ($b - d$).

The first and second cutoff frequencies are stored and shown in Fig. 3.4.

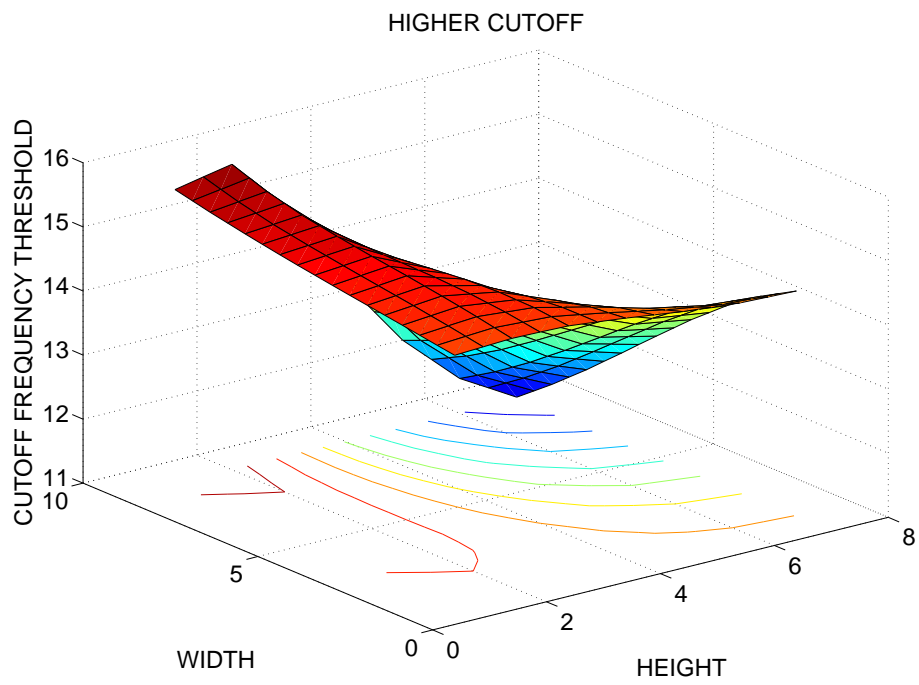
3.3.2 Simulation Results for Parameter Sweep

A brute force numerical method is applied to obtain the physical dimensions that provides the desired performance required by the specifications in Tab. 3.1. The inside width a must be no more than 16 mm. A value of $a = 14$ mm is chosen, where b is kept the same as with the standard rectangular profile WR90. In other words, the wide dimension of a rectangular waveguide is shortened, raising the lower cutoff frequency. By adding a ridge with the right dimensions, the cutoff frequencies can be tuned to the desired specifications.

All values for the lower cutoff frequency below f_C are acceptable and all values above f_H is acceptable for the specifications given. It is necessary to find the region where both these criteria are met. Fig. 3.5 shows this region. The red indicates all the combinations of values that will provide a ridged waveguide with the desired cutoff frequencies.



(a) Lower Cutoff Frequencies



(b) Higher Cutoff Frequencies

Figure 3.4: Cutoff Frequencies of a Ridged Waveguide with a Fixed a and b

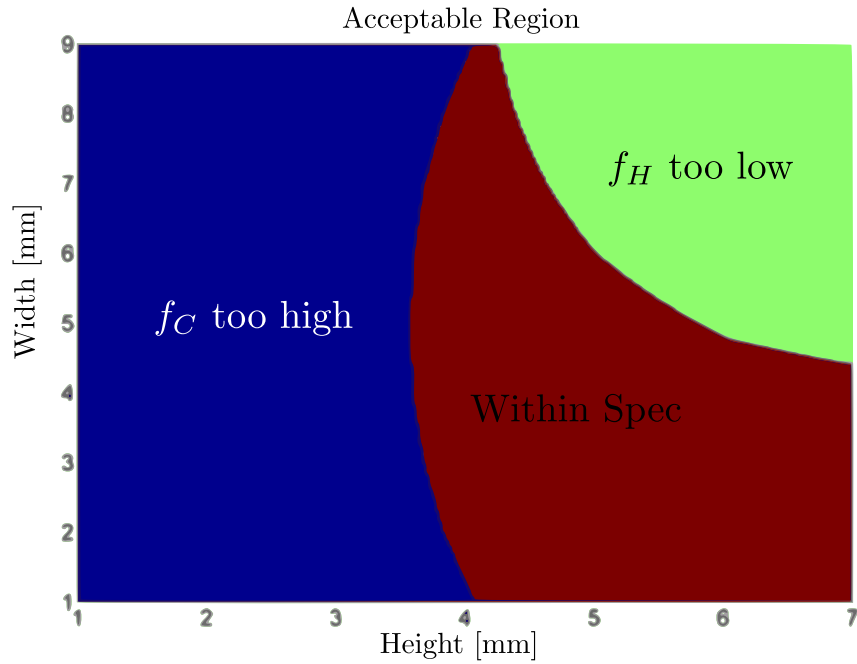


Figure 3.5: Region Where Both the Lower and Higher Cutoff Frequency Specifications are Met

3.3.3 Final Design of Ridged Waveguide

From the result in Fig. 3.5 it is clear that there are many solutions to the correct operating bandwidth of a ridged waveguide. To verify the validity of the design values of Fig. 3.5, a borderline case is taken and confirmed with an individual simulation. A ridge height of $(b - d) = 5$ mm and a ridge width of $s = 6$ mm is chosen as the confirmation values. The physical dimensions of the waveguide profile are provided in Tab. 3.3 and Fig. 3.6.

Table 3.3: Properties of Final Ridged Waveguide Design

Property	Value
a	14 mm
b	10.16 mm
s	6 mm
d	5.16 mm
$(b - d)$	5 mm
f_C	7.15 GHz
f_H	13.21 GHz

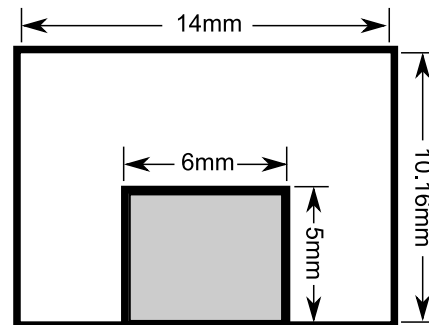


Figure 3.6: Physical Dimensions of Final Ridged Waveguide

The dimensions chosen lies close to the border between the acceptable region and the region where f_H is too low in Fig. 3.5. This border is defined

by the higher cutoff frequencies. In other words, the green region to the “right” of the acceptable region are for those values for which the second cutoff frequency is lower than the desired cutoff value. It therefore makes sense that the chosen f_H is close to the design limit. The lower cutoff frequency f_C , however, is well within its tolerance. This is because it is far away from the blue region, where the lower cutoff frequency is higher than f_C . From the discussion of the waveguide wavelength (λ_g) and the conclusions drawn in Eq. 2.1.13b, it can be seen that a lower cutoff frequency corresponds to a shorter waveguide wavelength. This, in turn, serves to shorten the physical length of an array.

With the combination of the behavior of the surfaces given by Fig. 3.4(a) and Fig. 3.4(b) and the acceptability threshold provided by Fig. 3.5, many physical properties can be found that will generate a valid ridged waveguide. Similar curves can be made for any combination of a and b . All other ridged waveguides considered for the final application have the dimensions given in Tab. 3.3.

Chapter 4

Analysis of Aperture Radiators

An exhaustive discussion of aperture radiators can easily distract from the final aim of finding a suitable element for the waveguide antenna array. A subset of the more interesting properties are discussed and analyzed with respect to several aperture antenna types. A common and well-understood aperture antenna is discussed, as well as some arbitrary aperture configurations. The aim is to determine what slot to use in the final design, but also to verify the method used for analyzing the arbitrary aperture shapes.

4.1 Discussion of Slot Properties of Interest

Section 2.2 provided a broad discussion on how aperture antennas are excited, along with the equivalent circuit model and the notion of placement of apertures in a waveguide relating to its amplitude excitation. In all studies, the waveguides are designed to make use of the TE_{10} mode.

It is generally understood that an aperture antenna's *radiating frequency* can be tuned by its length. The *amplitude*, depending on the shape of the aperture and configuration, can be tuned by rotating the aperture or by changing the aperture's offset from the center of the waveguide. For the sake of simplicity, it is assumed that the resonant frequency is the frequency where the maximum energy is being radiated. The amplitude is also assumed to be proportional to the radiated power.

In all studies, the resonant frequency is chosen to be $f_0 = 10.5$ GHz; the same as the design frequency for the final antenna. The effect of the aperture length is ignored, but for the necessary tuning to ensure that all apertures radiate at the same frequency. All antenna lengths are $\frac{\lambda}{2}k$, where $k \approx 1$ is tuned until resonance is obtained.

The property that is used to control the amplitude differs, depending on the type of aperture in question (hereafter referred to as the "amplitude tuner"). There are two classes, the offset aperture and the rotated apertures. The offset aperture is defined by the offset in the x -direction that the aper-

ture is placed from the centerline (the line along the z -axis) of the waveguide. Fig. 4.1 shows the axis and angle definitions required to interpret the amplitude tuners. The angle θ is used for rotated aperture antennas, where the offset is defined as the distance of the center of a slot in the x -direction.

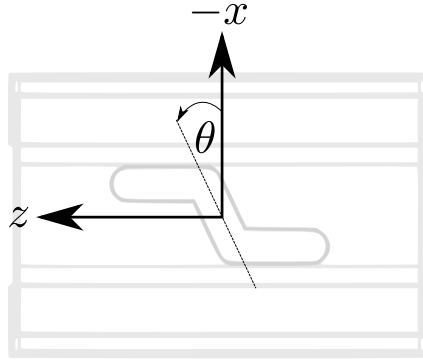


Figure 4.1: Definition of Amplitude Tuners

Since low *cross-polarization* is one of the final goals of the research, it is also a value that must be considered. For this application, vertical polarization is desired, so the cross-polarization is the horizontal polarization. Here the cross-polarization is treated as a ratio between the unwanted polarization and the desired polarization, as shown in Eq. 4.1.1.

$$\text{Cross-Polarization} = \frac{\text{Unwanted Polarization}}{\text{Desired Polarization}} \quad (4.1.1)$$

If these values are expressed in decibels (dB), which is a logarithmic scale, this ratio can be written as the difference between the two components as in Eq. 4.1.2.

$$\text{Cross-Polarization [dB]} = \text{Unwanted Polarization [dB]} - \text{Desired Polarization [dB]} \quad (4.1.2)$$

Bandwidth is also be considered. Bandwidth here refers the 3dB-Power bandwidth. In other words, the range of frequencies for which the aperture will radiate more than or equal to half of the maximum radiated power. This value is expressed as a percentage of the center frequency (f_0). To obtain the value, Eq. 4.1.3 is used.

$$BW\% = \frac{f_{MAX} - f_{MIN}}{f_0} \times 100 \quad (4.1.3)$$

Define P_{MAX} as the maximum radiated power, or the power at f_0 . The value f_{MAX} then refers to the first frequency f above f_0 for which $P_f = \frac{P_{MAX}}{2}$; f_{MIN}

refers to the first frequency below f_0 for which this is true. The results for these parameters are given and discussed in section 4.9.

4.2 Study: Offset Rectangular Aperture in the Broadwall

A rectangular aperture, cut into the broadwall of a rectangular waveguide and offset from the centerline, is shown by Fig. 4.2.

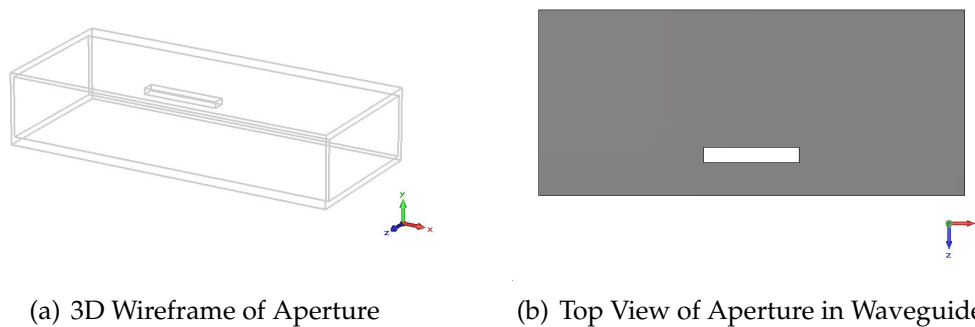


Figure 4.2: Model for Rectangular Aperture at Some Offset from the Center-line of the Waveguide

The waveguide used here is the standard WR90 rectangular waveguide used for many X-band applications. Its dimensions are $22.86 \times 10.16\text{mm}$ and is used here for all studies that require a rectangular waveguide profile.

By sweeping the value of the offset, the offset of the rectangular aperture, the power that is radiated can be increased. The length of the aperture is tuned for each of these offsets until the maximum power is radiated at the center frequency.

The *Amplitude Tuner* axis in the figures in section 4.9 refers, in this case, to the possible range of offsets for the aperture. The lower percentage value refers to the offset that corresponds to the lower radiated power and the higher percentage refers to the largest offset. For example, a value of 50% refers to the aperture being placed halfway between the centerline and the wall of the waveguide.

4.2.1 Bandwidth

Fig. 4.11 shows how the bandwidth changes with the amplitude. The values range from 10% – 14% for the offset rectangular aperture. These values are used as the benchmark against which the other studies are compared.

Rectangular apertures have been used for many years in a variety of applications, indicating that their performance characteristics are sufficient for practical applications.

4.2.2 Amplitude

The amplitude of the rectangular aperture is depicted in Fig. 4.12. It can be seen that a given aperture can radiate between 0% – 40% of the input power, depending on its offset. This behavior corresponds to the expected behavior of an offset aperture placed in the broadwall of a waveguide propagating the TE_{10} mode. As the offset increases, the aperture cuts more surface current, increasing the strength of the electric field that forms across the gap.

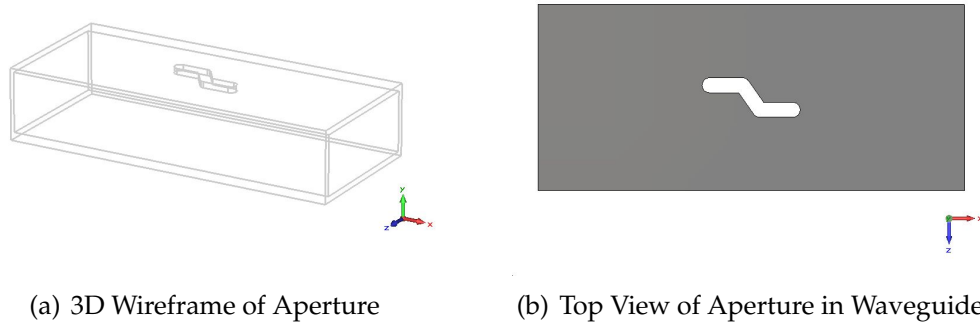
4.2.3 Cross-Polarization

This study is the only one for which the cross-polarization decreases with radiated power, as can be seen in Fig. 4.13. In other words, for high-power elements, the offset aperture will provide lower cross-polarization levels than the other configurations considered here. However, for lower values (less than 5% of the input power radiated by the aperture as is typical for large arrays), it may be better to use a different type of aperture.

4.3 Study: Z-slot Aperture in the Broadwall

Fig. 4.3 depicts a Z-slot cut into a standard rectangular waveguide. The Z-slot, named for its shape, is an aperture that is a combination of a rotated rectangular aperture and an offset aperture (see Fig. 2.10 for a depiction of these two configurations). The radiated power is altered by rotating the fixed length center section of the “Z”, while the two horizontal tabs are used for tuning the center frequency.

The *Amplitude Tuner* axis for the rotated slots refers to the rotation angle. The rotation θ may vary from $0^\circ - 90^\circ$, where $\theta = 90^\circ$ is the same as a rectangular aperture placed in the center of the waveguide. The rounded edges of the Z-slot is to model the aperture as it would be used in practice if machining techniques are used during manufacture. This is not done for the rectangular slots, as they are only for theoretical comparison and the literature generally does not take the rounding of corners into account. When reading the data in Fig. 4.11-4.13, note that $\theta = 90^\circ$ corresponds to the lower excitation limit of 0% and $\theta = 0^\circ$ corresponds to 100%.



(a) 3D Wireframe of Aperture

(b) Top View of Aperture in Waveguide

Figure 4.3: Model for Z-slot at Some Rotation Angle

4.3.1 Bandwidth

The performance of the Z-slot in terms of power bandwidth is depicted in Fig. 4.11. It can be seen that the bandwidth of the Z-slot is relatively stable when compared to the rectangular aperture and varies from 10% – 11.5%.

4.3.2 Amplitude

The Z-slot shows the same behavior as the rectangular aperture, but has a slightly lower radiation capability. Fig. 4.12 indicates that a Z-slot, when inserted in a rectangular waveguide, cannot radiate as much power as a rectangular aperture. However, the capability of the Z-slot to radiate energy is sufficient for applications where many radiators need to be utilized.

4.3.3 Cross-Polarization

According to the results displayed in Fig. 4.13, the Z-slot cross-polarization performance seems to be far below the standard of the rectangular aperture. This is because of the rotated nature of the slot. The surface current that is being cut generates an electric field across the aperture, just as in the rectangular aperture. However, the angle of rotation of the aperture causes the field to have an E_z and E_x component. The rectangular aperture did not experience this effect, which accounts for the pure polarization. If the E_z component can be suppressed, the polarization can be purified and performance improved.

4.4 Study: Z-slot Aperture in the Broadwall with Polarizer Plates

The previous section indicated that the rotated nature of the Z-slot causes an extra field component (E_z) to be generated, which is the field that contributes to the cross-polarization. In an effort to suppress this component, two plates are placed on either side of the aperture as depicted in Fig. 4.4.

Section 2.1.2 shows that two parallel plates of conducting material can be treated as a transmission line. The equations in Eq. 2.1.8 are valid if the parallel plates are fed with a field sufficient to excite the TE_1 mode. That is, an electric field tangential to the direction of propagation must be provided at a sufficient frequency. The field must also be oriented such that the field points from one plate to the other (the E_y component in Fig. 2.2). It is important to note that the other field components (e.g. E_x and E_z) are suppressed. This implies that if the plates are fed with a field that has two tangential components in the electric field, that only one will be propagated.

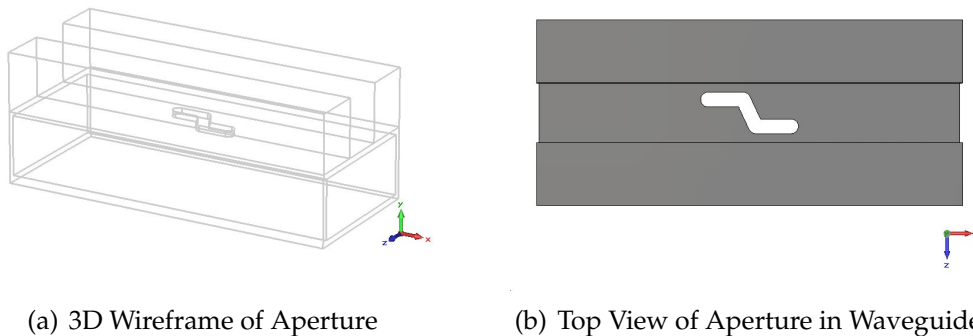


Figure 4.4: Model for Z-slot with 10mm Polarizer Plates

4.4.1 Bandwidth

Despite the anomalous behavior of the percentage bandwidth at lower excitations, it appears as though the trend for a Z-slot with polarizer plates is that the bandwidth decreases with excitation. The values vary between 9.5% – 12% bandwidth.

4.4.2 Amplitude

The polarizing plates seem to have little effect on the radiation capability of the Z-slot. At low excitations in particular, Fig. 4.12 shows that a Z-slot inserted into a rectangular waveguide radiates almost the same

amount of energy, despite the presence of the plates. Neither the Z-slot by itself, nor the Z-slot with the polarizer plates can achieve the same radiation capability as the rectangular aperture.

4.4.3 Cross-Polarization

For the polarizer plates to prove useful, the cross-polarization performance is critical. The addition of two 10 mm long plates suppress the cross-polarization level by as much as 20 dB. This improvement places the Z-slot performance in the same order as the rectangular aperture, particularly at lower excitations.

4.5 Study: Z-slot Aperture in a Ridged Waveguide

It has been shown that the Z-slot can provide performance comparable to that of a rectangular aperture antenna in terms of bandwidth, radiation capability and cross-polarization, provided that parallel plates are used to suppress the unwanted polarization. However, as discussed in chapter 3, it is sometimes desirable to use a waveguide with a different profile.

It is important to confirm that the performance of the apertures are not affected too greatly by the change in the waveguide. Fig. 4.5 depicts a Z-slot inserted into the waveguide that is used in the design of chapter 6.

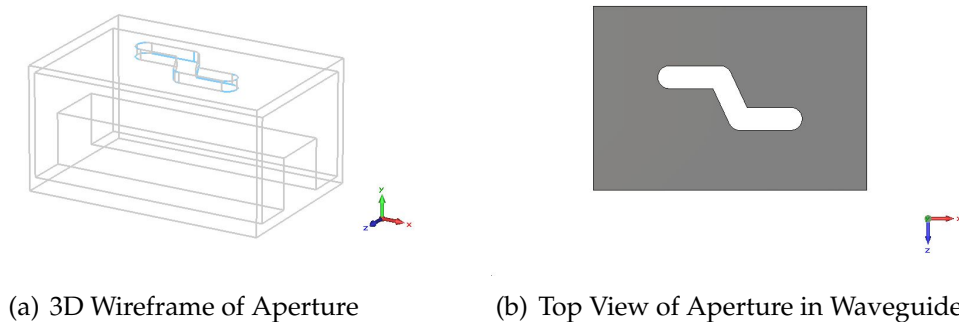


Figure 4.5: Model for Z-slot in a Ridged Waveguide

4.5.1 Bandwidth

The bandwidth of a Z-slot when inserted into the ridged waveguide of Fig. 4.5 is shown in Fig. 4.11. Of the studies conducted here, it provides the highest bandwidth for any given excitation.

4.5.2 Amplitude

The change in waveguide profile has changed the radiation capability of the Z-slot in such a way that the amplitudes are comparable to that of the rectangular aperture. A given Z-slot, inserted into a rectangular waveguide, radiates only about 70% of the power than if it is inserted in a ridged waveguide. This behavior can be ascribed to the higher field concentrations (i.e. the stronger surface currents) at the surface where the slot is inserted.

4.5.3 Cross-Polarization

Fig. 4.13 shows that the Z-slot in a ridged waveguide has almost identical properties to that of a Z-slot in a rectangular waveguide. However, there is an offset of 2–5 dB, indicating that the initial component of the undesired polarization is stronger when the aperture is excited in a ridged guide than if it is excited in a rectangular guide.

4.6 Study: Z-slot Aperture in a Ridged Waveguide with Polarizer Plates

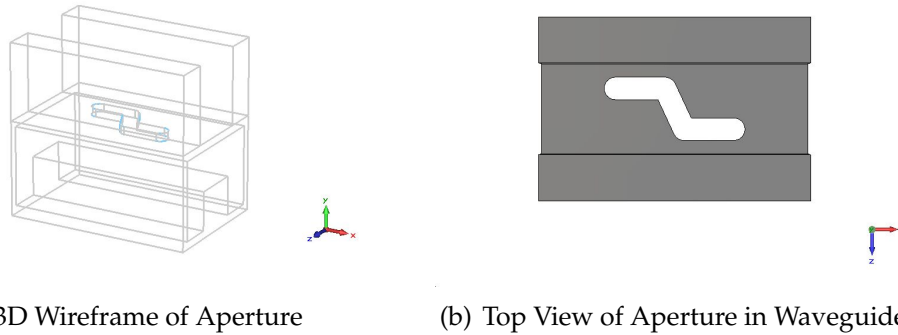
The aperture configuration that is used in the final design is depicted in Fig. 4.6. Fig. 4.6(a) shows how the ridged waveguide profile, polarizer plates and Z-slot are combined to provide a solution whose physical and performance properties adheres to the desired specification.

4.6.1 Bandwidth

The bandwidth of the Z-slot with polarizer plates in a ridged waveguide performs sufficiently well compared to other apertures and configurations. Depending on the excitation, the bandwidth varies between 11% – 12%, which is the most stable bandwidth of the configurations studied.

4.6.2 Amplitude

Fig. 4.12 shows that the excitation range is the highest of the configurations presented here, with a range of up to 42% of the input power radiated by a single element. It is unlikely that such values will be needed for an array,



(a) 3D Wireframe of Aperture

(b) Top View of Aperture in Waveguide

Figure 4.6: Model for Z-slot with 10mm Polarizer Plates in a Ridged Waveguide

but this range does indicate the sensitivity of the aperture to its rotation angle. Higher sensitivity implies that finer manufacturing tolerances are required, but also that a smaller range of tuning values are required. Since the Z-slot appears to have lower cross-polarization levels at lower tuning values, this could be advantageous.

4.6.3 Cross-Polarization

Again, the cross-polarization of the Z-slot in a ridged waveguide tracks the counterpart in a rectangular waveguide reasonably well, even with the polarizer plates present. Fig. 4.13 again depicts an offset of 2–5 dB as seen with the same configuration without the plates. If the range of apertures for the final design requires elements to radiate up to 15% of the input power, then the range of cross-polarization levels is the same as for the rectangular aperture, namely < -35 dB.

4.7 Study: Varying Polarizer Plate Lengths in a Z-slot Ridged Waveguide Configuration

In both the studies involving the Z-slot, the presence of a 10 mm length polarizer plate suppressed the cross-polarization of the configuration by 20–25 dB. The bandwidth and radiation capacity of the slots were reasonably unaffected, making polarizer plates a viable option for cross-polarization suppression.

This study varies the length of the polarizer plates surrounding a Z-slot antenna inserted in a ridged waveguide as in Fig. 4.6. A polarizer of zero length reduces to the model in Fig. 4.5. A slot angle of $\theta = 25^\circ$ is chosen and as the model is changed, the length is tuned to ensure resonance. The

length of the polarizer is swept between 1–15 mm and the cross-polarization level is studied.

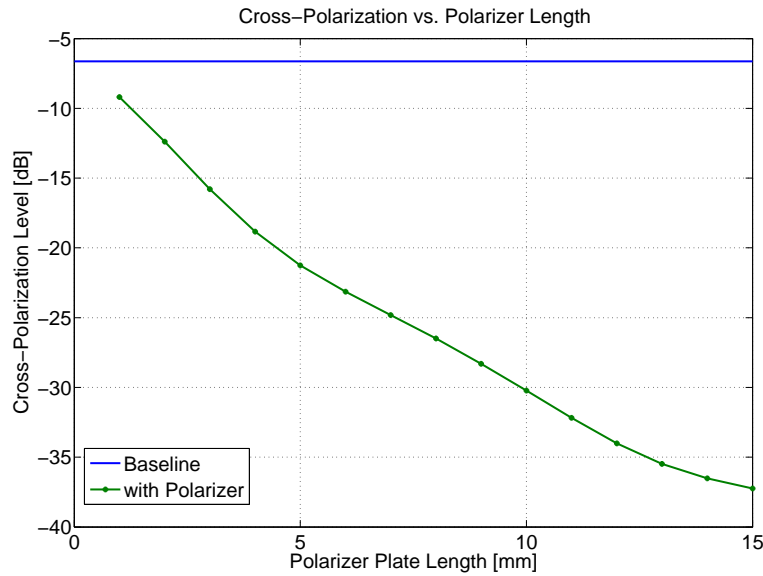


Figure 4.7: Cross-Polarization Level with Varying Polarizer Plate Lengths

Fig. 4.7 shows the cross-polarization of the configuration as the polarizer plate length is increased. The blue line at -6.63 dB shows the inherent cross-polarization of the configuration in the absence of polarizer plates. It can be seen that in general, a longer length of polarizer plate will provide more suppression of the unwanted polarization. The previous studies have shown that even though there is a strong link between the polarizer plates and the cross-polarization suppression, the bandwidth and radiated power is also affected.

Fig. 4.8 shows the bandwidth properties of the configuration when the lengths of the plates are varied. The blue line at 14.5% is again the baseline bandwidth in the absence of polarizer plates. The bandwidth can be pushed up to double the baseline value with the proper selection of plate length. Since bandwidth is related to the quality factor Q of the antenna, it may be useful to look at the variation of this property as well. The bandwidth is related to Q by Eq. 4.7.1 [5].

$$Q = \omega \frac{\text{average energy stored}}{\text{energy loss/second}} = \frac{100}{\text{BW}\%} \quad (4.7.1)$$

The stored energy can be stored as both magnetic (W_m) and electric (W_e) energy. Resonance, by definition, is that frequency where these two values are equal ($W = W_m = W_e$) [5]. The quality factor can then also be written as

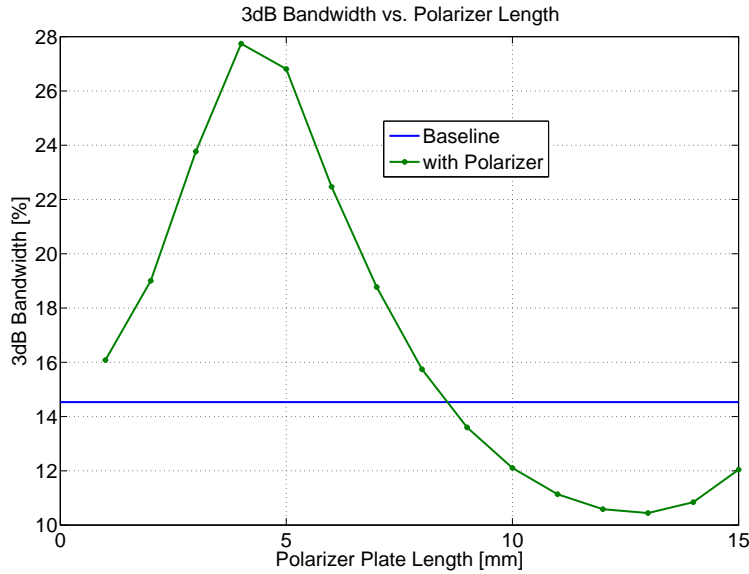


Figure 4.8: Bandwidth Variation as a Result of Varying Polarizer Plate Lengths

in Eq. 4.7.2a. Fig. 4.9 shows both the quality factor and the radiated power for comparison.

$$Q = 2\pi f_0 \frac{W_m + W_e}{P_R} = 2\pi f_0 \frac{2W}{P_R} \quad (4.7.2a)$$

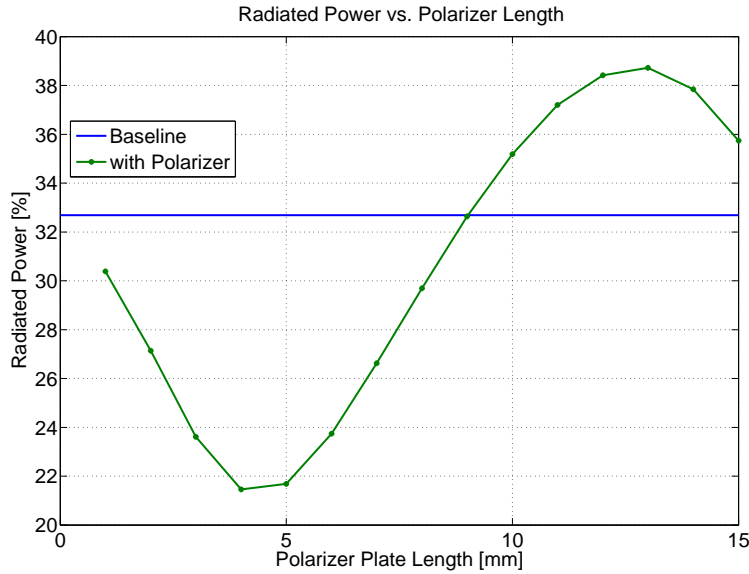
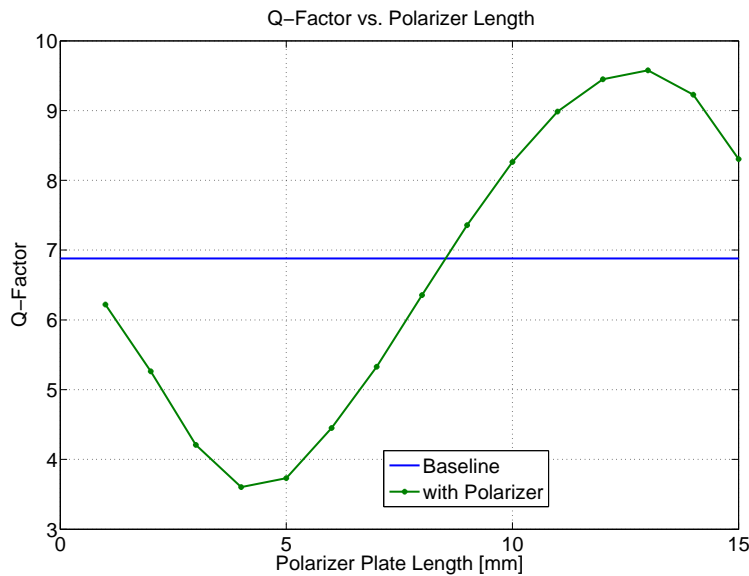
$$\Rightarrow W = \frac{QP_R}{4\pi f_0} \quad (4.7.2b)$$

From Eq. 4.7.2b it can be shown that if the radiated power as well as the quality factor decreases, that the stored energy must decrease as well. This means that even though it is possible to obtain a higher radiation capability from an aperture, it will also store more energy in the electric and magnetic fields of the configuration. It is suspected that mutual coupling between elements is related to the stored fields, making this an undesirable result. As a compromise, it is recommended that the polarizer length should be chosen based on two criteria:

1. the level of desired cross-polarization suppression; and
2. the length of polarizer plate that will leave other performance properties reasonably unaffected.

The properties of the configuration with a polarizer plate length of 10 mm that is used in other studies, can be compared to the baseline values as shown in Tab. 4.1.

Tab. 4.1 shows that with proper selection of the polarizer plate length, it is possible to obtain Z-slot elements that can radiate the same power over

(a) Percentage of Power Radiated at f_0 for Varying Polarizer Plate Lengths(b) Quality Factor at f_0 for Varying Polarizer Plate Lengths**Figure 4.9:** Radiated Power and Q-Factor for Varying Polarizer Plate Lengths

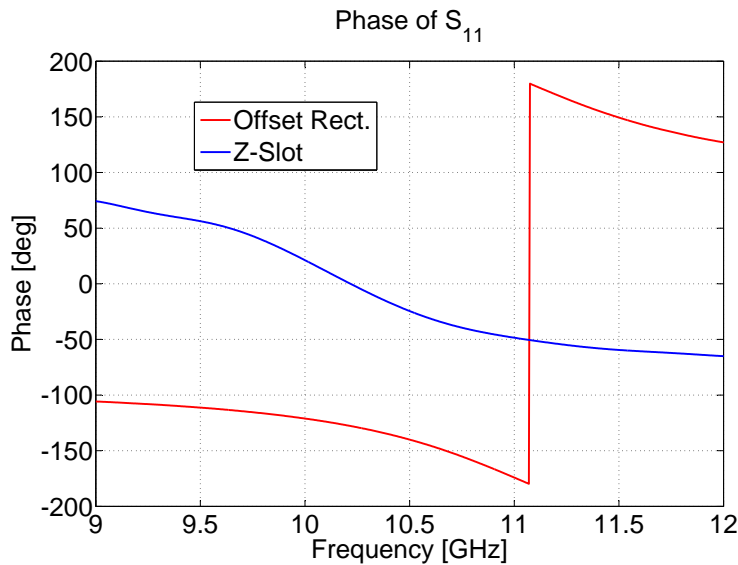
the same bandwidth as when the polarizer plates are absent. The reason for doing this is to achieve the cross-polarization suppression evident from Fig. 4.7. Tab. 4.1 shows a suppression of -23.6 dB in the cross-polarization for this element whilst leaving other properties relatively unaffected.

Table 4.1: Properties of a 25° Z-slot Antenna Compared to the Addition of Polarizer Plates

Property	Baseline	10 mm Plates
Cross-Polarization Level	-6.63 dB	-30.22
Radiation Capacity	32.69%	35.18%
3dB Bandwidth Percentage	14.53%	12.1%
Q-Factor	6.881	8.264

4.8 Equivalent Circuit Models

Section 2.2.2 stated that the equivalent model of an aperture may be approximated as either that of a series impedance or a parallel admittance. Fig. 4.10 shows the phase of S_{11} for both the offset rectangular aperture and the Z-slot aperture.

**Figure 4.10:** Phase of S_{11} for an Offset Aperture and a Z-slot

The difference in determining resonance stems from where the reflected voltage waves come from. The offset aperture responds similarly to that of a parallel impedance as depicted in Fig. 2.10(a). The Z-slot responds more like a series impedance as depicted in Fig. 2.10(b). However, the response of the Z-slot appears to be more complex. It may be necessary to use the more complete Π or T model networks to characterize the Z-slot. For the purposes of the work done here, the series impedance model is sufficient.

4.9 Simulation Results

The results of several studies discussed in this chapter are given here for convenience in Fig. 4.11 – 4.13. Each study discusses the data in Fig. 4.11 – 4.13 as it pertains to that study.

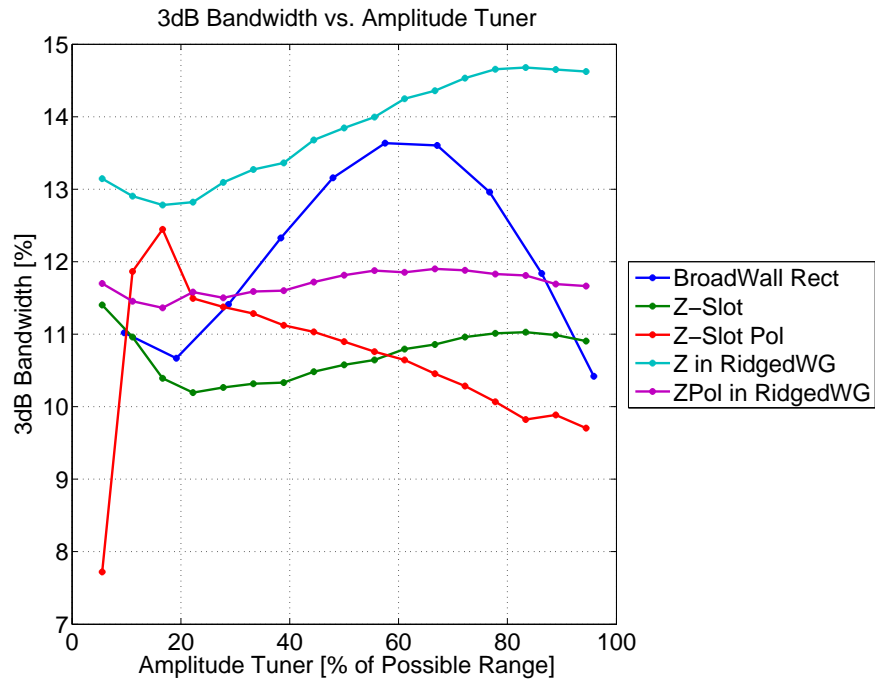


Figure 4.11: Percentage Bandwidth

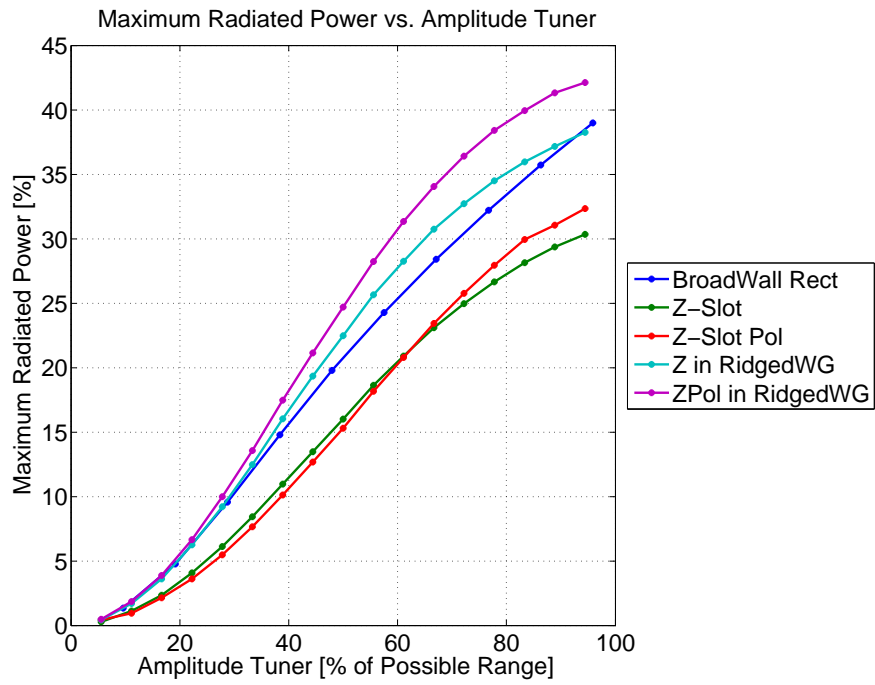


Figure 4.12: Percentage of Power Radiated by Aperture

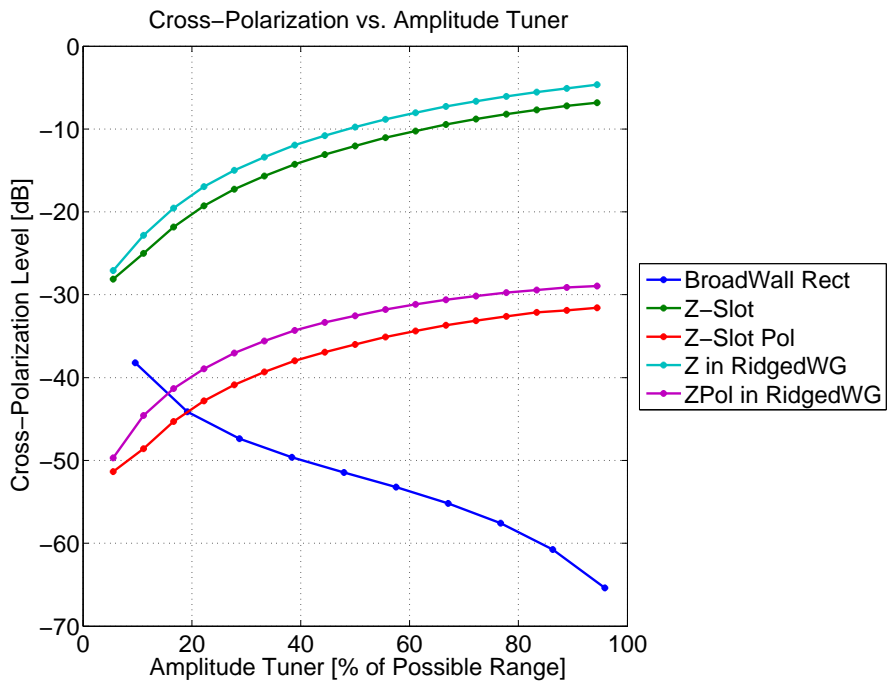


Figure 4.13: dB Cross-Polarization Level

Chapter 5

Algorithms for Aperture Characterization & Antenna Optimization

5.1 Discussion of the Parameter Sweep Algorithm

The flow chart for the algorithm of the parameter sweep is given in Fig. 5.1. Its structure is simple in that there are few branches and decisions that must be made. Before the algorithm can be executed, a CST model must be created with the aperture configuration that will be used in the array design. Three apertures are placed adjacent to one another to simulate a more realistic operating environment.

Fig. 5.2(a) shows the environment used to characterize a Z-slot. The center Z-slot's impedance is the one that is calculated from the scattering parameters. Matlab modifies the CST model to have the physical values required for an iteration of the loop shown in Fig. 5.1. The results are then pulled back into Matlab for further processing.

Once the entire range is simulated, a rough estimation of the behavior of the aperture is known. The resolution is then artificially enhanced by interpolating between the points. A high resolution will give a better first order estimate of any desired value. These higher resolution surfaces for the real, imaginary and bandwidth properties of the apertures are then stored for the optimization algorithm to implement an array design.

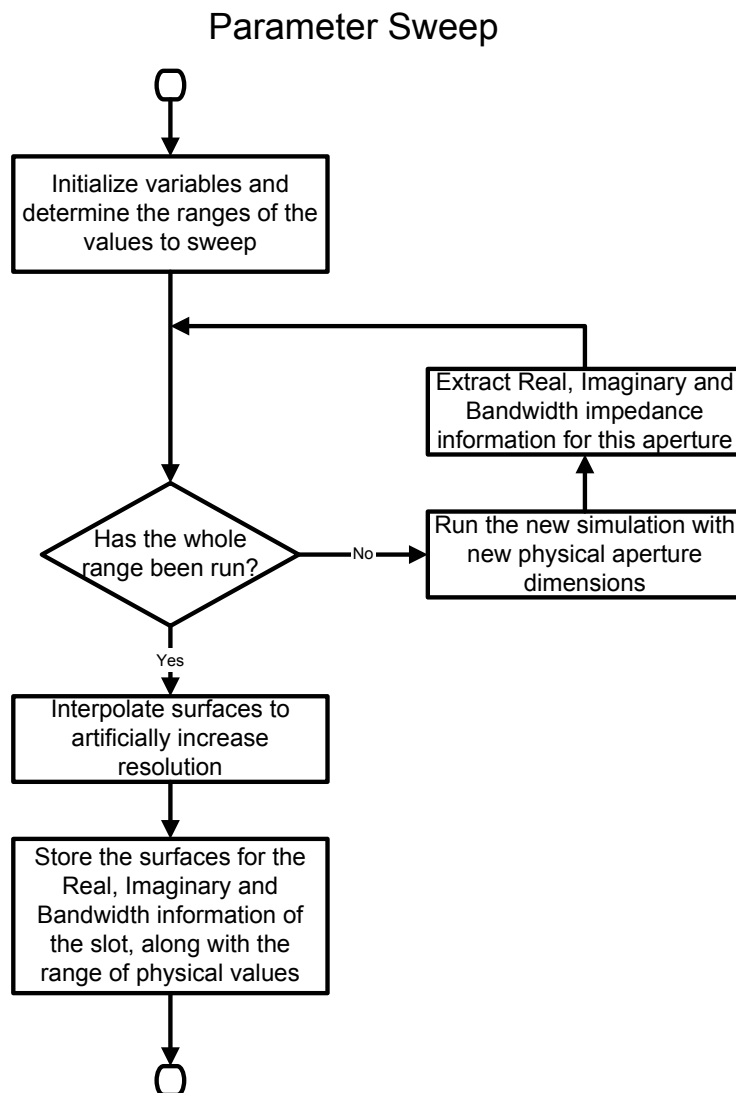


Figure 5.1: Flow Chart of the Parameter Sweep

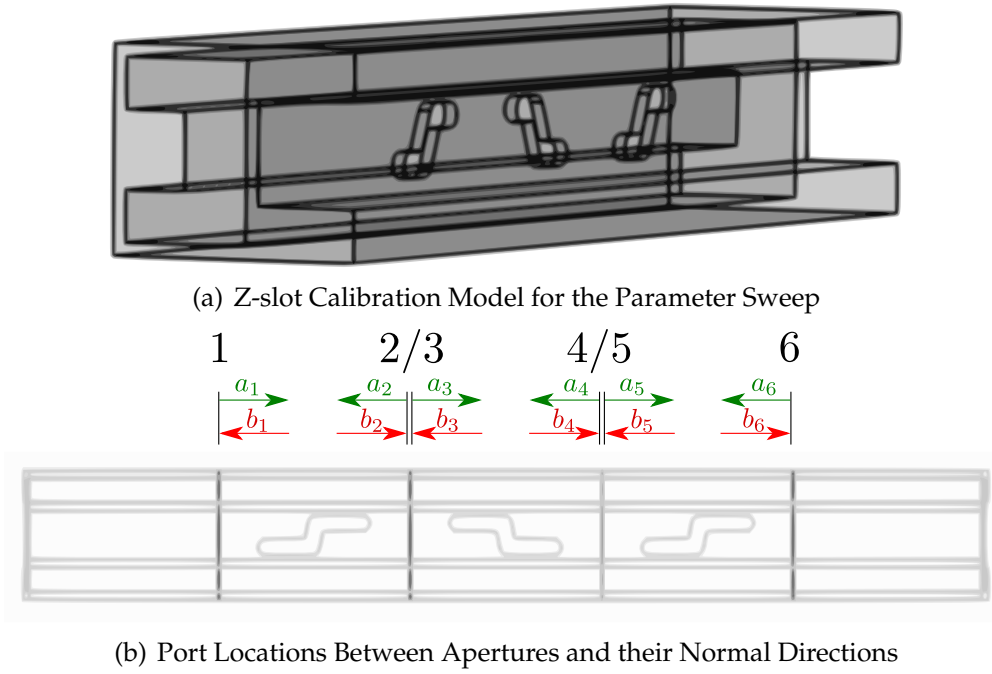


Figure 5.2: Z-slot Environment and Port Definitions

5.2 Extraction of Impedance Properties from S-Parameters

The extraction of the real, imaginary and bandwidth properties is non-trivial and requires further discussion. The S-parameter is defined as the ratio between the reflected voltage wave measured at a port “i” vs. the input voltage wave at port “j”. The notation for this ratio is given in Eq. 5.2.1.

$$S_{ij} = \frac{b_i}{a_j} \Big|_{V_k^+ = 0 \text{ for } k \neq j} \quad (5.2.1)$$

In Eq. 5.2.1, a_j is the incident voltage wave at port “j” and b_i is the reflected voltage wave (at port $i = j$) or the transmitted voltage wave (at port $i \neq j$) [5]. Note that the definition allows only one port to be active at a time. Using this convention, the scattering matrix for the model in Fig. 5.2(b) is written in Eq. 5.2.2.

$$\begin{bmatrix} b_1 \\ b_2 \\ b_3 \\ b_4 \\ b_5 \\ b_6 \end{bmatrix} = \begin{bmatrix} s_{11} & s_{12} & s_{13} & s_{14} & s_{15} & s_{16} \\ s_{21} & s_{22} & s_{23} & s_{24} & s_{25} & s_{26} \\ s_{31} & s_{32} & s_{33} & s_{34} & s_{35} & s_{36} \\ s_{41} & s_{42} & s_{43} & s_{44} & s_{45} & s_{46} \\ s_{51} & s_{52} & s_{53} & s_{54} & s_{55} & s_{56} \\ s_{61} & s_{62} & s_{63} & s_{64} & s_{65} & s_{66} \end{bmatrix} \begin{bmatrix} a_1 \\ a_2 \\ a_3 \\ a_4 \\ a_5 \\ a_6 \end{bmatrix} \quad (5.2.2a)$$

$$\mathbf{B} = \mathbf{SA} \quad (5.2.2b)$$

For a traveling wave antenna, energy is inserted into the waveguide at one end and propagates through the waveguide until it meets a terminating load. In other words, energy is coming from one end and is dissipated along the line. The load at the end absorbs the last of the energy from which nothing is reflected. When this principle is translated to the model in Fig. 5.2(b), energy is inserted into the guide at port 1. Port 2 absorbs all of the energy that is not radiated by the aperture. The energy that flows out of port 3 is exactly equal to the energy absorbed by port 2. In the same way the energy can be tracked up to port 6, where the last of the energy is absorbed. This can be written in vector form as in Eq. 5.2.3.

$$\mathbf{B} = \begin{bmatrix} b_1 \\ b_2 \\ b_3 \\ b_4 \\ b_5 \\ b_6 \end{bmatrix}; \quad \mathbf{A} = \begin{bmatrix} 1\angle 0^\circ \\ b_3 \\ b_2 \\ b_5 \\ b_4 \\ 0 \end{bmatrix} \quad (5.2.3)$$

In other words, the excitation vector can be written in terms of the incident and reflected waves. This means that, since \mathbf{S} is known from CST simulations, six independent equations can be written with four unknowns to solve (i.e. $b_2 \dots b_4$). When \mathbf{A} is substituted back into Eq. 5.2.2 and multiplied out, equations for each of the reflected voltage waves are obtained in the form of Eq. 5.2.4.

$$\begin{aligned} b_2 &= s_{21}1\angle 0^\circ + s_{22}b_3 + s_{23}b_2 + s_{24}b_5 + s_{25}b_4 \\ &\vdots \\ b_5 &= s_{51}1\angle 0^\circ + s_{52}b_3 + s_{53}b_2 + s_{54}b_5 + s_{55}b_4 \end{aligned} \quad (5.2.4)$$

Placing Eq. 5.2.4 back into vector form and further simplified to a new matrix form as in Eq. 5.2.5.

$$\begin{aligned}
 s_{21} &= [(1 - s_{23}) \quad -s_{22} \quad -s_{25} \quad -s_{24}] \mathbf{B} \\
 &\vdots \\
 s_{51} &= [-s_{53} \quad -s_{52} \quad -s_{55} \quad (1 - s_{54})] \mathbf{B}
 \end{aligned} \tag{5.2.5a}$$

$$\begin{bmatrix} s_{21} \\ s_{31} \\ s_{41} \\ s_{51} \end{bmatrix} = \begin{bmatrix} (1 - s_{23}) & -s_{22} & -s_{25} & -s_{24} \\ -s_{33} & (1 - s_{32}) & -s_{35} & -s_{34} \\ -s_{43} & -s_{42} & (1 - s_{45}) & -s_{44} \\ -s_{53} & -s_{52} & -s_{55} & (1 - s_{54}) \end{bmatrix} \begin{bmatrix} b_2 \\ b_3 \\ b_4 \\ b_5 \end{bmatrix} \tag{5.2.5b}$$

$$\mathbf{C} = \mathbf{Q}\mathbf{B}_{sub} \tag{5.2.5c}$$

The constants vector is represented by \mathbf{C} , \mathbf{Q} is a subset matrix of the S-parameters and \mathbf{B}_{sub} is a subset vector of \mathbf{B} . At closer inspection, it can be seen that \mathbf{Q} can also be written as in Eq. 5.2.5d.

$$\mathbf{Q} = \begin{bmatrix} 1 & 0 & 0 & 0 \\ 0 & 1 & 0 & 0 \\ 0 & 0 & 1 & 0 \\ 0 & 0 & 0 & 1 \end{bmatrix} - \begin{bmatrix} s_{23} & s_{22} & s_{25} & s_{24} \\ s_{33} & s_{32} & s_{35} & s_{34} \\ s_{43} & s_{42} & s_{45} & s_{44} \\ s_{53} & s_{52} & s_{55} & s_{54} \end{bmatrix} \tag{5.2.5d}$$

To solve for \mathbf{B}_{sub} , some manipulation can be performed to obtain the matrix solution given in Eq. 5.2.6.

$$\begin{aligned}
 \mathbf{C} &= \mathbf{Q}\mathbf{B}_{sub} \\
 \mathbf{Q}^{-1}\mathbf{C} &= \mathbf{Q}^{-1}\mathbf{Q}\mathbf{B}_{sub} \\
 \mathbf{B}_{sub} &= \mathbf{Q}^{-1}\mathbf{C}.
 \end{aligned} \tag{5.2.6}$$

The relationship between the reflected voltages and excitation voltages given in Eq. 5.2.3. Reflection coefficients can now be calculated at any port, since all of the excitation and reflected voltages are known. The reflection coefficient for port 3, for example, can now be written as in Eq. 5.2.7.

$$\Gamma_3 = \frac{b_3}{a_3} = \frac{b_3}{b_2} \tag{5.2.7}$$

Remember that there is a phase shift (call it $\Delta\phi$) associated with energy that propagates down a length of transmission line. Eq. 5.2.7 represents the reflection coefficient at the location of port 3. To move the reference point to the center of the slot, this phase shift must be taken into account for both the time it takes the incident wave to hit the aperture as well as the return

time. This is shown in Eq. 5.2.8.

$$\begin{aligned}\Gamma_A &= \frac{b_3 e^{-j\Delta\phi}}{b_2 e^{+j\Delta\phi}} \\ &= \frac{b_3}{b_2} \times e^{-2j\Delta\phi}\end{aligned}\quad (5.2.8a)$$

To convert from this reflection coefficient to the load impedance, Eq 5.2.9 is applied [5]. This now includes the impedance of the slot as well as the terminating load impedance (i.e. the input impedance behind the aperture). Note that $Z_0 = 1$ for the normalized system being used.

$$Z_{IN} = Z_0 \frac{1 + \Gamma_A}{1 - \Gamma_A} = \frac{1 + \Gamma_A}{1 - \Gamma_A} \quad (5.2.9)$$

Again, Z_{IN} refers to the input impedance that includes both the aperture and the input impedance after the aperture. Since only the impedance of the aperture is of interest, it is necessary to calculate the input impedance at port 5 in the same way. This time the transmission line phase shift must be calculated to the other direction as shown in Eq. 5.2.10.

$$\Gamma_5 = \frac{b_4}{b_5} \times e^{2j\Delta\phi} \quad (5.2.10)$$

Apply Eq. 5.2.9 to this reflection coefficient as in Eq. 5.2.11 and calculate the load impedance Z_L .

$$Z_L = \frac{1 + \Gamma_5}{1 - \Gamma_5} \quad (5.2.11)$$

The aperture impedance can be calculated by subtracting the two values, as they are placed in series (call it Z_S). If the element were to be a parallel impedance (call it Z_P), all of the calculations would be identical, except that the aperture would be taken as a parallel impedance to the load impedance. The calculation of the aperture impedance is given in Eq. 5.2.12, where the equivalent model of the aperture would determine whether Z_S (Fig. 5.3(a)) or Z_P (Fig. 5.3(b)) is used.

$$Z_S = Z_{IN} - Z_L \quad (5.2.12a)$$

$$Z_P = \frac{Z_{IN} Z_L}{Z_L - Z_{IN}} \quad (5.2.12b)$$

Any aperture that can be modeled as a series or parallel impedance can be calculated in this way. This method is used to gain an initial estimate of aperture impedance for all of the following designs.

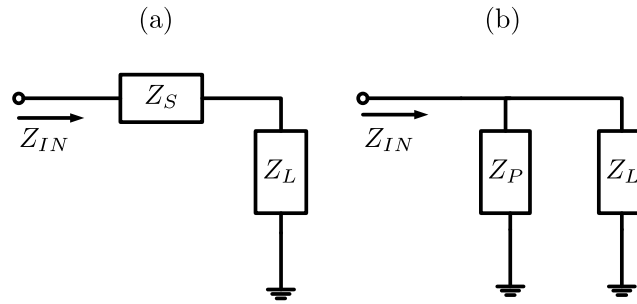


Figure 5.3: Location of Aperture Impedances With Respect to the Load Impedance

5.3 Simulation Results of a Parameter Sweep

The purpose of the parameter sweep is to characterize an aperture antenna in an environment similar to the one in which it will be implemented. That which is needed for this characterization includes information on the real part of the impedance, the imaginary part of the impedance and an indication of how quickly the values change. This information enables a reasonable first order estimate of the individual aperture properties of an array. This information is presented in the surfaces of Fig. 5.4–5.6.

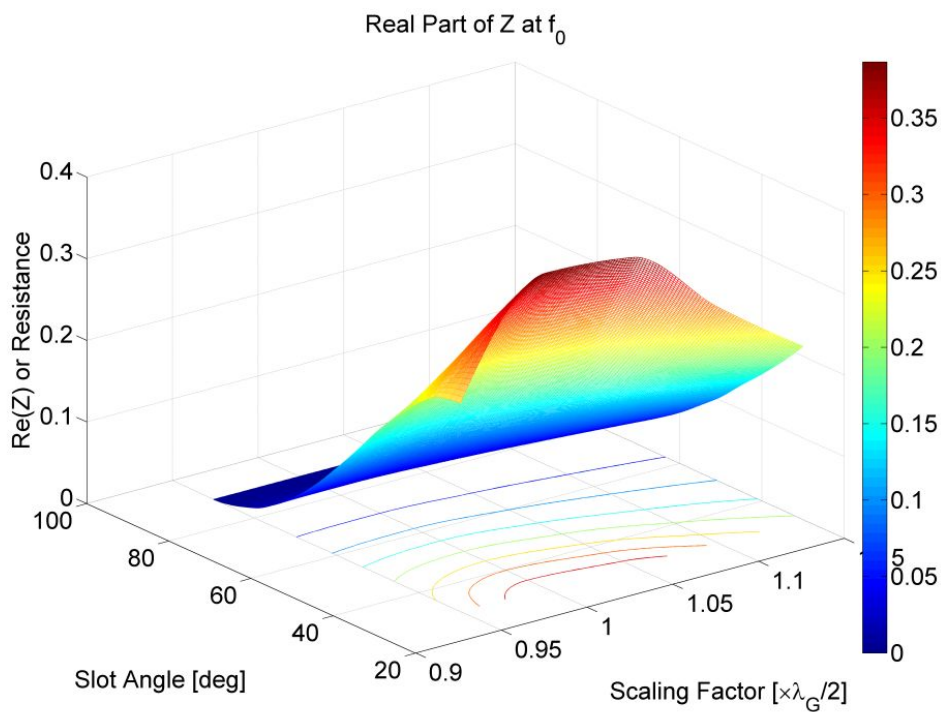


Figure 5.4: Resistance: Real Part of the Aperture Impedance

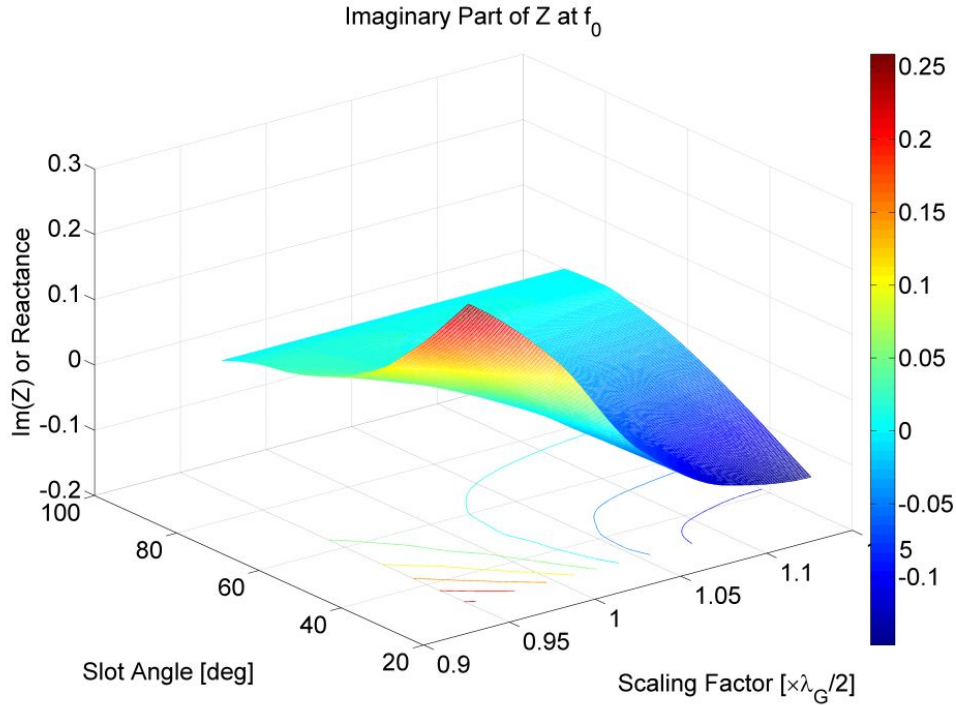


Figure 5.5: Reactance: Imaginary Part of the Aperture Impedance

The grids are obtained by calculating the impedance of a number of CST simulations with varying slot lengths and angles. Every frequency has its own impedance, so the values of Z at f_0 are isolated and plotted in Fig. 5.4–5.5 in its real and imaginary components. The values are then interpolated to artificially increase the resolution.

The phase slope is defined by locating the resonant frequency for any calculated impedance. This would be the frequency where the imaginary component is zero, or alternatively where the phase of the impedance is zero. If the change in phase is assumed to be linear in the region near the resonant frequency, a slope can be calculated that will indicate how quickly the aperture moves away from the resonant frequency. The slope is taken between -5° to 5° as depicted in Fig. 5.7.

Only the grids in Fig. 5.4–5.5 are used for the first-order design. Every point on the slot length and angle axes provides a data point for the real and imaginary components of the impedance. In other words, for any combination of physical parameters, there is an associated impedance. The impedances of interest are those for which the imaginary component is zero. When the curve from Fig. 5.5 that corresponds to $Im(Z) = 0$ is traced onto the surface of Fig. 5.4, a single curve in 3D space is obtained that gives the purely real aperture impedances.

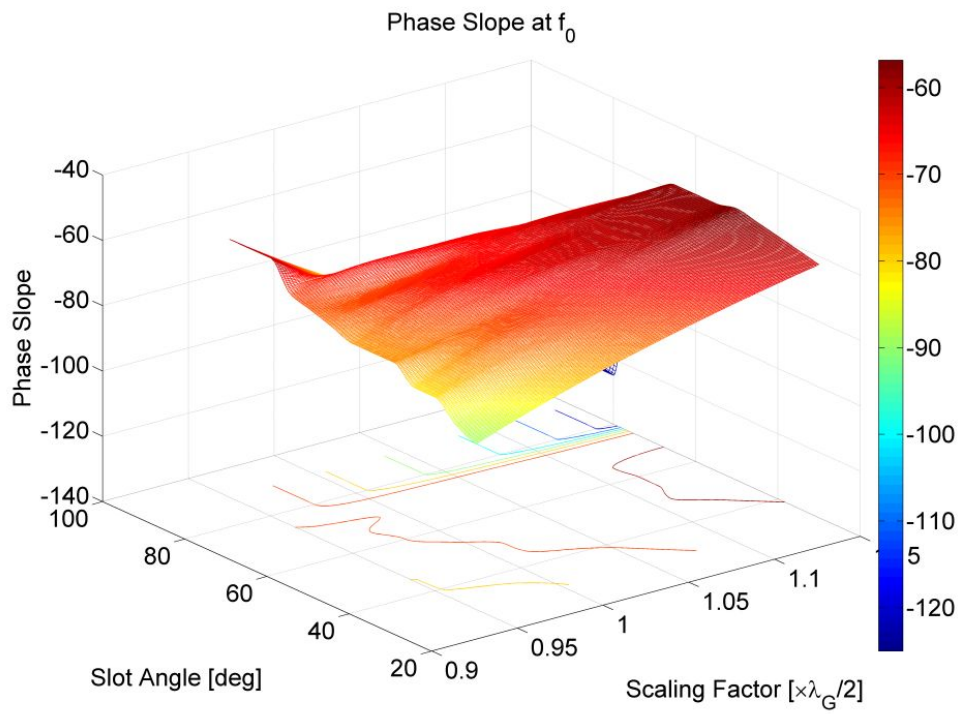


Figure 5.6: Phase Slope: Rate with which Impedance Changes

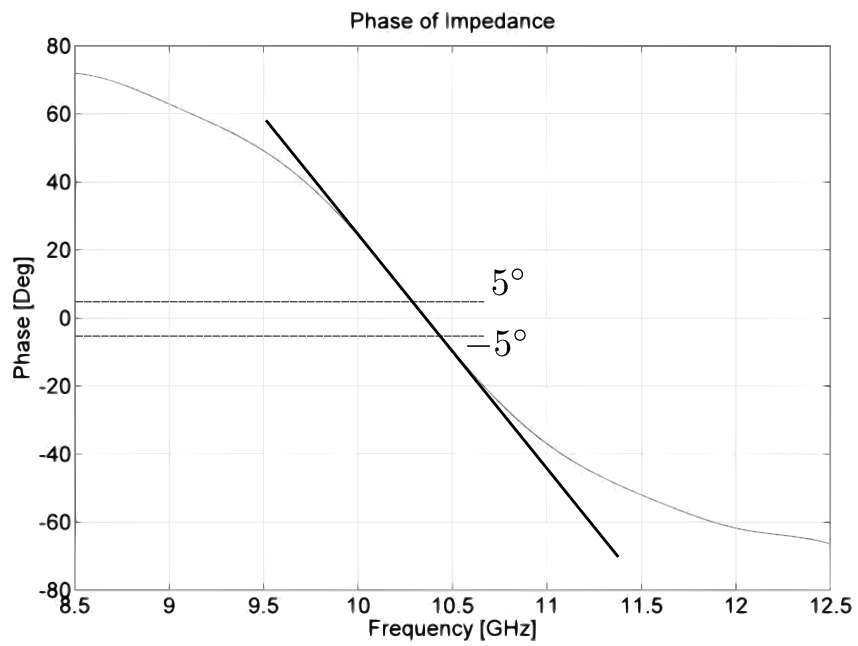


Figure 5.7: Phase of the Impedance

5.4 Optimization Algorithm

The term *optimization* is used here informally to describe the process of obtaining the best result for a design through the systematic application of a set of rules. The process is depicted in the flow chart in Fig. 5.8. The algorithm adjusts certain design parameters with each iteration with the aim of improving the performance characteristics of the antenna. The cycle terminates when the antenna shows the desired performance characteristics.

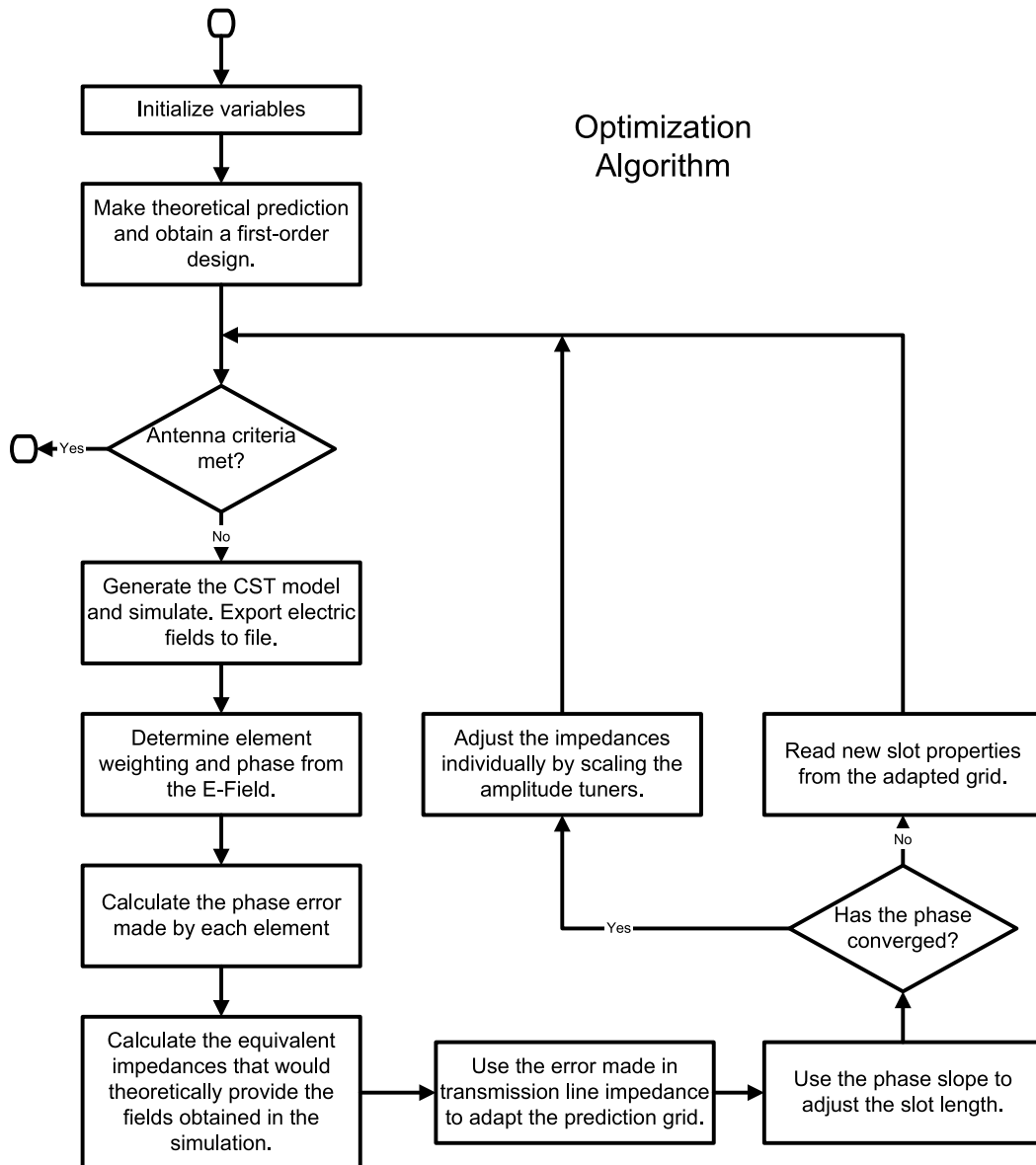


Figure 5.8: Flow Chart of the Optimization Algorithm

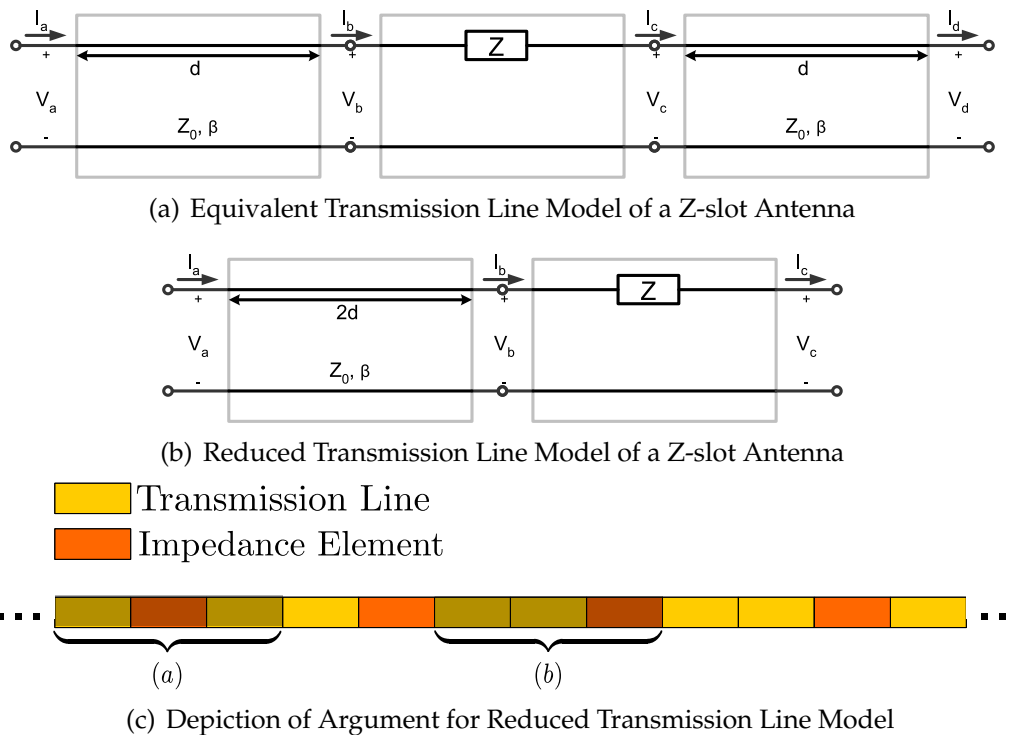


Figure 5.9: Transmission Line Model for a Z-slot Antenna

5.4.1 Theoretical Model

Before a model can be built and simulated, it is necessary to first design for the desired performance and create a first-order physical model of the antenna. Chapter 2, 4 and 5 interpreted aperture antennas as series or parallel impedances and were characterized in terms of impedance. Placing these impedances in a waveguide is similar to inserting a series or parallel impedance in a transmission line and can be cascaded with ABCD parameters as in Fig. 2.11.

Fig. 5.9(a) shows the equivalent model of a Z-slot antenna. Fig. 5.9(b) is a simplification of the same model. Note that the simplification assumes that the aperture antennas are cascaded. The two sections of transmission line are replaced by one of twice the length. This is *not* because one section is moved to the other side of the impedance, as this would cause a phase error. When two Z-slot models (Fig. 5.9(a)) are connected, there will be two sections of transmission line in the middle that connect. This is the source of the double length line in Fig. 5.9(b). In other words, between any two connected impedances, there will be two connecting sections of transmission line that can be seen as one line of twice the length. This argument is depicted in Fig. 5.9(c), where three Z-slot antennas are connected in series.

Using this model and the equations developed in section 2.3, the voltages and currents at any point on the line can be calculated; call them V_n

and I_n respectively. Since only the voltages and currents at the apertures are of interest, V_n and I_n will only be used to refer to the voltages and currents over the impedances, meaning that n is a number between 1 and the number of elements in the array.

The array synthesis requires a specific voltage or current weighting over a radiating element, depending on the equivalent circuit model of the aperture. The Villeneuve power distribution is shown in Fig. 5.10, along with the impedance distribution that will provide the power distribution.

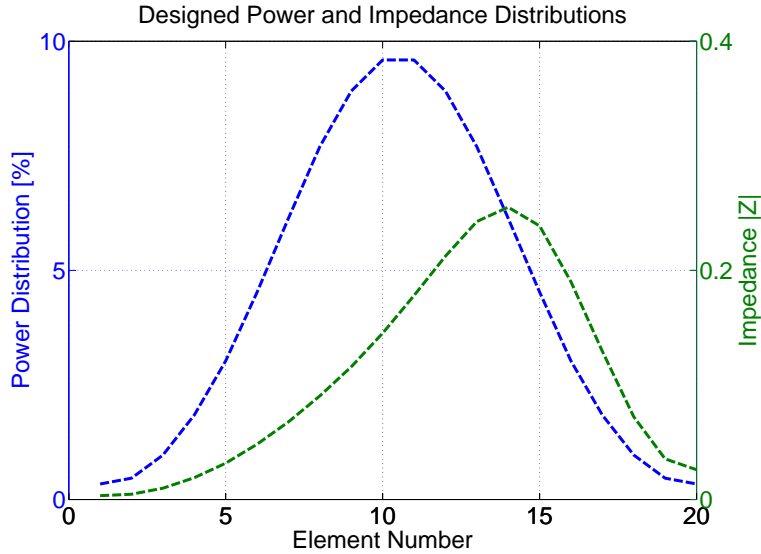


Figure 5.10: Villeneuve Power and Impedance Distribution

Each element in the array has a certain impedance associated with it. The mismatch caused by each cascaded element cause reflections back to the source. If all of these reflections add in phase, it disrupts the assumed one-way flow of power down the transmission line. To counter this effect in traveling-wave applications, the element spacing is altered such that the reflections add out of phase, thus diminishing the effect of reflections.

The transmission line model is again used to determine the total input reflection of the array. If the return loss, given by Eq. 5.4.1, is more than a designed threshold, the spacing is changed and the loss is calculated again. The smallest element spacing (i.e. the phase difference between the element excitation) that adheres to the desired return loss threshold is used.

$$RL = -20 \log |\Gamma| \quad (5.4.1)$$

Note that the only design criteria are the power distribution and the return loss. The impedances are calculated from the transmission line model

based on the desired power radiation of each element and the return loss determines the element spacing.

Once the impedances are known that will provide the necessary power distribution, the values can be looked up from the grids generated by the aperture characterization in chapter 5.

The physical parameters that are read from the grids, along with the calculated element spacing, is now used to generate a CST model. The model is simulated and the farfields and electric fields are stored. The electric field's amplitude and phase relate strongly to the excitation of an aperture. Regardless of the equivalent model of the aperture, the radiation occurs from an electric field forming over the gap of the aperture. By looking at the E-field some distance ($> \frac{\lambda_0}{2}$) from the aperture, the excitation of the aperture can be determined. The E-field represents either the voltage over a series element, or the current through a parallel impedance. An example of such a field is depicted in Fig. 5.11(a).

A windowing is performed where the average field over the region of each element is taken as the element weighting. The values are normalized, so the exact value is not important, only the pattern. For the phase shown in Fig. 5.11(b), only the value directly above the center of the element is taken. The distribution in Fig. 5.11(a) must be the square root of the power distribution (in order to obtain the excitation) given in Fig. 5.10 and the phase must change linearly due to the non-resonant element spacing.

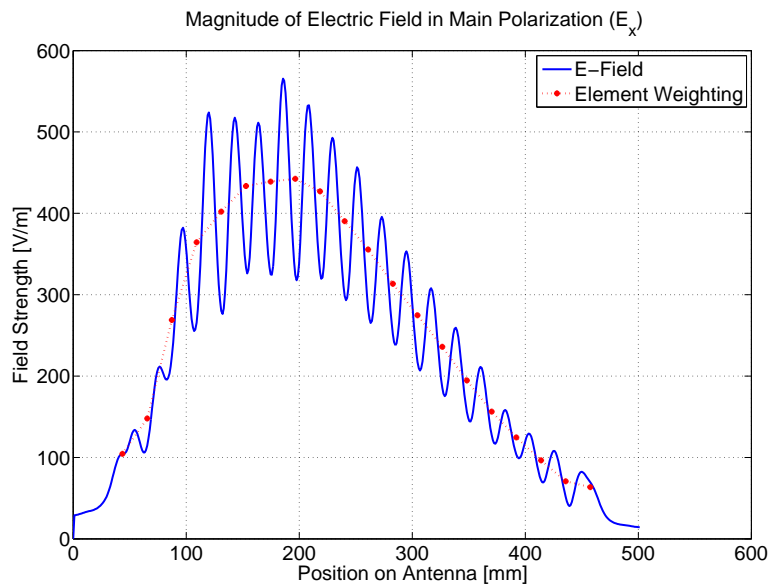
5.4.2 Interpretation of Simulation Results

The power that is not radiated by the antenna or reflected back to the source, must be the power absorbed by the load (P_L). This can be calculated as in Eq. 5.4.2a. Similarly, the total radiated power (P_R) must be the input power minus the power absorbed by the terminating load and the input port. Eq. 5.4.2b gives this equation in terms of S-parameters.

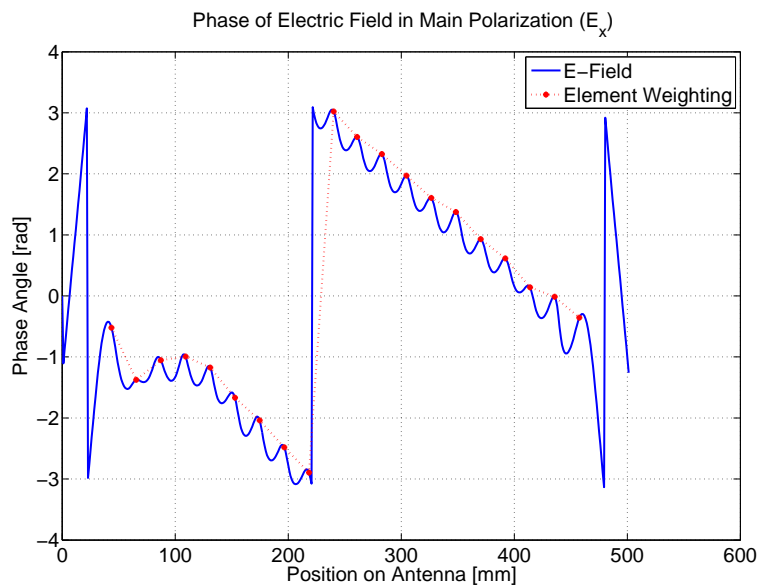
$$P_L = S_{21}^2 \quad (5.4.2a)$$

$$P_R = 1 - S_{11}^2 - S_{21}^2 \quad (5.4.2b)$$

The terminating load is used as the starting point for analyzing the rest of the array. The known radiated power P_L is used to determine the initial voltage and current of the system. Using the ABCD model of Fig. 5.9(b), the voltages (V_n) and currents (I_n) over each radiating element n can be calculated, including the effect of the transmission line between elements. The notation of Eq. 5.4.3 refers to the series impedance model depicted in Fig. 5.12.



(a) Magnitude of E_x of the Electric Field Over the Antenna



(b) Phase of E_x of the Electric Field Over the Antenna

Figure 5.11: Magnitude and Phase of Electric Field over the Antenna

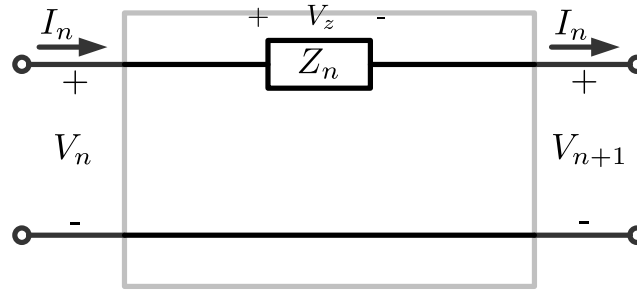


Figure 5.12: Series Impedance Transmission Line Model Notation

$$P_n = \left| \vec{E}_x \vec{E}_x^* \right| \quad (5.4.3a)$$

$$\text{Re} \{ Z_n \} = \frac{P_n}{\vec{I}_n \vec{I}_n^*} \quad (5.4.3b)$$

$$\phi = \angle Z_n = \angle E_x - \angle I_n \quad (5.4.3c)$$

$$Z_n = \text{Re} \{ Z \} + j (\text{Re} \{ Z_n \} \times \tan(\phi)) \quad (5.4.3d)$$

The power radiated by an element is related to the E-field excitation E_x by Eq. 5.4.3a. The radiated power is related to the real part of the element impedance and is given by Eq. 5.4.3b, where the angle of the impedance is equal to the angle of the field relative to the transmission line phase as in Eq. 5.4.3c. This stems from the transmission line model, where the excitation (which could be a voltage for parallel elements) could have any phase depending on the element spacing. If the element is purely real, the phase of the field should be identical to the phase on the line at that point.

With the real component and the phase angle of the impedance, the complete complex value of Z_n can be calculated with Eq. 5.4.3d. The element spacing at this point is known from the theoretical calculations, so the phase shift between elements can be calculated.

With all of this information, it is possible to obtain a transmission line model containing complex impedances that would provide the E-field excitation calculated by CST. This is the basis of the rest of the algorithm, as it indicates how far a desired aperture impedance is from the simulated aperture impedance.

5.4.3 Adaptation of Reference Values for Next Iteration

By adapting the prediction grid generated in chapter 5 after each iteration, it becomes increasingly accurate. The difference in simulated values for the aperture impedances to the predicted values can be attributed to the mutual coupling between elements. In essence, the prediction grid becomes

a specialized grid for a particular configuration which includes the effect of mutual coupling.

A curve is fit to the simulated data to approximate the simulated behavior of the range of impedances of interest. Fig. 5.13 shows the method used to fit the curve. Two curves are actually calculated. A 3rd order curve is fit to all the data points. Note that this curve can potentially have negative values for a real impedance (as can be seen in Fig. 5.13). To prevent these values from being incorporated, a 2nd order curve is also calculated, with the minimum amplitude being at $\theta = 90^\circ$ with an impedance of $\text{Re}\{Z\} = 0$. In other words, for higher impedance values, the 3rd order curve is used and the 2nd order curve is used at lower impedances.

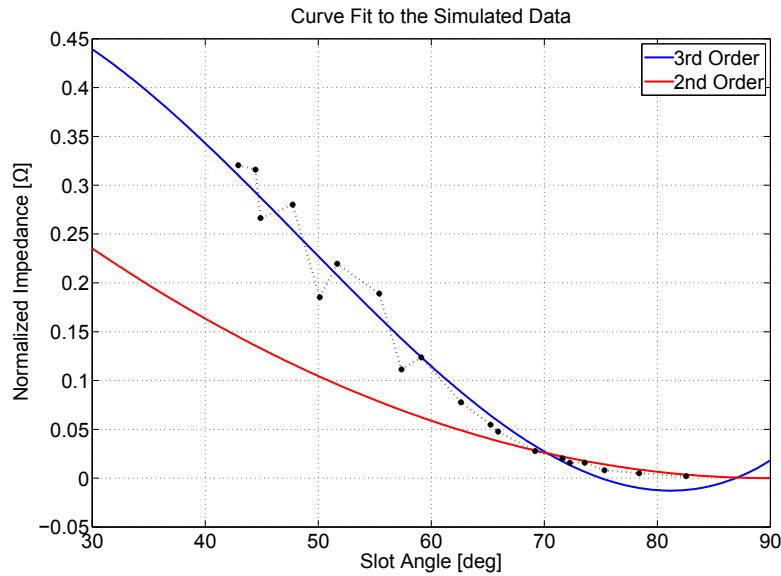
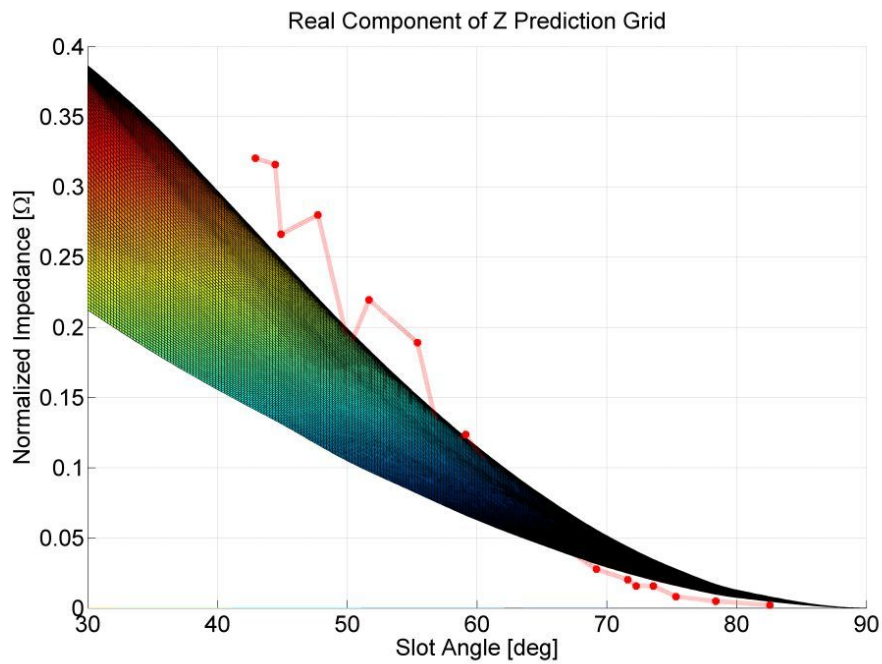


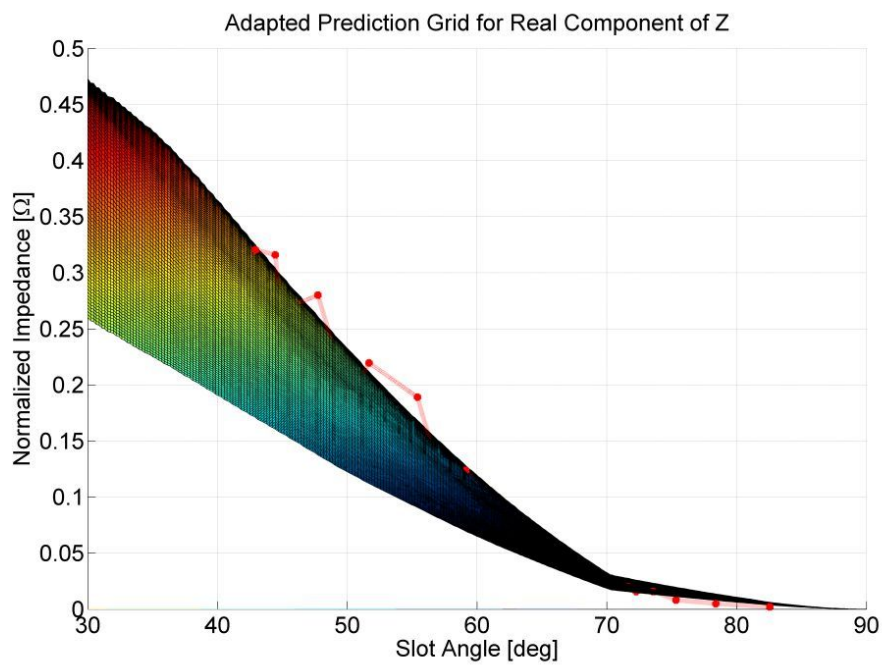
Figure 5.13: Curve Fitted to Simulated Data

The curve in Fig. 5.13 is used to scale the prediction grid. For any aperture length in the grid of Fig. 5.4, the impedance is scaled so that the simulation results match the physical parameters used. The initial prediction grid and the adapted grid are shown in Fig. 5.14(a) and Fig. 5.14(b), respectively. The reasoning is that, had the same physical values been used for the simulation, the predicted impedances would be much closer to the estimated values.

Note that only the real part of the impedance has been discussed thus far. The imaginary component also plays a very important role in the adaptation process, albeit more subtle. The presence of the imaginary component implies that the element is not operating at resonance. This could best be explained using an example. Take the curve of Fig. 5.7. It has the properties of a phase slope $m = -66.6$ and a resonant frequency $f_0 = 10.375$ GHz.



(a) Original Prediction Grid



(b) Adapted Prediction Grid

Figure 5.14: Prediction Grids Before and After Adaptation

Hypothetically, if an impedance angle of $\angle Z = 20^\circ$ is measured after a simulation, then the following procedure may be applied to rectify the error.

The positive angle $\angle Z = 20^\circ$ implies that there is in fact a different resonant frequency (f_s) for this configuration than the predicted value of f_0 . Assuming that the error is in the region close to where the phase changes linearly, a straight-line approximation can be made to determine the actual resonant frequency f_s . These steps are shown in Eq. 5.4.4.

$$ph(f) = mf + c \quad (5.4.4a)$$

$$c = 20 - (-66.6)(10.375) = 711.6 \quad (5.4.4b)$$

$$\therefore ph(f) = -66.6f + 711.6 \quad (5.4.4c)$$

and resonance occurs when ph is zero,

$$\Rightarrow 0 = -66.6f_s + 711.6 \quad (5.4.4d)$$

$$f_s = 10.675 \text{ GHz} \quad (5.4.4e)$$

The linear approximation is applied and the simple relation for the new aperture length (l_{new}) can be written as in Eq. 5.4.5.

$$l_{new} = l_{old} \times \frac{f_{actual}}{f_{expected}} = l_{old} \times \frac{f_s}{f_0} \quad (5.4.5)$$

This adaptation is made to each individual aperture length. In the example above, the new length would be $l_{new} = l_{old} \times \frac{f_s}{f_0} = 1.0289 \times l_{old}$. It may take several iterations before the values are reasonably accurate (within 5% or less, depending on the accuracy required by the application). This is because both the magnitude *and* the phase of the aperture impedance are modified simultaneously. The magnitudes will initially be inaccurate because of the phase error, but as the phase error diminishes, the simulated magnitudes will become closer to the values predicted by the adapted grids.

Once the magnitudes and the phases of the elements have stabilized (in other words the predicted physical values cease to change between iterations), it is possible that the desired power distribution still has not been obtained. This is because the grids were adapted using a 3rd order and 2nd order approximation. The actual magnitude behavior of the apertures are unknown, particularly in the presence of mutual coupling. When it is clear that this primary convergence point has been reached, the adaptation strategy must be altered.

The second phase of the magnitude tuning involves a new approach that assumes the values are close to the final values. This means that some convergence will take place, albeit on an arbitrary curve. To remedy this, the second phase only looks at the element excitation weighting. If an element's

weighting is too low, it is pushed up and if it is too high, it is lowered. This method ignores the impact that the tuning has on the impedance models of the apertures, which will have an effect on the element phase and load power. For this reason it is used only for fine-tuning and for no more than three or four iterations. During this phase, phase tuning is implemented in the same way as during the first phase.

The combination of the different tuning methods helps the algorithm to aim for a design that has the desired element excitation. This implies that the equivalent transmission line model is satisfied, except with the results of the second magnitude tuning phase.

5.5 Validation of CST Models

Before the algorithm is applied to the design of the Z-slot array, it is necessary to confirm that:

1. The simulation results generated by the algorithm environment accurately depict the real-world properties of an antenna; and that
2. The properties being measured accurately characterize the behavior of the antenna.

The first point refers in particular to the radiation pattern of the antenna. It is important to know whether the CST simulations provide results that compare well to actual antenna measurements. The second point refers to whether the assumptions and approximations made during the design process are reasonable. Both of these points can be resolved by comparing a measured farfield to the simulated farfields from CST.

The antenna that is used to verify the algorithm is described by the properties in Tab. 5.1. Offset rectangular apertures (or longitudinal slots) inserted in the broad wall of the waveguide are used.

Table 5.1: Properties of the Antenna Used for Validation

Property	Value
Profile	WR90
f_0	9.9 GHz
Number of Elements	40
P_L	3%
Sidelobe Level (Design)	-35 dB
Sidelobe Level (Real)	-30 dB
Taper	Villeneuve
Feed Type	Traveling Wave

The design properties of the antenna are not evaluated here, as the design is not generated by any work done in this thesis. It serves only to validate the environment. To that end, an antenna is taken for which measured data is available. The antenna is recreated in CST with the code used by the optimization algorithm. The same fields that are used for the algorithm are exported and interpreted as would normally be done for an iteration.

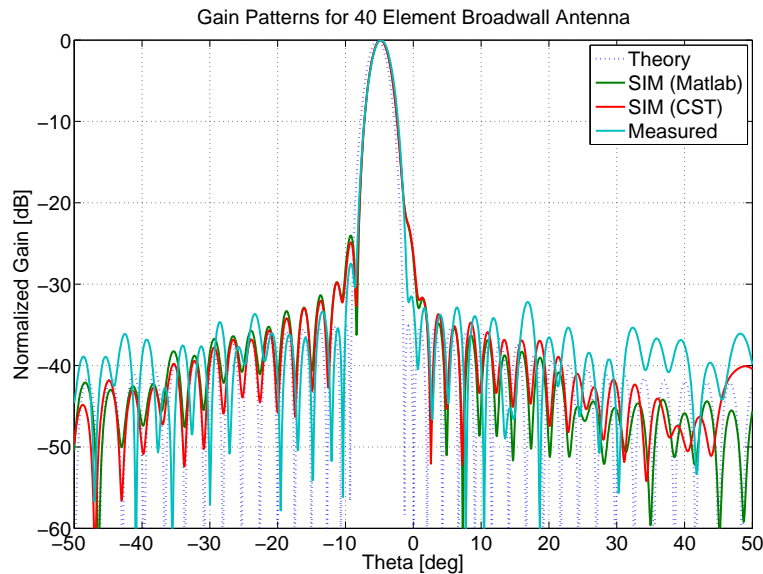


Figure 5.15: Gain Patterns for 40 Element Offset Rectangular Aperture Array

Four plots are visible. The first is the theoretical prediction of what the radiation pattern would look like if all elements are ideal. The second uses the optimization algorithm's method of determining the gain pattern, which only looks at the main polarization's electric field component. CST also generates a radiation pattern, which is shown by the third curve. Finally the measured data is provided. Fig. 5.15 indicates that the simulations predicted the general behavior of the antenna reasonably well (to within a few dB of the measured values). Discrepancies can be attributed to simulation or measurement inaccuracies. Note the squint of -5° ; this is due to the non-resonant spacing that is typical of traveling wave antennas.

Fig. 5.16 gives a close-up view of the main lobe and the close-in side lobes. The simulation data agrees very well, with the behavior of the two patterns being similar except for a 1 dB error on the peak of some lobes. The simulations show that there is a shoulder expected at $\theta = -1^\circ$ and a high sidelobe at $\theta = -9^\circ$. The measured data behaves as predicted, the shoulder at $\theta = -1^\circ$ manifests as a small sidelobe and the high sidelobe at $\theta = -9^\circ$ is present, although also lower than predicted. Other differences between the

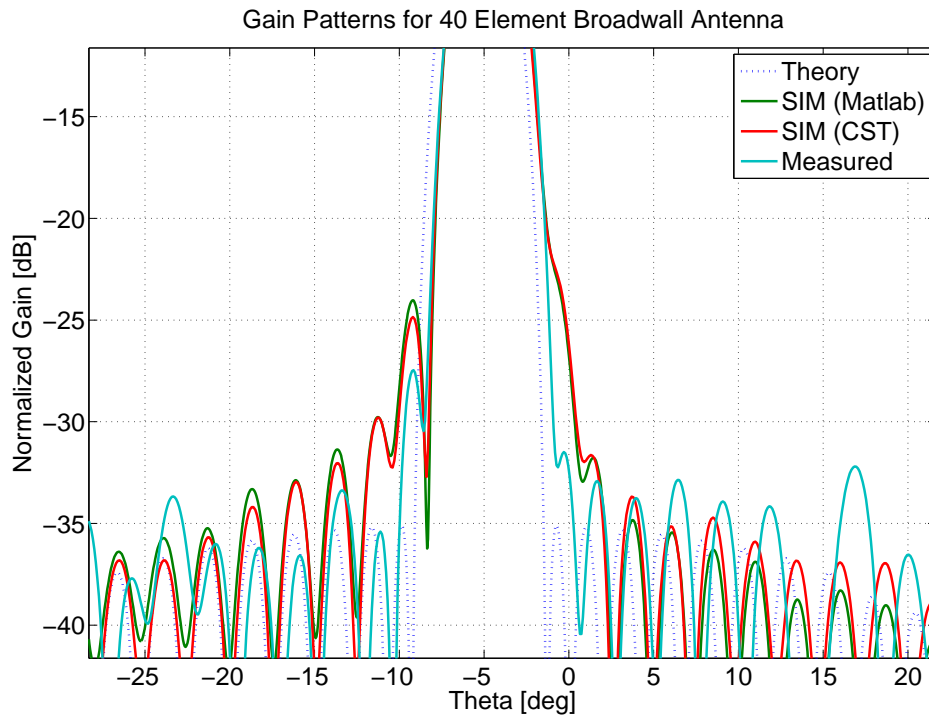


Figure 5.16: Zoom of Gain Patterns for 40 Element Offset Rectangular Aperture Array

measured and simulated data can be attributed to manufacturing tolerances of the antenna or inaccuracies in the measurement setup.

The calculated gain pattern appears to provide a reasonable estimate for antenna performance. Also, the method used by the optimization algorithm to calculate the gain pattern is comparable to CST's calculation, which implies that the correct parameters are being monitored.

Chapter 6

Antenna Designs and Comparison

The results obtained from the optimization algorithm of chapter 5 and the work that precedes it are summarized here in the form of three antenna designs. The first antenna is a benchmark antenna that consists of rectangular offset apertures inserted into a rectangular waveguide. The other two antennas both make use of the Z-slot. The first is a simple Z-slot array in a rectangular waveguide, where the other includes the ridged waveguide design of chapter 3 and polarizer plates. The attributes of the antennas are compared in order to isolate the source of undesired sidelobes.

6.1 Benchmark Design

The benchmark design is intended to give a baseline for the performance of an antenna with the design specifications given in Tab. 6.1. It makes use of offset rectangular apertures inserted into the broad wall of a standard rectangular waveguide (WR90). Since the Z-slot antenna is intended to replace an antenna of this type, it is important to know how well it performs. A secondary purpose is to ensure that the optimization algorithm performs as desired and converges to the correct result.

Table 6.1: Specifications for the Benchmark Design

Property	Value
Operating Frequency f_0	10.5 GHz
Number of Elements	20
Sidelobe Level (Design)	-35 dB
Sidelobe Level (Real)	-30 dB
Taper	Villeneuve

The specification in Tab. 6.1 specifies several operating properties of the antenna. The ones that were chosen include the use of a Villeneuve distribu-

tion, that the antenna must be a traveling-wave type and have a load power of $P_L = 13\%$. The load power may seem arbitrary, but is chosen to ensure that the aperture impedances fall within the possible range. In effect, if the load power is too low, then the aperture impedances must be higher in order to radiate the additional energy. Note that even though a sidelobe level of -35 dB is specified, any value below -30 dB is sufficient. The tolerance of 5 dB is common for many antenna designs.

A model of the waveguide is given in Fig. 6.1(a) as the starting point. Once the physical properties of the elements are determined, the waveguide in Fig. 6.1(a) is manipulated and the apertures are inserted to produce an antenna as in Fig. 6.1(b).

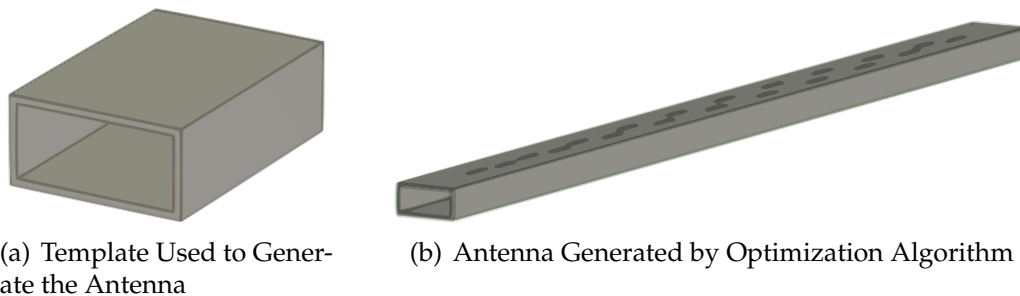


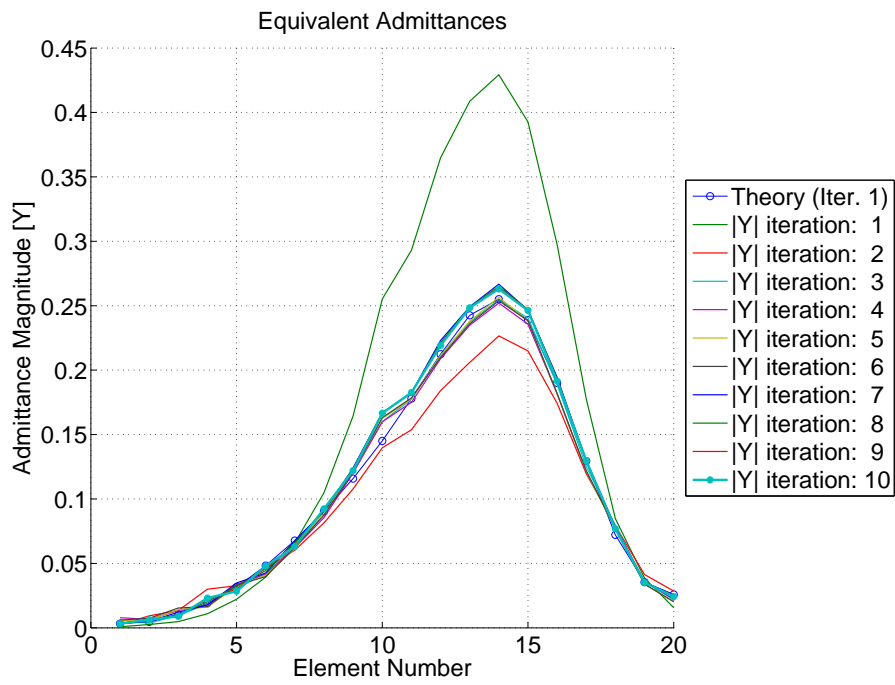
Figure 6.1: CST Model of the Benchmark Template and Antenna

The desired performance is obtained after 10 iterations for this antenna. As was stated in section 5.4, the iterations are tuned based on the magnitude and phase error made with the aperture impedances. Fig. 6.2 shows the magnitudes calculated with each iteration and for clarity, only the final values are shown in Fig. 6.2(b).

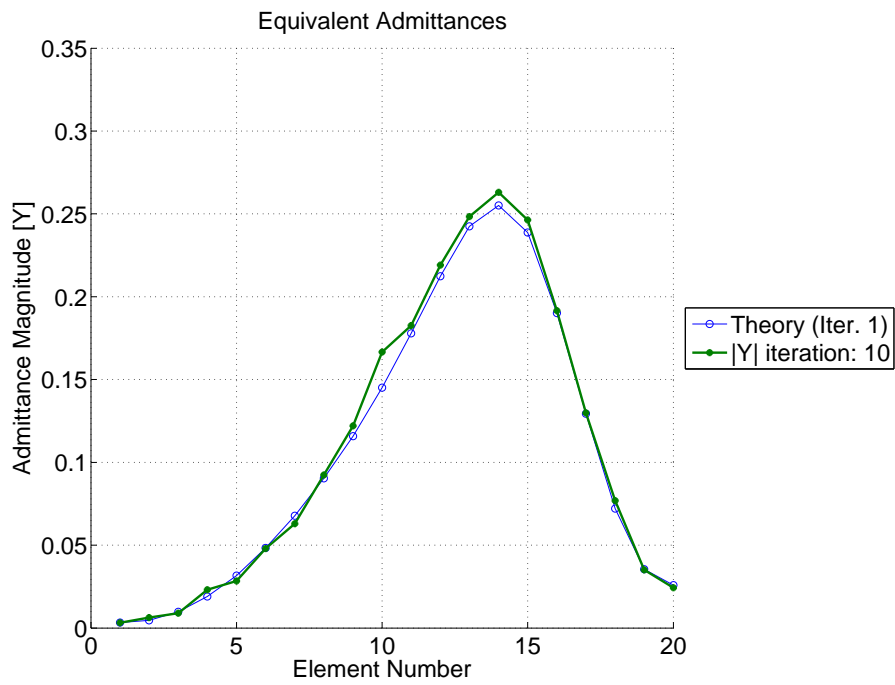
It can be seen that the magnitude for the first iteration, which was based on the values generated by the characterization in chapter 5, is off by almost double the desired value for some elements. However, after only two iterations the magnitude converged to a reasonably accurate state (less than 5% average error). Similarly, the phase in Fig. 6.3 shows how the phase is affected after each run.

The phase error for the first iteration is the curve that spans between -20° and 20° . The phase error is very sensitive at lower values and it takes three iterations before the phase begins to settle. After the 10th iteration, the phase is shown by Fig. 6.3(b). The average phase error for the final iteration is 0.73° , which may be considered to be a high level of accuracy.

Once the magnitude and phase has converged to the acceptable levels shown in Fig. 6.2(b) and Fig. 6.3(b), the performance of the antenna must be analyzed. The radiation pattern is used for this purpose. Fig. 6.4 shows the gain for the final iteration. The theoretically calculated pattern is also shown.

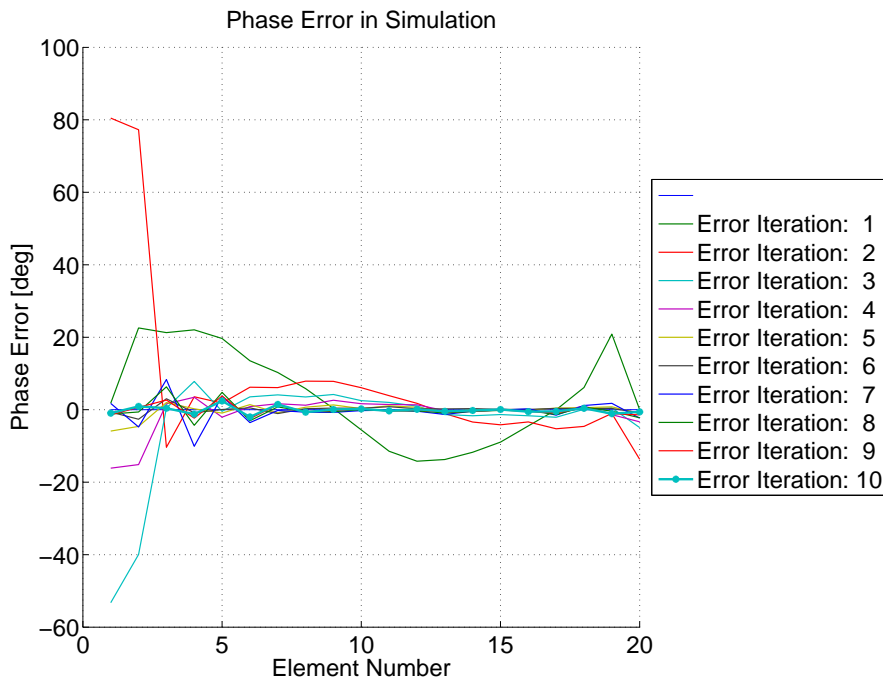


(a) Simulated Magnitudes Over All Iterations

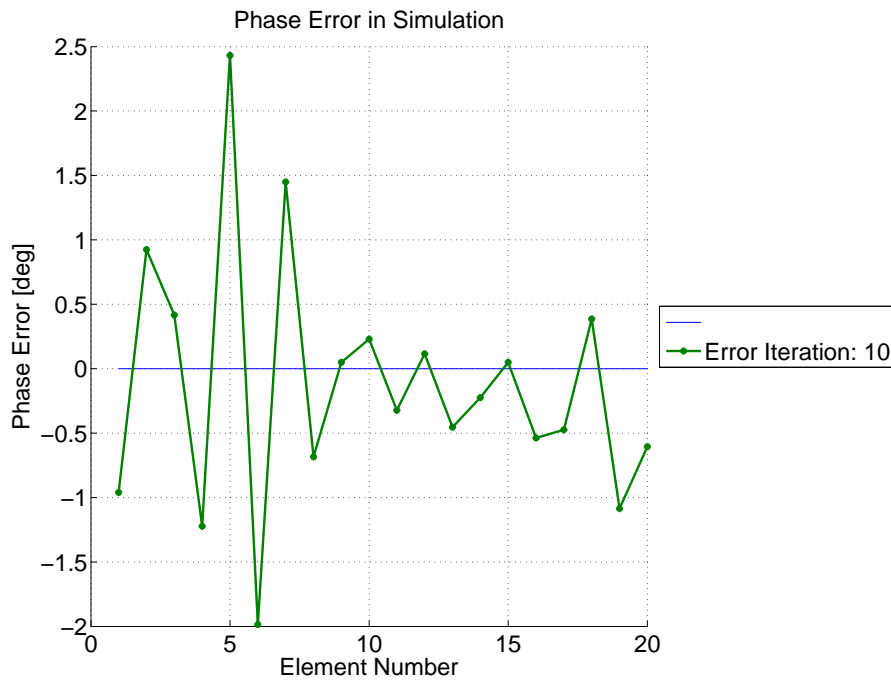


(b) Simulated Magnitude for Final Iteration

Figure 6.2: Simulated Magnitudes for All Iterations of the Benchmark Antenna



(a) Simulated Phases Over All Iterations



(b) Simulated Phase for Final Iteration

Figure 6.3: Simulated Phases for All Iterations of the Benchmark Antenna

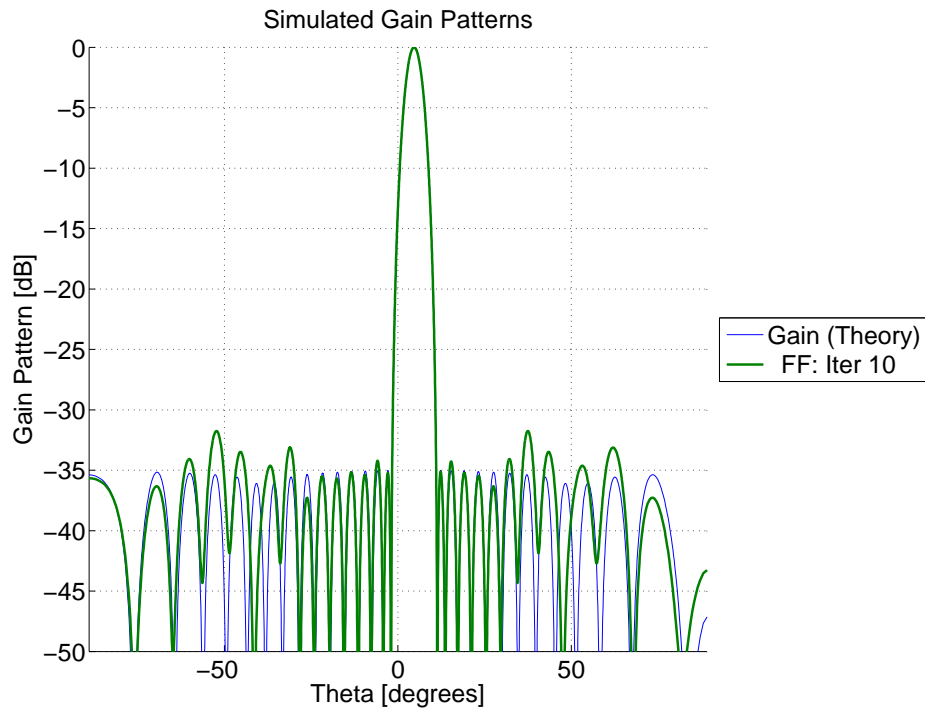


Figure 6.4: Radiation Pattern for the Benchmark Design

It can be seen that the simulated pattern matches the theoretical pattern to within 3 dB over the band and that a sidelobe level of -32 dB is obtained. This result is satisfactory; it implies that the optimization algorithm is functioning correctly and provides a benchmark antenna with which to compare the performance of the Z-slot antenna designs.

6.2 WR75 Z-slot Antenna Design

For the Z-slot antenna to be compared to the benchmark, it must have similar design properties. Therefore the specifications given in Tab. 6.1 are applicable to the design of the Z-slot antenna array as well, along with the additional design characteristics chosen (i.e. $P_L = 13\%$, the antenna should be a traveling-wave type and the same Villeneuve power distribution is used). The desired radiation pattern is obtained after 13 iterations.

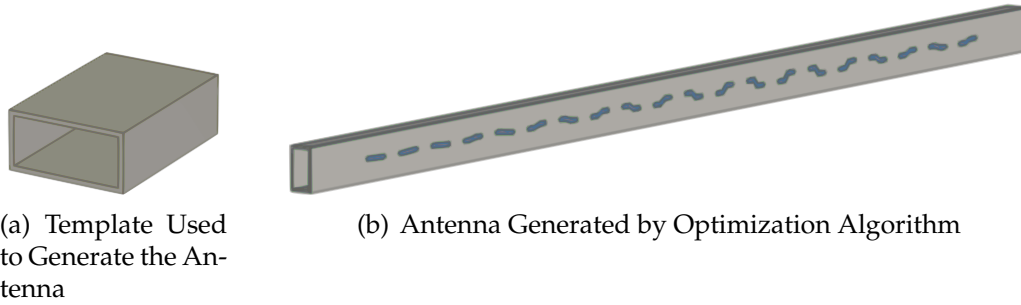


Figure 6.5: CST Model of the WR75 Z-slot Template and Antenna

A slightly different approach is used for the second phase of the optimization algorithm than for the other two antennas, where the transmission line power is used as a reference rather than just the power distribution. This results in the load power being taken into account as well as the power distribution, providing more accurate results (as opposed to the method used in section 6.3).

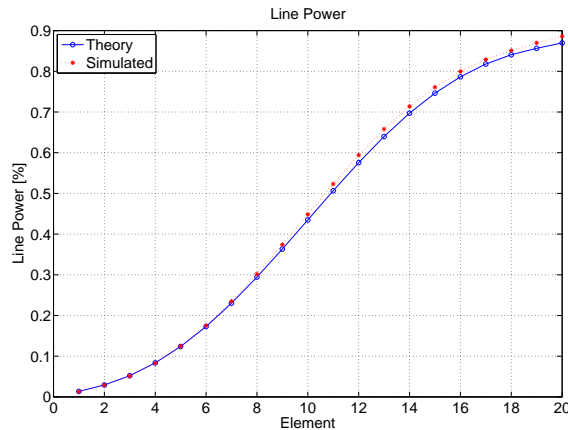


Figure 6.6: Total Radiated Power After Each Element

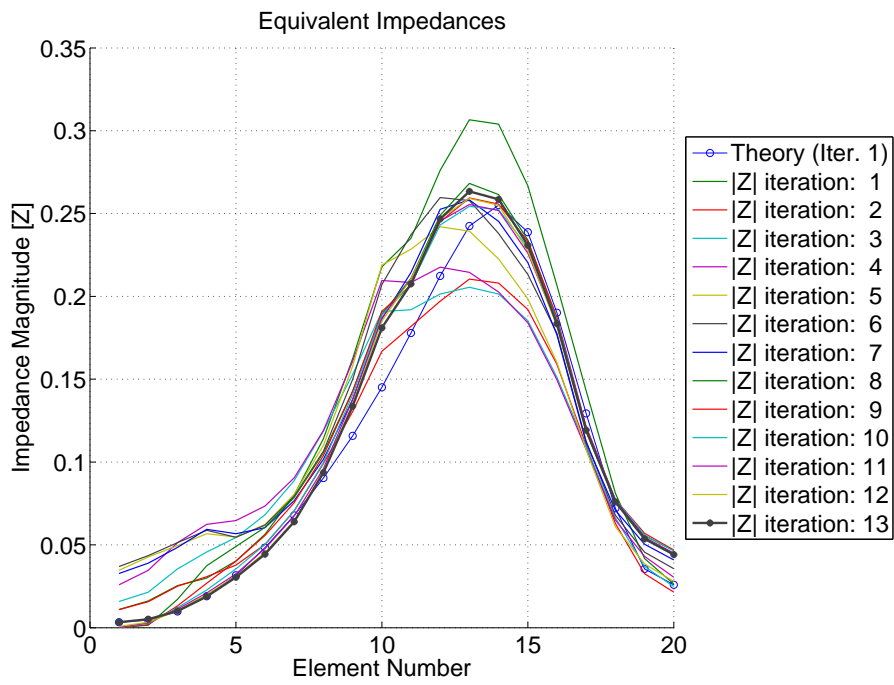
The transmission line power that remains after each element is theoretically known. Fig. 6.6 shows the total radiated power ($P_{IN} - P_{Line}$) for

the final iteration. A power balance can more easily be seen for traveling-wave antennas using this method than when only the element distribution is taken into account. The load power is $P_L = 11.4\%$ of the input power.

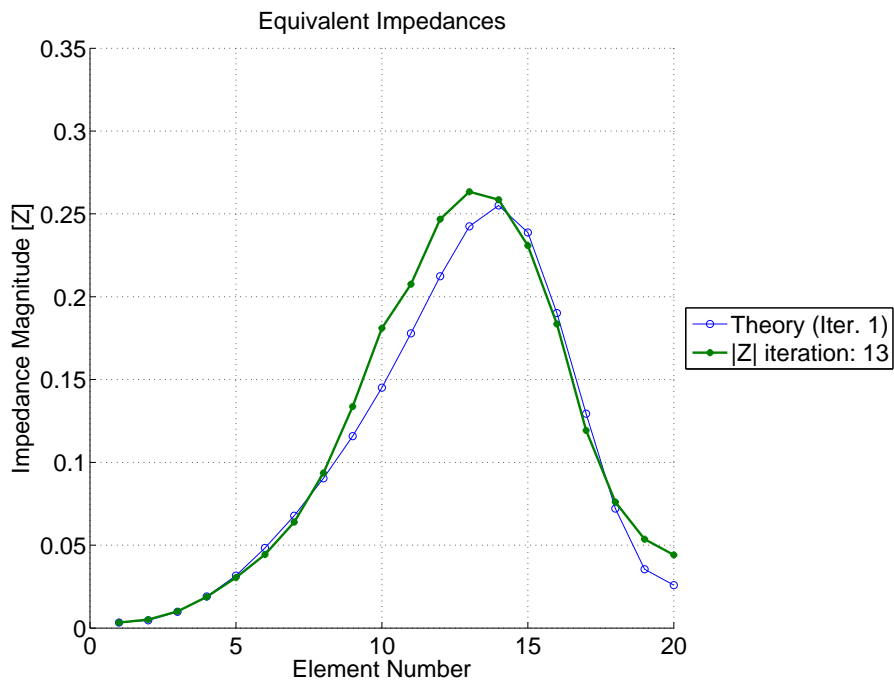
Fig. 6.7 shows the magnitude of the element impedances over all iterations and for the final iteration. For low values the approximations and grid adaptations appear to have difficulty describing the actual behavior of the Z-slot apertures; this can be seen from the large range of values and the lack of convergence for lower values. The second phase tuning takes care of this discrepancy and provides adequate results.

The element phases are shown in Fig. 6.8. Both the impedance magnitude and phase results indicate that a reasonable level of accuracy is obtained. The average phase is accurate to within 3° and the magnitude to within 5% of the desired values.

The radiation pattern shown in Fig. 6.9 is within specifications. The pattern is calculated using only the main polarization component. The effect of the cross-polarization component on the radiation pattern is discussed in section 6.4.

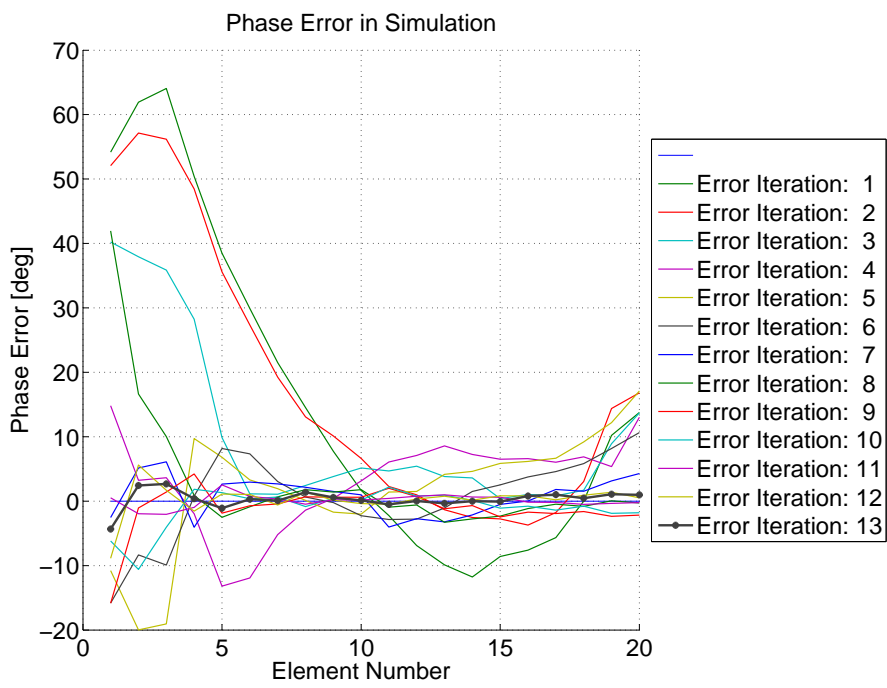


(a) Simulated Magnitudes Over All Iterations

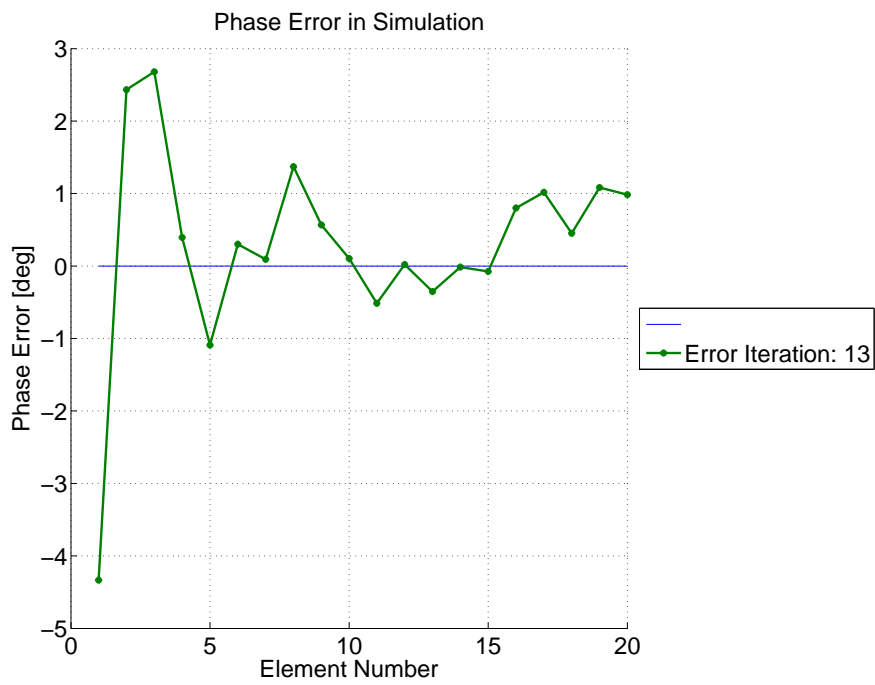


(b) Simulated Magnitude for Final Iteration

Figure 6.7: Simulated Magnitudes for All Iterations of the WR75 Z-slot Antenna



(a) Simulated Phases Over All Iterations



(b) Simulated Phase for Final Iteration

Figure 6.8: Simulated Phases for All Iterations of the WR75 Z-slot Antenna

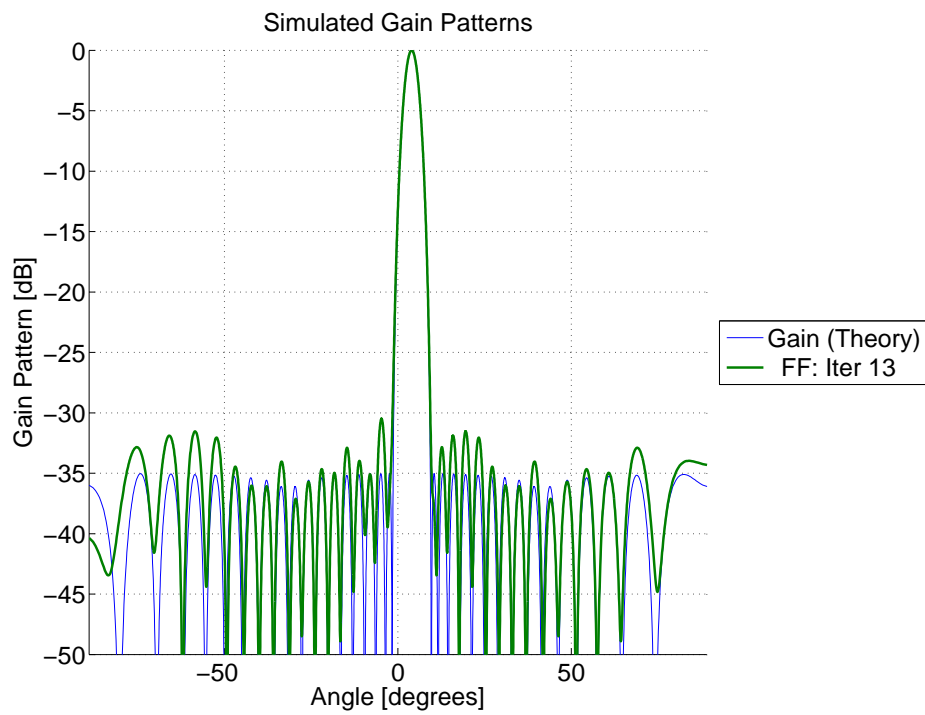


Figure 6.9: Radiation Pattern for the WR75 Z-slot Design

6.3 Ridged Waveguide Z-slot Antenna Design

The template is provided for the ridged waveguide Z-slot design and the resulting antenna is shown in Fig. 6.10.

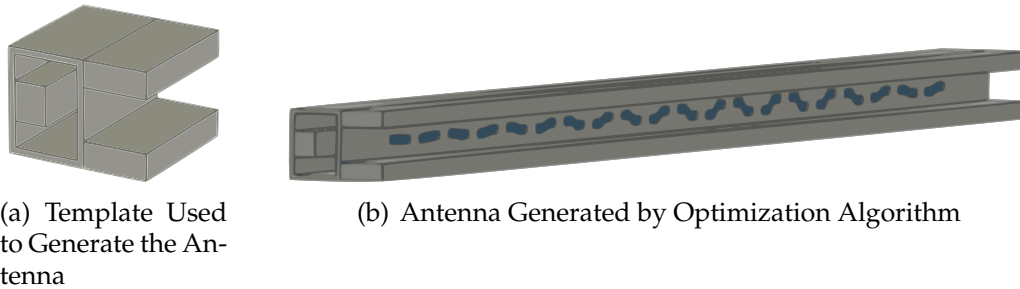


Figure 6.10: CST Model of the Ridged Waveguide Z-slot Template and Antenna

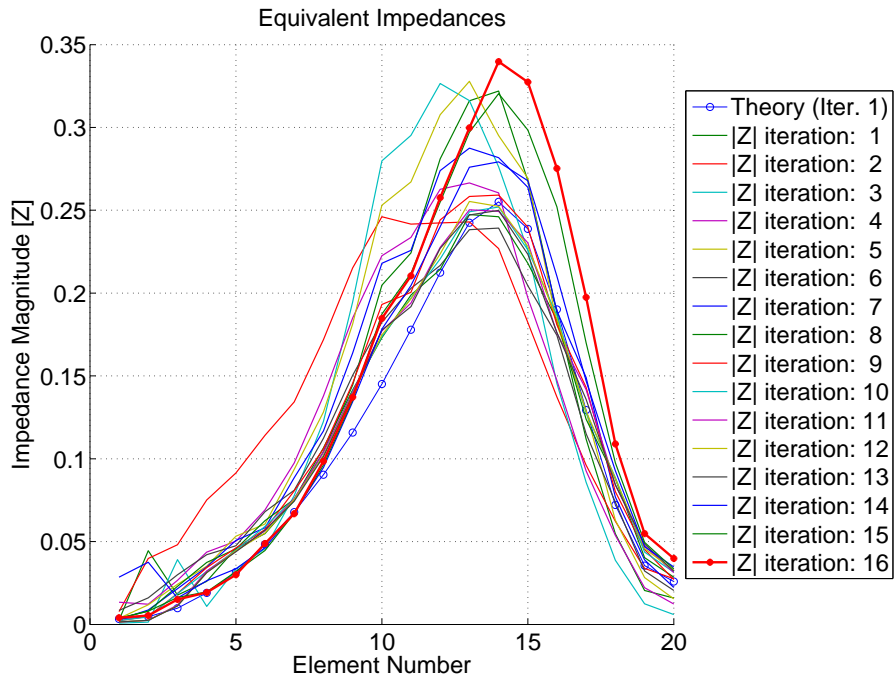
The desired performance is obtained after 16 iterations for the ridged waveguide Z-slot antenna. Again the initial error can be attributed to the aperture characterization neglecting to take mutual coupling into account. It can also be seen from Fig. 6.11(a) that the magnitude took longer to converge to the desired values than for the benchmark in Fig. 6.2(a).

Note that the values converge and then diverge again in later iterations. This is because the second phase of the tuning alters the magnitude based only on the aperture weighting. The load power is now incorrect (only $P_L = 7.9\%$), since the elements radiate more power than they are intended to. The final magnitudes shown in Fig. 6.11(b) shows this weighting.

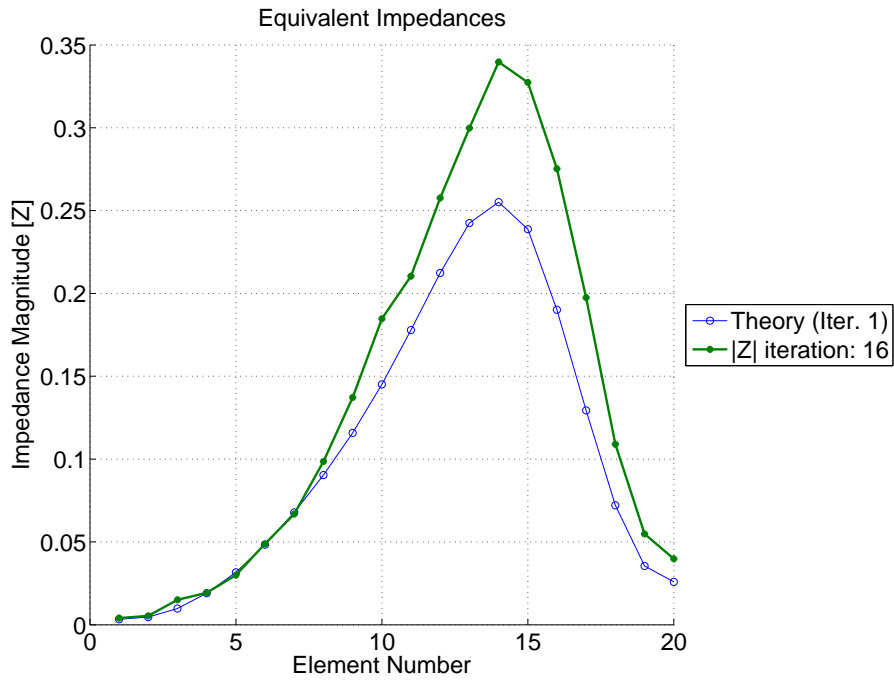
The phase error over all iterations is shown in Fig. 6.12(a). It can be seen that the lower impedance elements (placed at the ends of the array) are particularly sensitive to phase errors. Initial phase errors as high as $\theta_{err} = 85^\circ$ is observed for the initial iterations. The final phase values shown in Fig. 6.12(b) are reasonable compared to the initial values. Again, the second tuning phase change the aperture impedance values significantly, which also affects the phase.

The radiation pattern shown in Fig. 6.13 shows that despite the double-edged nature of the second tuning phase, the desired pattern can be obtained. A sidelobe level of -32 dB is obtained for the Z-slot antenna, which compares well to the results of the benchmark antenna.

For the sake of interest, the aperture excitations are shown in Fig. 6.14. This is to show the focus of the optimization algorithm during the second phase. Once the iterations converge during the first phase to the impedances based on the grid predictions, the focus is shifted away from impedance and rather to the aperture excitation weightings. Fig. 6.14(a) shows that the values converge to a weighting pattern that does not correspond to the desired weighting. However, after the second phase is started

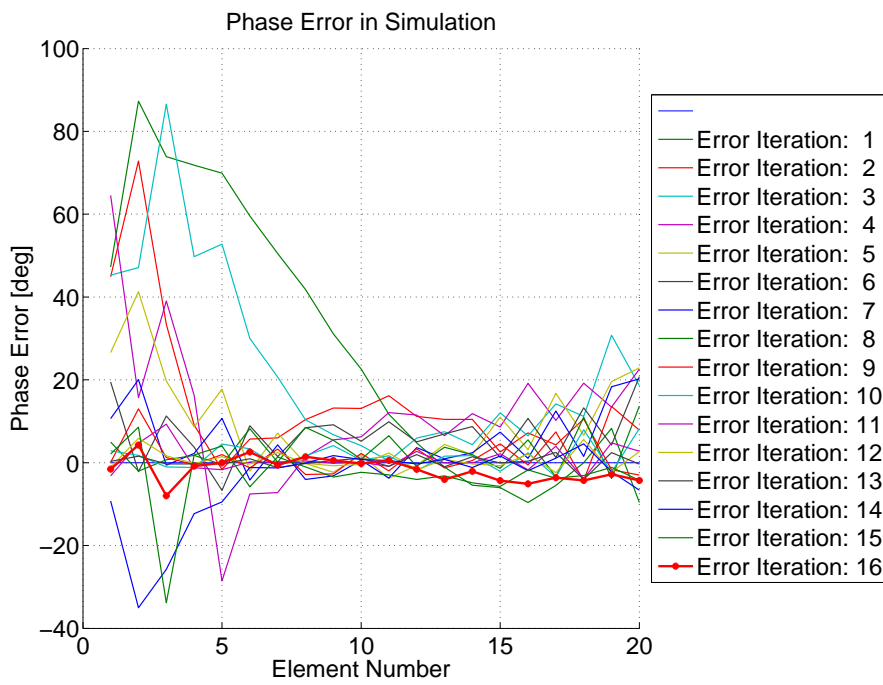


(a) Simulated Magnitudes Over All Iterations

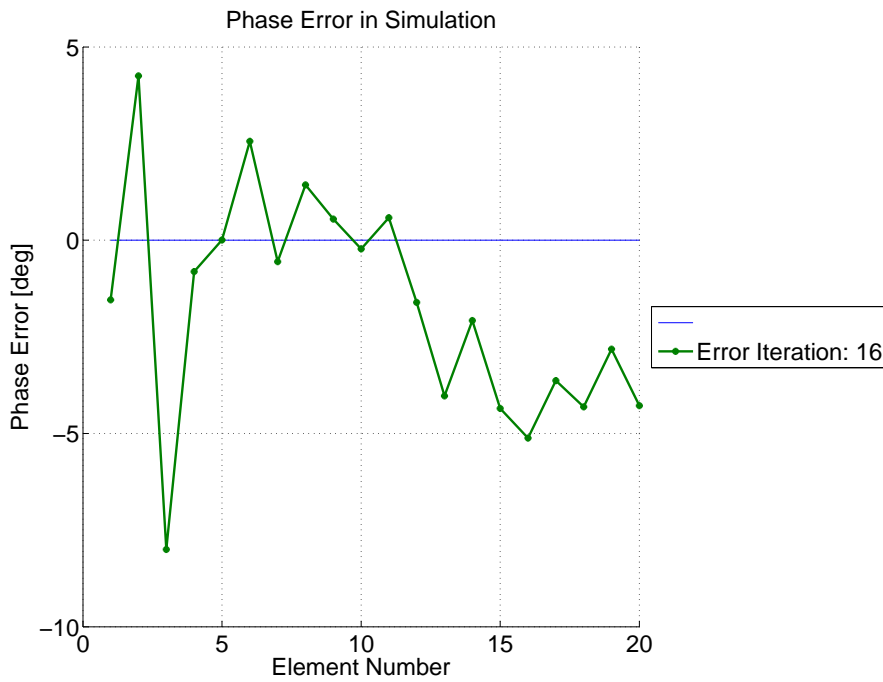


(b) Simulated Magnitude for Final Iteration

Figure 6.11: Simulated Magnitudes for All Iterations of the Ridged Waveguide Z-slot Antenna



(a) Simulated Phases Over All Iterations



(b) Simulated Phase for Final Iteration

Figure 6.12: Simulated Phases for All Iterations of the Ridged Waveguide Z-slot Antenna

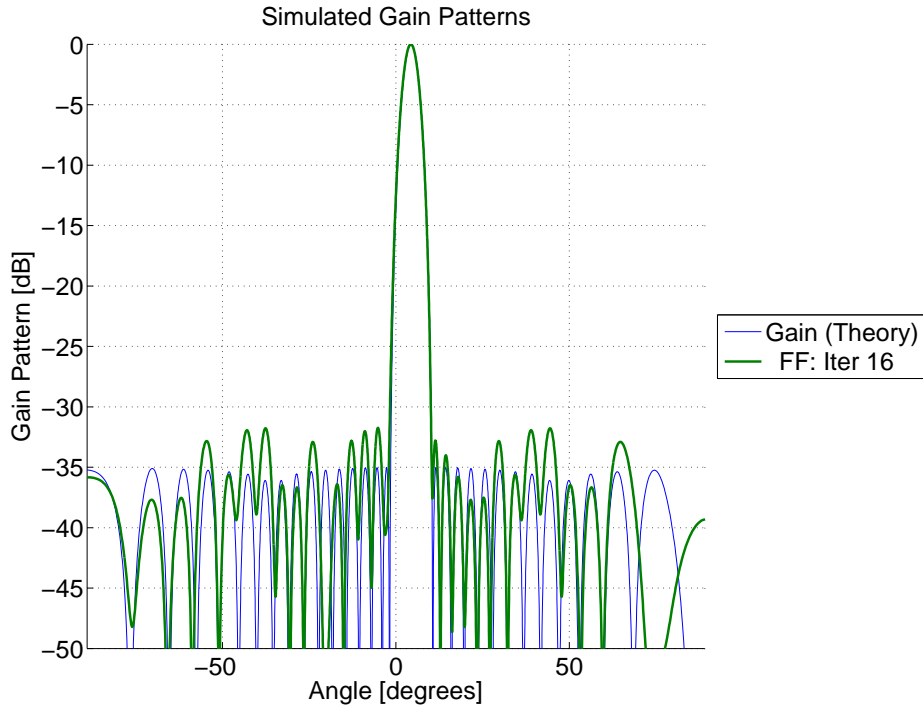
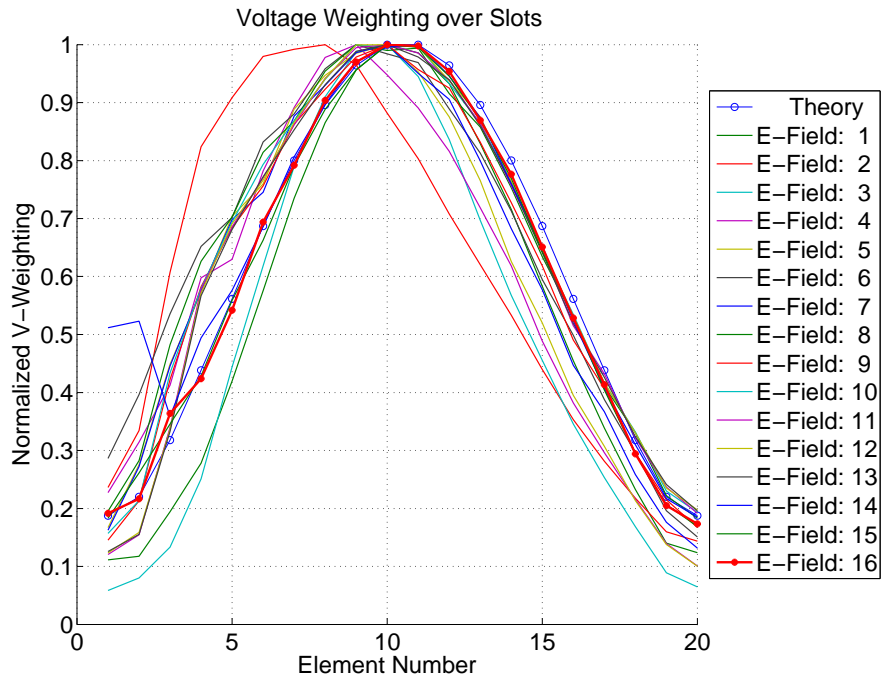


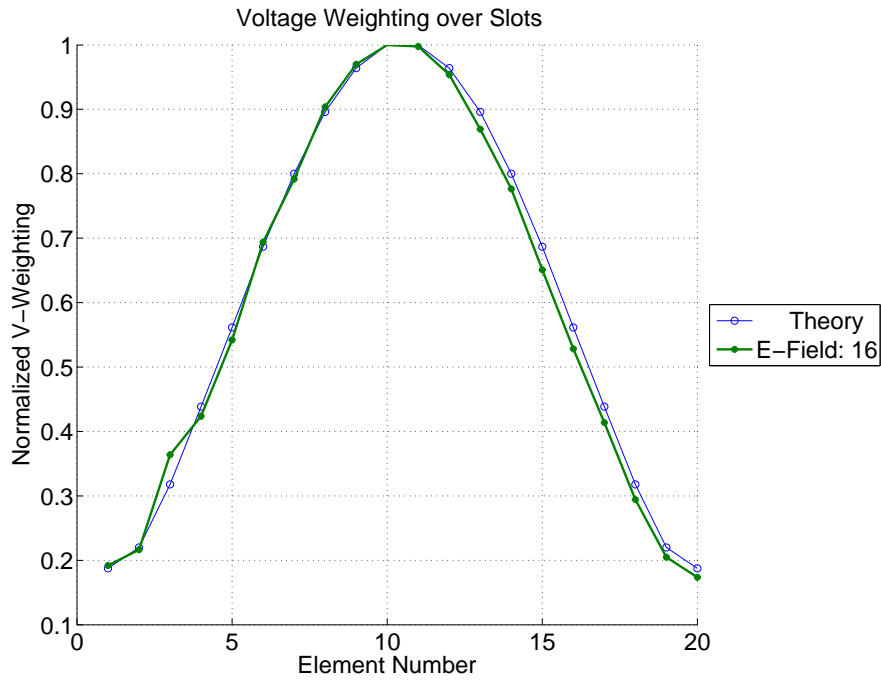
Figure 6.13: Radiation Pattern for the Ridged Waveguide Z-slot Design

(at iteration 14), the pattern converges in only 3 iterations and is shown in Fig. 6.14(b). The final load power is $P_L = 7.9\%$, which is lower than the design value of $P_L = 13\%$, due to the higher aperture impedance values.

Although the two tuning phases are performing as they are designed to, the algorithm admittedly needs to be adapted to simultaneously look at both the impedances *and* the excitation weightings. The transmission line method used in section 6.2 is one possible solution, where both the weighting and the load power is considered simultaneously.



(a) Simulated Weighting Over All Iterations



(b) Simulated Weighting for Final Iteration

Figure 6.14: Simulated Excitation Weightings for All Iterations of the Z-slot Antenna

6.4 Comparison of Benchmark and Z-slot Antenna Properties

The benchmark and Z-slot antennas all adhere to the minimum design specifications given in Tab. 6.1. It is now possible to compare their performance characteristics on an objective scale.

Only the broad wall radiation patterns were considered during the design process. Fig. 6.15 shows the 3D radiation patterns for all three antennas.

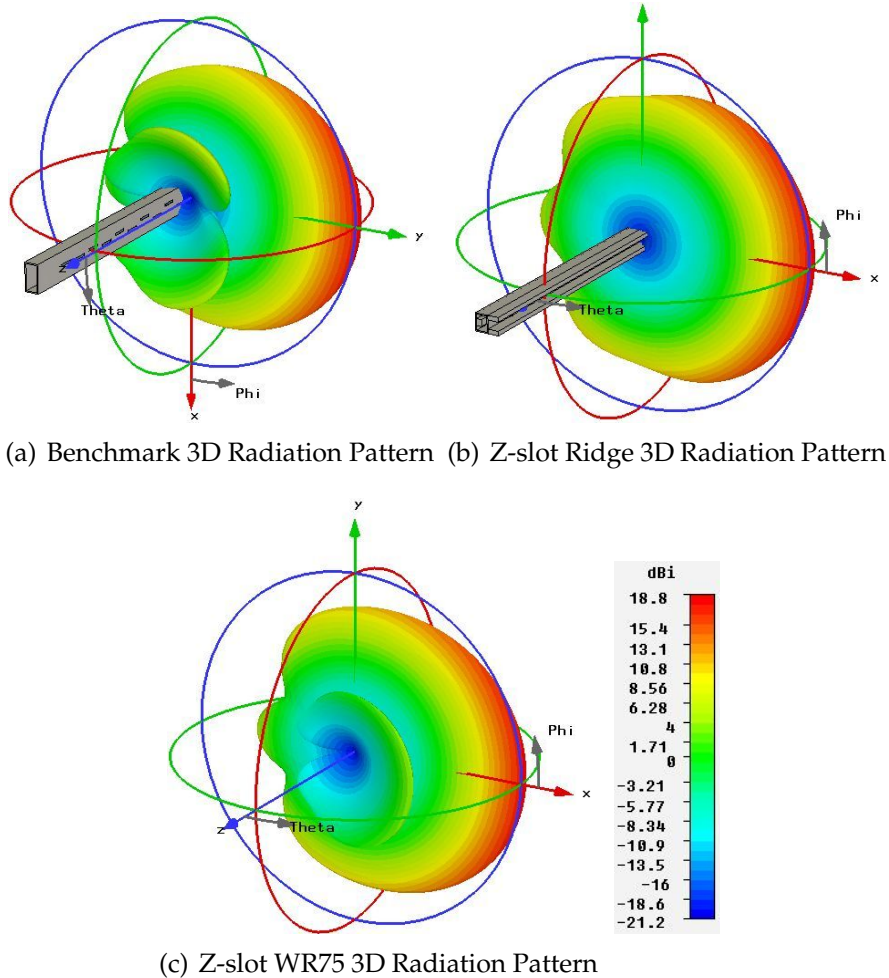


Figure 6.15: 3D Radiation Patterns

Note that the sidelobe in the elevation direction of the benchmark design (Fig. 6.15(a)) is all but removed from the ridged Z-slot antenna (Fig. 6.15(b)), yet still present in the WR75 Z-slot antenna.

Fig. 6.16 shows the radiation pattern for all three antennas with both the desired and cross-polarizations. The desired polarization is labeled as “phi” and the cross-polarization is labeled as “theta”. The main polarization

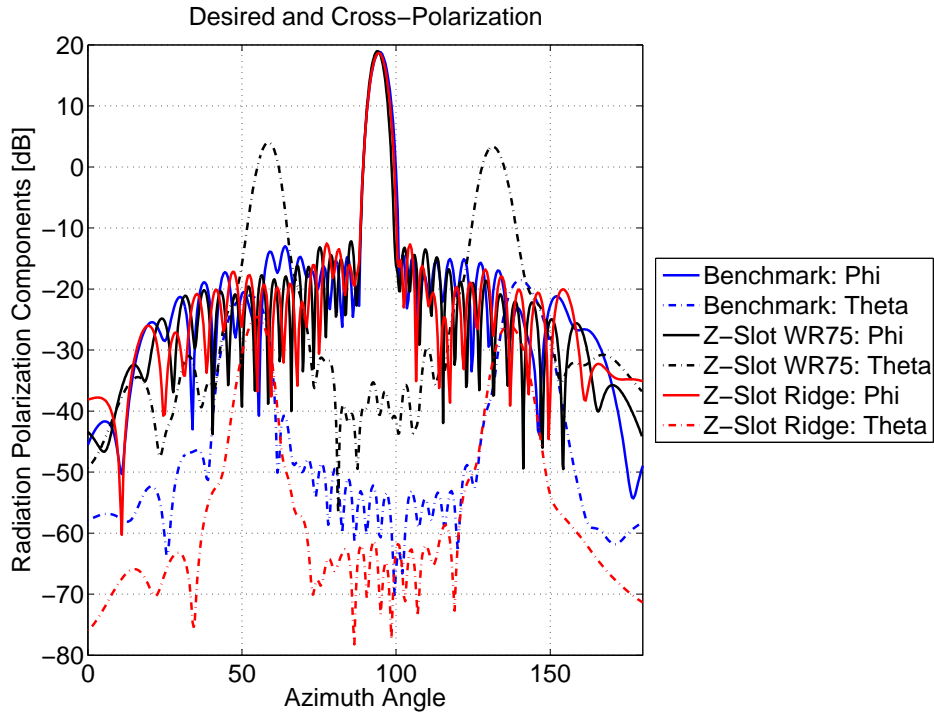


Figure 6.16: Polarization Components in the Radiation Pattern

appears at an azimuth angle of $\theta_{azim} = 94.6^\circ$, which corresponds to the main beam direction in the farfield patterns in Fig. 6.4, Fig. 6.13 and Fig. 6.9.

The cross-polarization shows a clear difference in performance between the three antennas. The benchmark shows a cross-polarization level that falls below the sidelobe level of the main polarization across all angles (for an elevation of 0°). This can be seen in Fig. 6.15(a) where the sidelobe disappears at a 0° elevation. In contrast, the WR75 Z-slot antenna shows a large sidelobe, which corresponds to the large cross-polarization shown in Fig. 6.16. Finally the ridged waveguide Z-slot antenna, which has the lowest cross-polarization, has no visible sidelobe in the 3D pattern. Here the cross-polarization component falls well below the desired polarization. These results indicate that there is a correlation between the cross-polarization of an antenna and the sidelobes found in the 3D pattern.

The absolute value of both polarizations provide the radiation patterns shown in Fig. 6.15. The azimuth cut for an elevation of 0° is shown in Fig. 6.17 for clarity. The difference between these patterns and the ones shown previously during the design process is that only the main polarization component was considered there.

The cross-polarization levels shown in Fig. 6.18 show that the ridged waveguide Z-slot antenna is very comparable in performance to the benchmark antenna. In fact, over the main beam, the cross-polarization of the

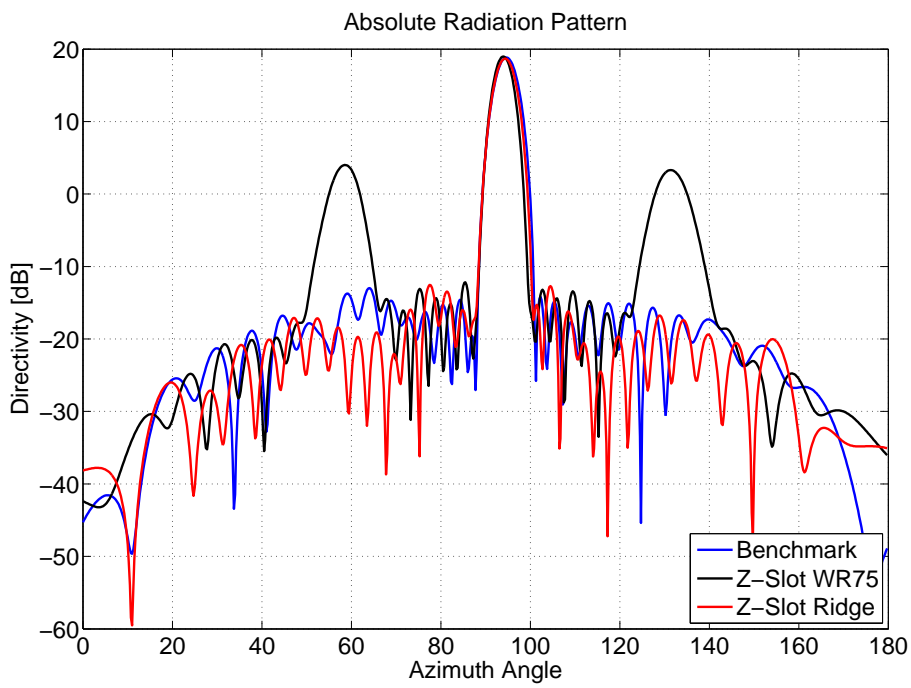


Figure 6.17: Absolute Radiation Pattern Including Both Polarization Components

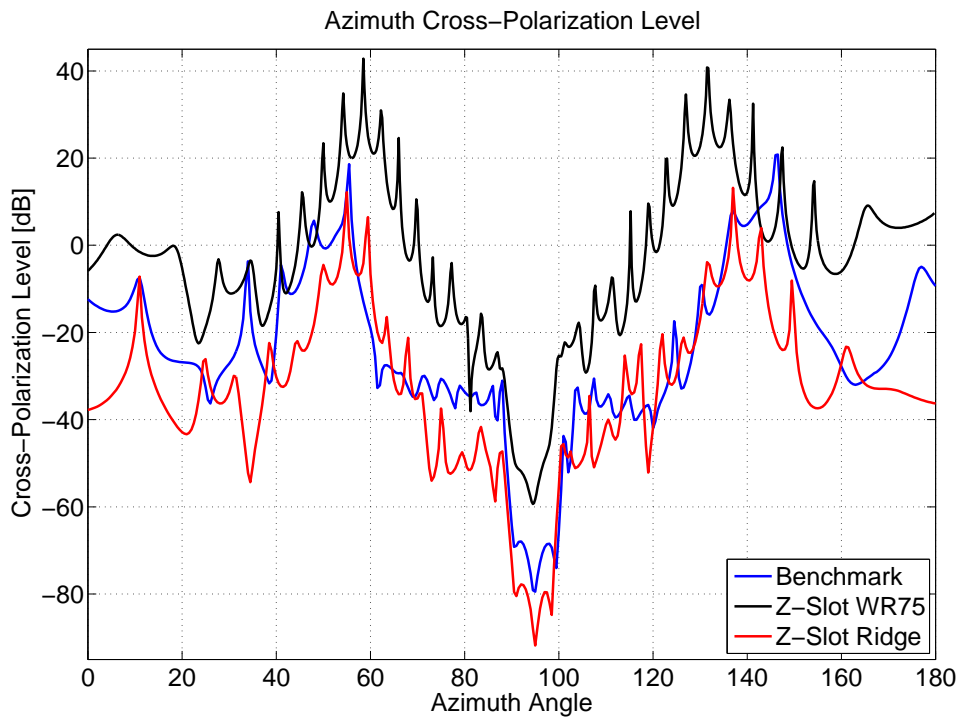


Figure 6.18: Cross-Polarization Level in the Azimuth Cut

ridged waveguide Z-slot antenna is more than 8.5 dB lower than the benchmark. It should also be noted that the WR75 Z-slot antenna (which is a linear array), does not perform as well as the benchmark antenna, indicating that the linear array assumption is not at fault for the appearance of the sidelobes but rather the cross-polarization.

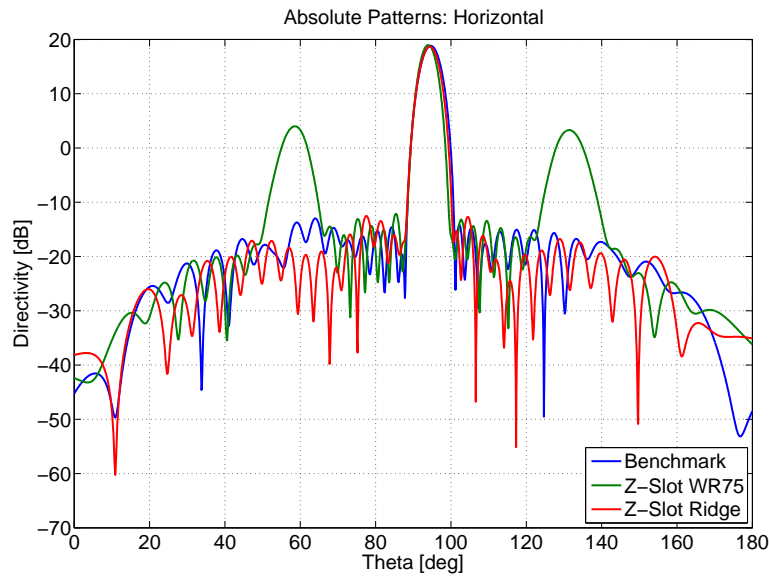


Figure 6.19: Horizontal Cut ($\phi = 0^\circ$) of Radiation Pattern for All Designs

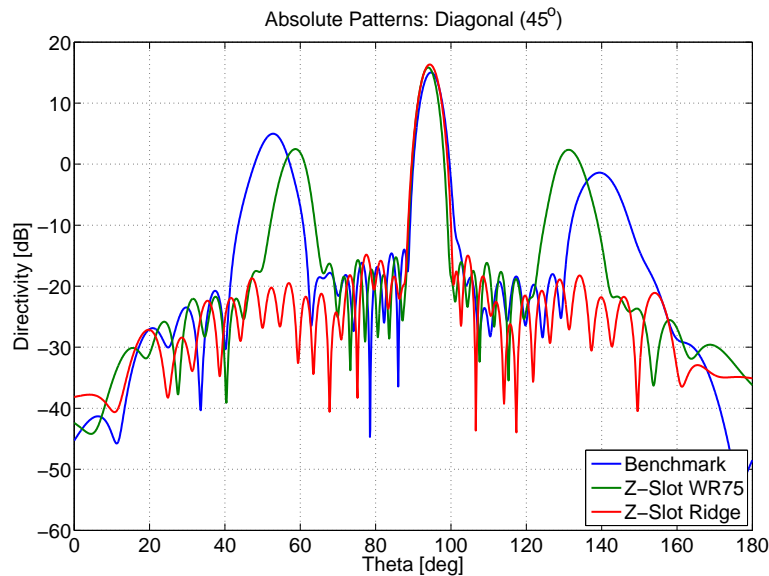


Figure 6.20: Diagonal Cut ($\phi = 45^\circ$) of Radiation Pattern for All Designs

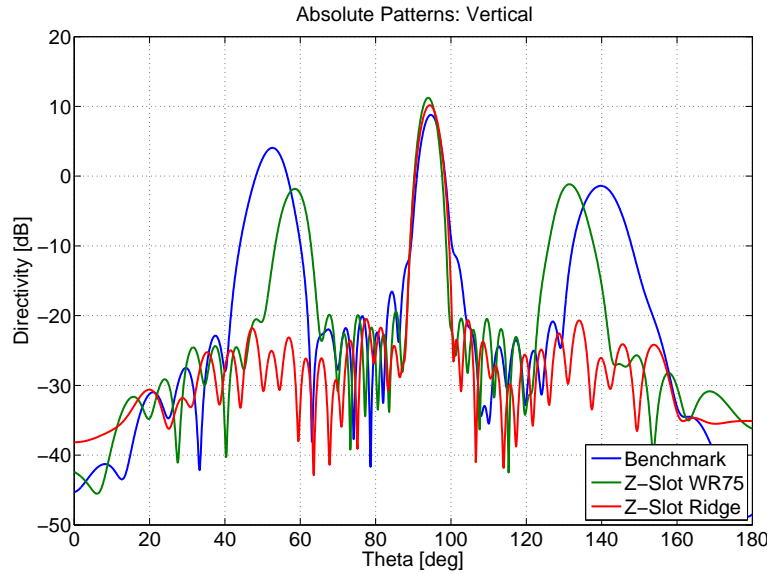


Figure 6.21: Vertical Cut ($\phi = 90^\circ$) of Radiation Pattern for All Designs

In Figs. 6.19–6.21, the absolute radiation pattern cut is shown for different elevations. Three elevations are given, namely “Horizontal”, “Diagonal” and “Vertical”. The horizontal cut (Fig. 6.19) refers to an elevation of $\phi = 0^\circ$, which corresponds to the same cut used during the design process. The diagonal cut (Fig. 6.20) looks at the radiation pattern at $\phi = 45^\circ$, where the 3D radiation pattern indicates the sidelobes are already quite prominent. The vertical cut (Fig. 6.19) corresponds to $\phi = 90^\circ$, which is the plane tangential to the desired radiation direction.

These plots indicate how well the Z-slot antenna with polarizer plates suppress the undesired sidelobes. Note that this is the absolute pattern, not just the desired polarization. For all practical purposes, the ridged waveguide Z-slot antenna completely suppresses the sidelobes in the 3D pattern (for the cuts shown) and keeps the sidelobe level to below the -30 dB criteria.

Chapter 7

Conclusions

7.1 Summary

For a radar antenna to be effective, it was argued in chapter 1 that the radiation pattern must be precisely designed and that the presence of sidelobes are undesired. Unwanted sidelobes have been observed in slotted waveguide designs for the standard rectangular offset slots in a rectangular waveguide. The possible cause of these sidelobes were hypothesized to be attributed to

1. cross-polarization and
2. the incorrect assumption of a linear array.

By isolating the cause of the sidelobes, a design procedure that takes the effect of cross-polarization into account could be developed to generate an antenna with the desired radiation pattern properties.

The steps involved in determining the cause of the undesired sidelobes involved a very practical approach. A typical antenna with offset rectangular apertures is taken as a benchmark with which to compare the results of other designs. The benchmark is broken down into its base components (namely the waveguide and the apertures) and investigated separately.

The waveguide is assumed to have no contribution to the polarization properties of the antenna, as the propagation mode by definition suppresses the undesired polarization component (i.e. the E-field in the direction of propagation). However, the design specification in Tab. 1.1 is considered and a custom waveguide profile is designed to conform to specifications. A ridged waveguide is found that has the correct operating frequency, bandwidth and tolerance bands.

The isolated offset rectangular aperture is investigated, along with the Z-slot. Polarization properties, radiation capacity and bandwidth properties of the apertures are discussed for various configurations. The effect of adding polarization plates to the Z-slot is also investigated. It was found

that by adding polarizer plates of increasing lengths, the unwanted polarization component of the Z-slot could be significantly suppressed. This result, in conjunction with the ridged waveguide design, provided the base components used for the low cross-polarization design. A linear array design is also completed (with poor cross-polarization levels).

The final antennas that were designed includes: a benchmark antenna using offset rectangular apertures; a Z-slot array in WR75; and a Z-slot array in a ridged waveguide with polarizer plates. The two Z-slot antennas serve to investigate whether it is the cross-polarization or the offsets of the rectangular apertures that cause the unwanted sidelobes. The low cross-polarization antenna showed significant improvement in the sidelobe level, where the “linear array” antenna showed a deterioration in performance. The conclusion that can be drawn from this is that by suppressing the cross-polarization, the unwanted sidelobes can be suppressed.

A ridged waveguide Z-slot antenna with polarizer plates is provided as a possible alternative to the offset aperture antenna. All of the performance properties compare well to the benchmark antenna, with the exception that the unwanted sidelobes are suppressed by approximately 15 – 20 dB.

7.2 Recommendations for Future Research

As is often the case, by answering one question two more are asked. The results shown here serve to indicate a trend in antenna behavior based on the polarization properties of a linear array. However, the precise extent to which the polarization affects the radiation pattern of an antenna is not discussed, nor is the possibility that the linear array is inaccurate completely eliminated.

Further investigation into the precise effect of the cross-polarization on the radiation pattern of an antenna should be conducted. Also, the only suppression technique considered here are the polarizing plates around a Z-slot antenna. More generic polarizers can be considered to further help improve the performance of the antenna.

The assumption that all radiators are placed in a straight line may still contribute to some extent to the poor sidelobe level of the offset rectangular aperture antenna. The limits of this approximation must be determined, particularly for arrays with a low number of elements (i.e. with large aperture offsets).

An improved method of characterizing arbitrary aperture configurations will serve to improve the first order design of an array. The apertures were either characterized as a parallel or series impedance, where complex apertures may perform more like a T or Π network. By accurately determining the equivalent network, better first-order designs can be made.

The optimization algorithm is very simple in comparison to some of the advanced methods being developed in the world. More intelligent algorithms should be considered to reduce the number of iterations necessary to obtain convergence. The current method relies on a priori knowledge of how the apertures operate, which is undesirable. An improved optimization algorithm will be independent of the equivalent network of an aperture or its behavior.

A general design approach may be also be investigated, where the ridged waveguide is turned on its head and the slots inserted into the trough of the ridge. By extending the outside of the ridge, the polarizer plates become a natural extension of the waveguide, making it more compact and lighter. The reason this was not done here is because it was difficult to model in CST. It may be possible that a different simulation tool could be used, alternatively the model may include a waveguide transition could be included (such as the one in Appendix D). This approach would likely make for a more practical antenna with much the same performance characteristics as the ridged waveguide antenna designed here.

7.3 Conclusion

The aim of the research conducted was to gain a greater understanding of slotted waveguide antennas along with the appearance of undesired sidelobes. Two possible causes to the sidelobes were hypothesized and systematically investigated. Several antennas were designed to verify the effect of the varying elements in a design (e.g. the waveguide profile, the aperture chosen and the polarizer plates). The resulting antennas both served to deepen the understanding of the problem, as well as to provide an alternative to the current design method used.

Appendices

Appendix A

Benchmark Design

A.1 Introduction

The dimensions for manufacture and the expected results are provided here. Note that no tolerances were considered and that results are subject to vary due to measurement and manufacturing errors. Fig. A.1 shows a depiction of the antenna.

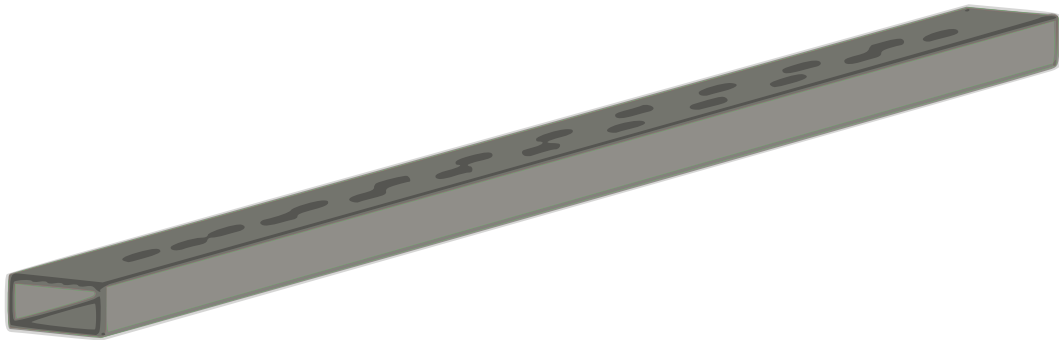


Figure A.1: Model of the Benchmark Antenna

A.2 Dimensions

Tab. A.1 provides the offsets and aperture lengths for the rectangular offset apertures inset into a rectangular waveguide. The element numbering starts from the source and increase toward the terminating load. The apertures have angled corners, as this is the most commonly found aperture in the literature. Milling such an aperture could be difficult and would commonly have rounded corners. The width of the aperture is $ap_width = 2$ mm for all elements. Elements are spaced $elem_sp = 20.40175$ mm apart from the center of each element.

Table A.1: Dimensions of Benchmark Apertures

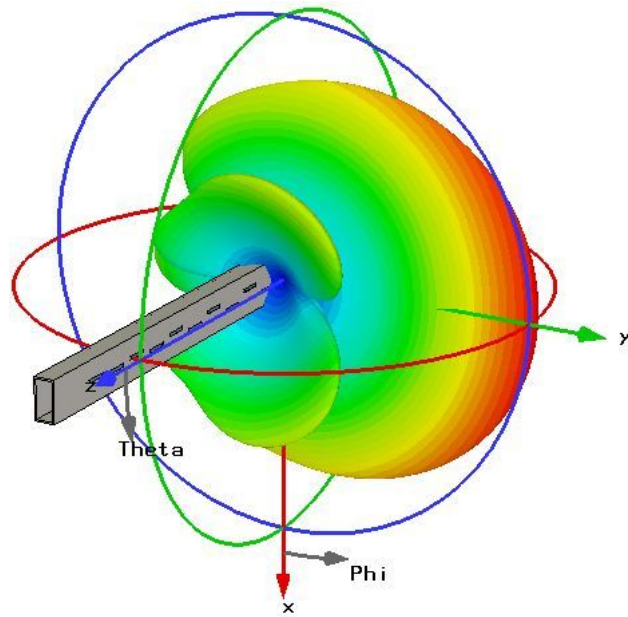
Element No.	Offset [mm]	Length [mm]
1	0.5892	13.59924
2	0.6925	13.61637
3	0.8755	13.61637
4	1.4579	13.61637
5	1.5976	13.63350
6	2.1541	13.63350
7	2.3786	13.68487
8	2.7279	13.73482
9	3.0653	13.78620
10	3.3758	13.80333
11	3.7711	13.83758
12	4.1468	13.85470
13	4.5320	13.87183
14	4.6050	13.88895
15	4.3998	13.87183
16	3.9677	13.83758
17	3.3063	13.78620
18	2.3613	13.70057
19	1.8018	13.63350
20	1.7369	13.63350

A standard WR90 profile is used, with a wall thickness of $th = 1$ mm. The inside dimensions of the profile are 22.86×10.16 mm. The total length of the antenna is $length = 469.2403$ mm.

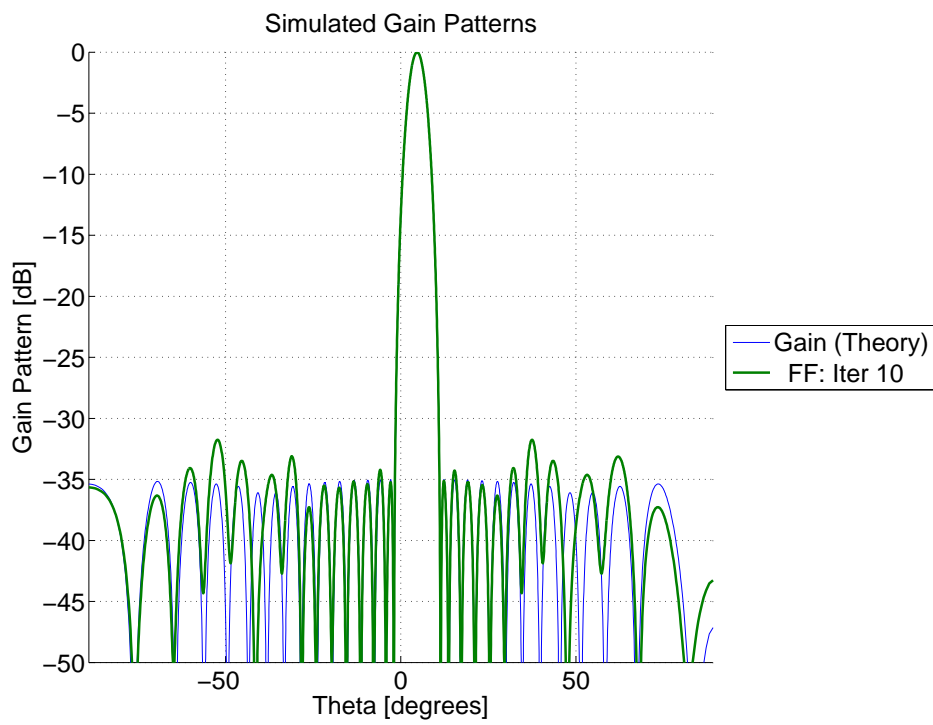
A.3 Simulated Results

The radiation pattern shown in Fig. A.3 shows the accuracy of the model in the azimuth direction as well as the 3D radiation pattern that exhibits the undesired sidelobes.

Fig. A.2(a) clearly shows the sidelobes at about 10 – 13 dB below the main lobe. The pattern in the azimuth cut shown in Fig. A.2(b) shows how well the designed pattern conforms to the theoretical pattern. The results indicated that all values are within tolerance and that the antenna performs as expected.



(a) 3D Radiation Pattern



(b) Azimuth Radiation Pattern

Appendix B

WR75 Waveguide Z-slot Design

B.1 Introduction

The dimensions for manufacture and the expected results are provided here. Note that no tolerances were considered and that results are subject to vary due to measurement and manufacturing errors. Fig. B.1 shows a depiction of the antenna.

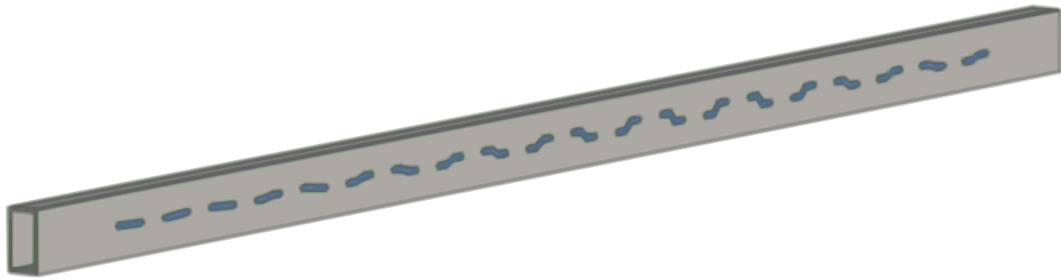


Figure B.1: Model of the WR75 Z-slot Antenna

A standard WR75 profile is used, with a wall thickness of $th = 1$ mm. The inside dimensions of the profile are 19.05×9.525 mm. The total length of the antenna is $length = 553.3372$ mm.

B.2 Dimensions

Tab. B.1 provides the rotation angles (in degrees) of the apertures as well as their lengths. The element numbering starts from the source and increase toward the terminating load. The angle is defined in Fig. 4.1.

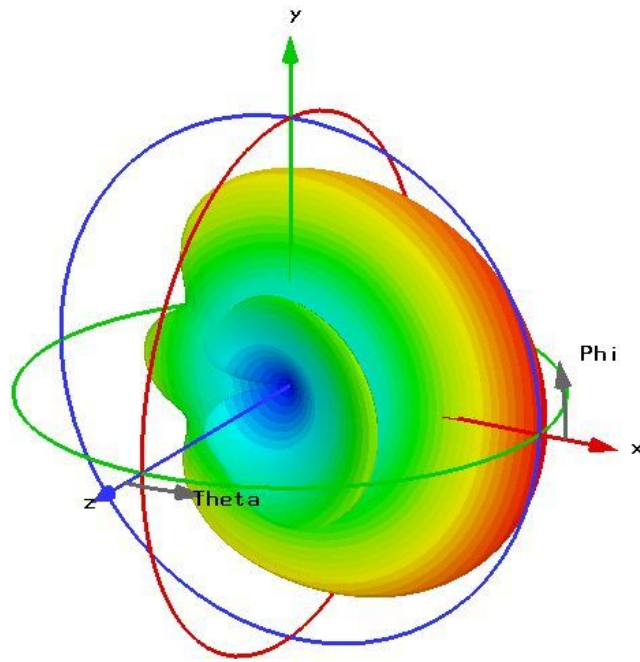
Table B.1: Dimensions of Z-slot Apertures in WR75

Element No.	Angle [deg]	Length [mm]
1	87.6702	12.28056429
2	85.3467	12.19350857
3	82.0847	12.22347857
4	78.6415	12.24203143
5	74.9699	12.20920714
6	71.3257	12.23204143
7	68.0284	12.29198143
8	64.7099	12.33622286
9	60.9176	12.43612286
10	56.0933	12.57741
11	49.83	12.74295857
12	42.6051	12.92848714
13	37.438	13.08832714
14	35.3394	13.14255857
15	37.7259	13.07833714
16	45.1924	12.87996429
17	56.6297	12.69300857
18	64.6498	12.59168143
19	68.5645	12.57170143
20	69.0049	12.57027429

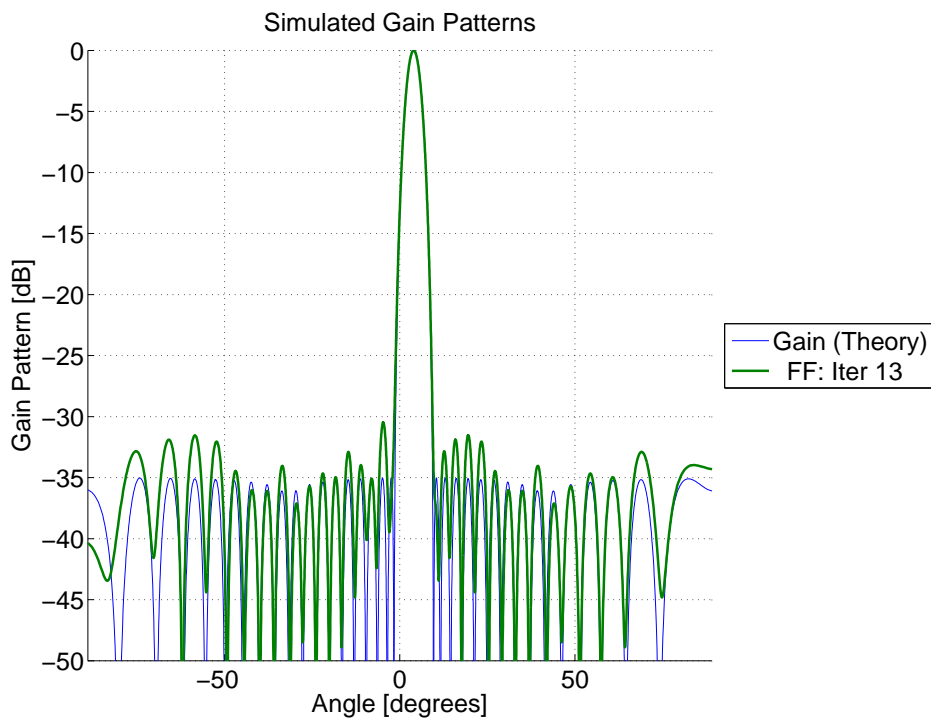
B.3 Simulated Results

The radiation pattern shown in Fig. B.3 shows the accuracy of the model in the azimuth direction as well as the 3D radiation pattern that exhibits the undesired sidelobes.

Fig. B.2(a) shows the undesired sidelobes are present at a level of approximately 15 dB below the main lobe. The pattern in the azimuth cut shown in Fig. C.3(b) shows how well the designed pattern conforms to the theoretical pattern. The results indicated that all values are within tolerance and that the antenna performs as expected. Note that in the case of Fig. B.2(b), the pattern is calculated only with the E_x component, which is why it differs from the 3D pattern. The sidelobes here are therefore a result of the cross-polarization component.



(a) 3D Radiation Pattern



(b) Azimuth Radiation Pattern

Appendix C

Ridged Waveguide Z-slot Design

C.1 Introduction

The dimensions for manufacture and the expected results are provided here. Note that no tolerances were considered and that results are subject to vary due to measurement and manufacturing errors. Fig. C.1 shows a depiction of the antenna. The waveguide used is not standard, so it must be extruded for best results. The polarizer plates may cause difficulties in milling the apertures, otherwise they may be attached after milling.

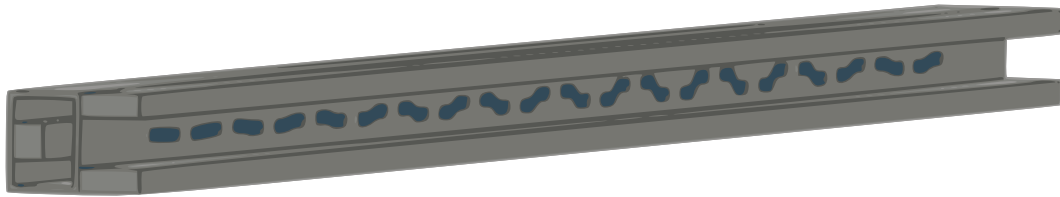


Figure C.1: Model of the Ridged Waveguide Z-slot Antenna

C.2 Dimensions

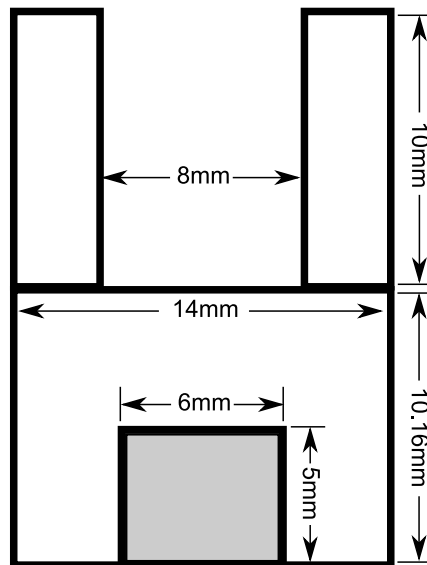
Tab. C.1 provides the rotation angles (in degrees) of the apertures as well as their lengths. The element numbering starts from the source and increase toward the terminating load. The angle is defined in Fig. 4.1.

The profile is designed to conform to the specifications of Tab. 1.1. The dimensions are given in Fig. C.2 and include the polarizer dimensions used.

The wall thickness is again $th = 1$ mm. The element spacing is $elem_sp = 21.79581$ mm and the total length of the antenna is $length = 501.3036$ mm. Apertures are $ap_width = 2$ mm for all elements.

Table C.1: Dimensions of Z-slot Apertures in a Ridged Waveguide

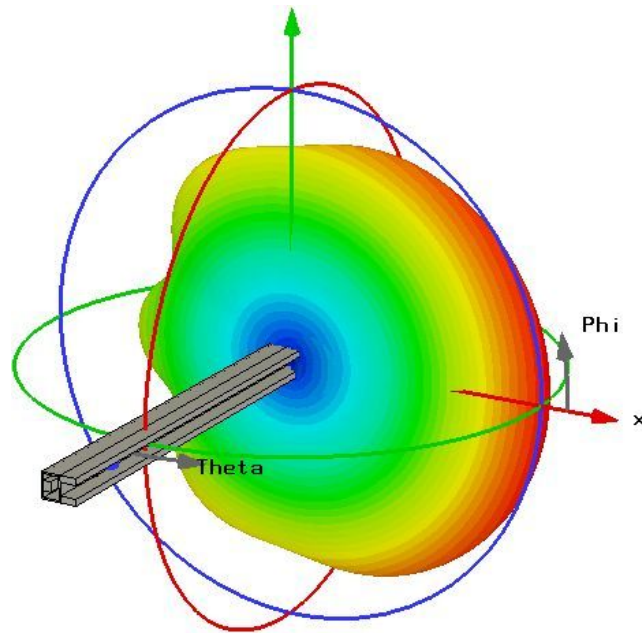
Element No.	Angle [deg]	Length [mm]
1	84.7445	16.41214
2	83.6496	16.41214
3	80.8029	16.41214
4	77.9562	16.41214
5	75.7664	15.90551
6	73.7956	15.46880
7	71.6058	15.19194
8	69.6350	14.96217
9	67.4453	14.82373
10	65.0365	14.73240
11	62.6277	14.63963
12	60.0000	14.59396
13	57.8102	14.57113
14	56.9343	14.57113
15	58.0292	14.57113
16	61.7518	14.61680
17	66.3504	14.77806
18	71.1679	15.14627
19	75.3285	15.79134
20	76.6423	16.18237

**Figure C.2:** Waveguide Profile for the Ridged Waveguide Z-slot Antenna

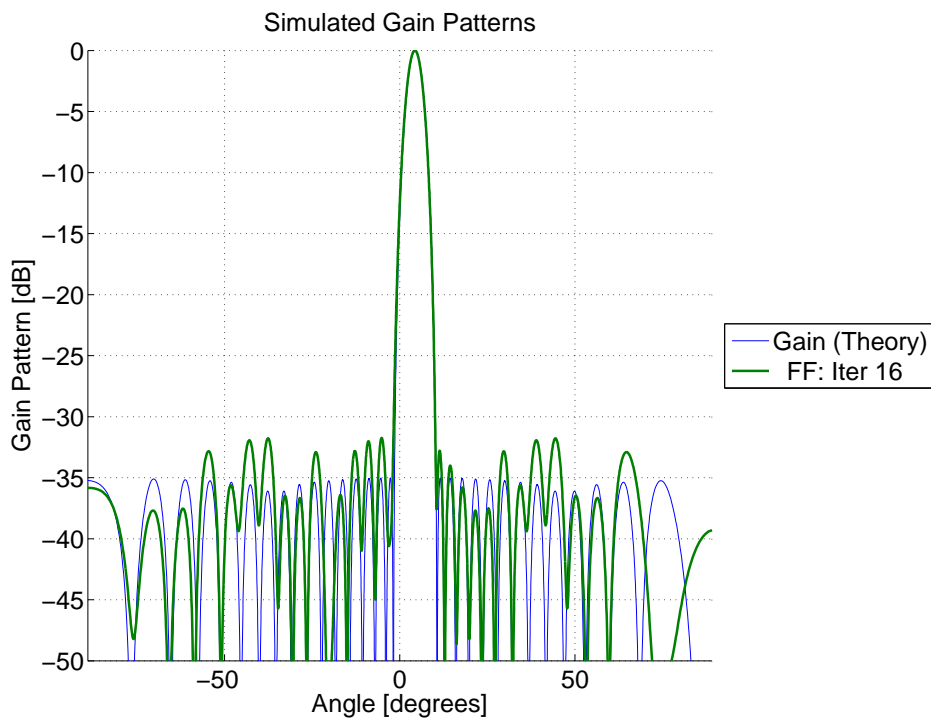
C.3 Simulated Results

The radiation pattern shown in Fig. C.3 shows the accuracy of the model in the azimuth direction as well as the 3D radiation pattern that exhibits the undesired sidelobes.

Fig. C.3(a) shows the sidelobes are suppressed to approximately 25 – 30 dB below the main lobe. The pattern in the azimuth cut shown in Fig. C.3(b) shows how well the designed pattern conforms to the theoretical pattern. The results indicated that all values are within tolerance and that the antenna performs as expected.



(a) 3D Radiation Pattern



(b) Azimuth Radiation Pattern

Appendix D

WR90 to Ridged Waveguide Transition

The CST simulations included an artificial termination load and feed port. This is convenient for simulation purposes in that it reduces the complexity of the model, but makes for an incomplete real-world design. In order to build and test the antennas designed using the ridged waveguide, it is necessary to find a means of feeding the antenna and to absorb the energy at the terminating port.

For this purpose a waveguide transition was designed using FEKO, a computational tool similar to CST. The results were optimized to transfer the maximum power at f_0 . The reflection coefficient, which in this case equals S_{11} , is shown in Fig. D.1. It can be seen that at $f = 10.5 = f_0$, most of the input power is absorbed by the output port depicted in Fig. D.2.

It should be noted that Fig. D.2 illustrates the two uses of the transition: primarily as a feed for the antenna, but also as a terminating load at the end of the antenna. In other words, the model in Fig. D.2 can be split in half and two elements must be manufactured. The first element will port energy propagating down a standard WR90 profile to the custom ridge profile. The terminating load will be attached to the end of the antenna, along with a WR90 terminating load attached.

The transition is made up of three sections:

- a WR90 section;
- a transition from WR90 to the ridged profile; and
- a ridged profile section.

Each of these sections is $secLen = 14.61457 \text{ mm} = 0.511864 \times \lambda$ long. It is this value that is optimized to provide the desired operating frequency. All other dimensions correspond to the respective profile dimensions. Further images of a transition is shown in Fig. D.3.

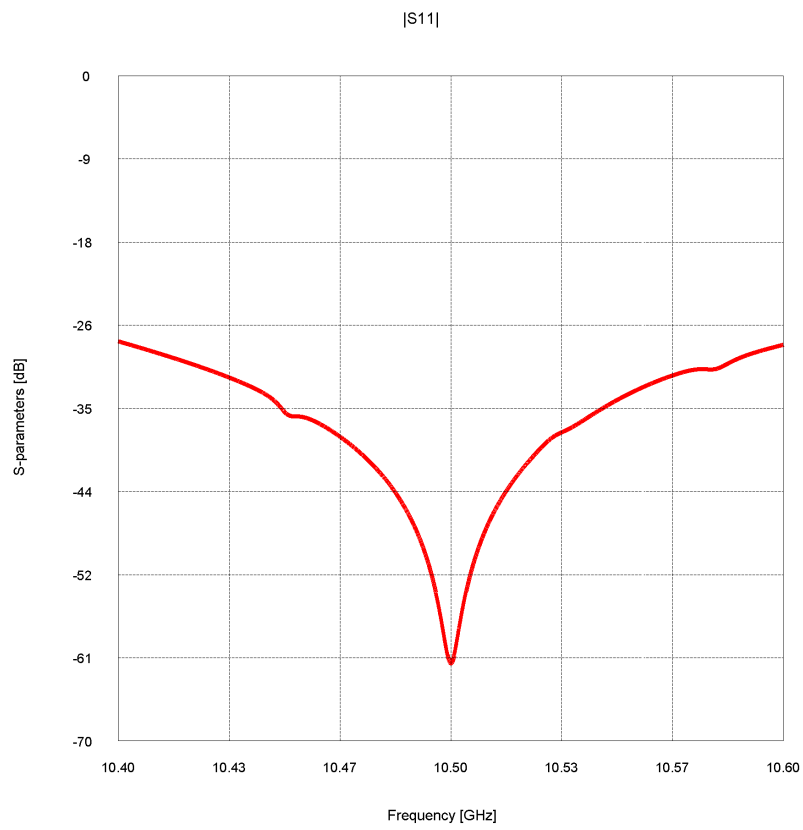


Figure D.1: Magnitude of S_{11}

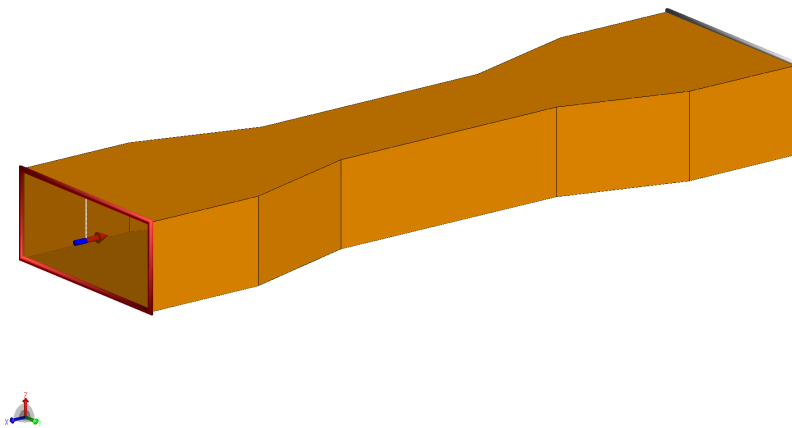


Figure D.2: Two-port Model for the Waveguide Transition

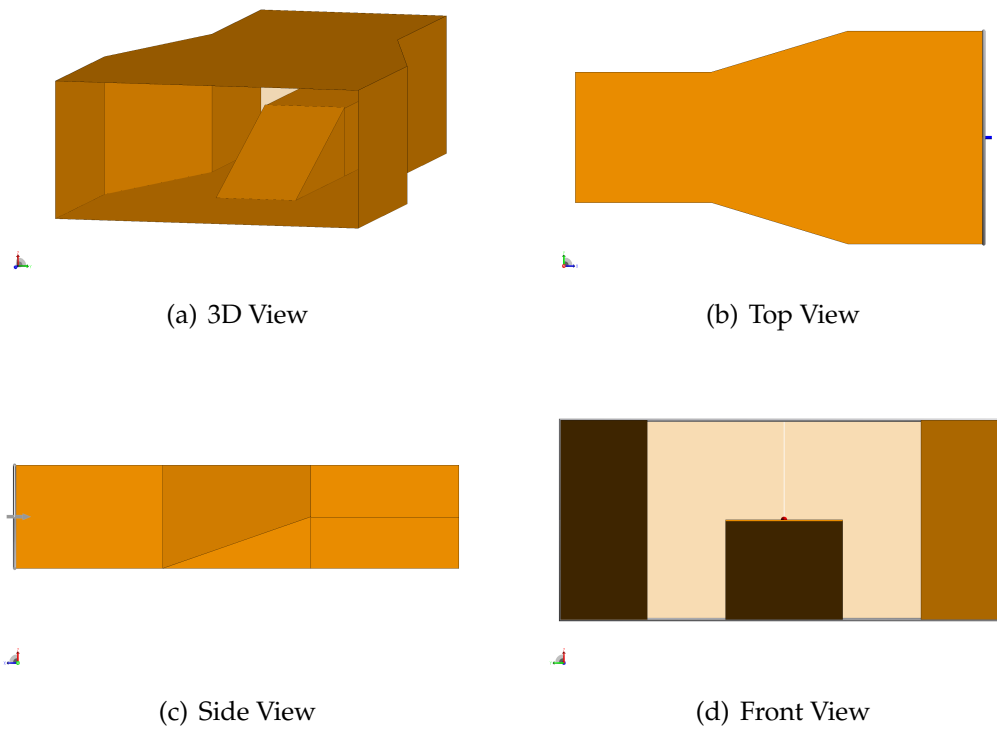


Figure D.3: Single-Ended WR90 to Ridged Waveguide Transition

Bibliography

- [1] M. Skolnik, *Introduction to Radar Systems*, 3rd ed. McGraw Hill, 2001.
- [2] "Private communication."
- [3] R. Elliot, *Antenna Theory and Design*. Prentice Hall, 1981.
- [4] D. Howard, Ed., *Dictionary of Electronics*, 4th ed. Penguin Reference, 2005.
- [5] D. Pozar, *Microwave Engineering*, 3rd ed. John Wiley & Sons, 2005.
- [6] S. Ramo, J. Whinnery, and T. van Duzer, *Fields and Waves in Communication Electronics*. John Wiley & Sons, 1994.
- [7] W. Hoefler and M. Burton, "Closed-form expressions for the parameters of finned and ridged waveguides," *IEEE Transactions on Microwave Theory and Techniques*, vol. MTT30, no. 12, pp. 2190–2194, Dec 1982.
- [8] S. Hopfer, "The design of ridged waveguides," *Transactions on Microwave Theory and Techniques*, vol. 3.5, pp. 20–29, Oct. 1955.
- [9] H. Booker, "Slot aeri-als and their relation to complementary wire aeri-als," *J. IEE (London)*, vol. 93, pp. 620–626, Dec 1946.
- [10] G. Deschamps, "Impedance properties of complementary multiterminal planar structures," *IRE Transactions on Antennas and Propagation*, vol. 7, pp. 371–378, 1959.
- [11] A. Stevenson, "Theory of slots in rectangular wave-guides," *Journal of Applied Physics*, vol. 19, pp. 24 – 38, 1948.
- [12] A. Oliner, "The impedance properties of narrow radiating slots in the broad face of rectangular waveguide: Part i–theory," *IRE Trans. Antennas Propagat.*, vol. 5, pp. 4–11, Jan. 1957.
- [13] ———, "The impedance properties of narrow radiating slots in the broad face of rectangular waveguide: Part ii–comparison with measurement," *IRE Trans. Antennas Propagat.*, vol. 5, pp. 12–20, Jan. 1957.

- [14] ———, "Equivalent circuits for small symmetrical longitudinal apertures and obstacles," *Transactions on Microwave Theory and Techniques*, vol. 8.1, pp. 72–80, Jan. 1960.
- [15] J. Gulick, G. Stern, and R. Elliot, "The equivalent circuit of a rectangular-waveguide-fed longitudinal slot," *IEEE Int. Antennas Propagat.*, vol. 24, pp. 685–688, Jun. 1986.
- [16] C. Balanis, *Antenna Theory*, 3rd ed. John Wiley & Sons, 2005.
- [17] A. Villeneuve, "Taylor patterns for discrete arrays," *IEEE Trans. Antennas Propagat.*, vol. 32, pp. 1089–1093, Oct. 1984.
- [18] J. Volakis, *Antenna Engineering Handbook*, 4th ed. McGraw Hill, 2007.
- [19] D. Kim and R. Elliott, "A design procedure for slot arrays fed by single-ridge waveguide," *IEEE Int. Antennas Propagat.*, vol. 36, pp. 1531–1536, November 1988.
- [20] (2009, Sept) Rectangular waveguide dimensions. Microwave Encyclopedia - Microwaves 101. [Online]. Available: <http://www.microwaves101.com/encyclopedia/waveguidedimensions.cfm>